Inelastic Earthquake Response and Damage Assessment of Retrofitted RC Structures

Kazuyuki IZUNO

December 1992

Inelastic Earthquake Response and Damage Assessment of Retrofitted RC Structures

Kazuyuki IZUNO

December 1992

Abstract

This dissertation is a fundamental study on seismic damage assessment and seismic retrofit of existing reinforced concrete structures. Earthquake response of existing structures were simulated using both experimental and analytical methods.

Firstly, effects of the different hysteretic models on damage assessment was studied to clarify how precise should the hysteretic rules for damage assessment be. Results showed that the non-degrading maximum value directed model was accurate enough for seismic damage analysis while the bilinear model underestimated damage because of its linear response to the low intensity cyclic loadings.

Secondly, seismic behavior of repaired RC members was investigated using hybrid experimental system called HYLSER (Hybrid Loading System of Earthquake Response). Results showed that the stiffness deterioration of the repaired specimens resembled that of the unrepaired originals when suitable repair methods were used. Energy-absorbing capabilities also were regained for adequately repaired specimens.

Thirdly, seismic response of a retrofitted RC structure was simulated numerically using fiber modeling technique extended to include the stress-strain relation of repair material such as grouted epoxy resin or covered steel plates. Analytically simulated seismic behavior was in good agreement with the experimental results. As an application of this method, earthquake response of a strengthened RC bridge pier was simulated, and effectiveness of thinner steel jackets was verified.

Finally, effectiveness of seismic isolator in retrofitting a RC bridge pier was studied using substructured hybrid experimental system. The isolated girder showed smaller acceleration response of the non-isolated structure, however, the maximum acceleration response of the isolated pier top was higher than the non-isolated pier because of its almost linear response of the isolated pier. Base shear force, absorbed hysteretic energy, ductility factor and the damage index decreased for the isolated structures.

Acknowledgements

I would like to express my sincere gratitude to Professor Yoshikazu Yamada and Associate Professor Hirokazu Iemura of Kyoto University for their invaluable supervision of my research, guidance, and encouragement throughout my research works for about nine years at Earthquake Engineering Laboratory of Department of Civil Engineering, Kyoto University.

I am indebted to Professor Manabu Fujii and Professor Eiichi Watanabe of Kyoto University for their critical review of the manuscript and their greatful help through my works.

I wish to acknowledge the revise of the papers by Dr. William Tanzo of Saitama University. He also helped me in the laboratory testings when he was a graduate student of Kyoto University.

I thank Professor Hitoshi Furuta, Dr. Masata Sugito, Dr. Junji Kiyono, Mr. Susumu Inoue and Mr. Makoto Kimura of Kyoto University for their kind help and continuous encouragement.

I would like to express my appreciation to Mr. Shinji Nakanishi and the students of Earthquake Engineering Laboratory, Department of Civil Engineering, Kyoto University, for their heartful help and friendship. Particulaly thanks are due to Mr. Shuhei Kohno, Mr. Koji Hama, Mr. Hiroyuki Geshi, Mr. Osamu Ohmoto, Mr. Toshiaki Ueno, Mr. Masatoshi Fukuda, Mr. Wataru Kurosawa, Mr. Hirotsugu Doi, Mr. Tadatoshi Furukawa, Mr. Tesuo Hirose, Mr. Masanori Hosokawa, Mr. Eiji Yamashita, Mr. Naoyuki Araki, Mr. Satoru Ohno, Mr. Hiroki Okada, Mr. Haruo Yoneyama, Mr. Toshiki Ohkawa, Mr. Kenji Baba, Mr. Satoru Fujisawa, Mr. Shigenori Kenzaka, Mr. Katsuhisa Ohmigishi and all students and almni of Earthquake Engineering Laboratory who worked with me.

I wish to acknowledge the aid in repair and cutting works of the test specimens by Mr. Masaru Shigeyoshi of Sho-Bond Construction Co., Ltd.

Lastly, I would like to thank my family for their heartful support and understanding.

December 1992, Kyoto *Kazuyuki Izuno*

Table of Contents

1. Introduction

1.1 General Remarks

Seismic damage analysis of existing reinforced concrete (RC) structures is important for the total lifeline system as well as for its own integrity. As revealed the damage analysis, many old structures constructed based on old codes need strengthening for future earthquakes. Moreover, some structures that were rendered nonfunctional due to earthquake damage could be reused after repair or strengthening of the damaged parts. Recently, repair and rehabilitation of the existing structures has become a world wide interest [1]. It is also important to determine how such repaired structures will respond during future earthquakes. The main objective of this research is to evaluate seismic vulnerability of the existing RC structures including retrofitted structures.

The first problem is how adequately we can evaluate damage of the structures. Many seismic safety indices have been proposed for RC structures, most of which use the ductility factor, absorbed hysteretic energy, or a combination of these two. These indices can be classified in 3 categories.

1. Indices using information about only earthquakes
   * *Maximum acceleration*: It is simple and often used, but has weak relation to damage.
   * *Maximum velocity*: It has some relation with damage of the structures.
   * *Characteristic intensity*: Park, Ang and Wen[2] proposed this index considering square mean value and duration of earthquake.

2. Indices using both information about earthquakes and structures
   * *Spectral intensity*: Housner[3] proposed this well known index, *SI*. It is defined as the integral of the velocity response spectrum for the natural period from 0.1 to 2.5 seconds. It has strong relation to the total damage of the specified area, however, it is not applicable to the damage assessment of the individual structure.
   * *Ductility Factor*: The ratio of the maximum displacement response to the yield deformation of the structure is widely used as an index of damage. However, this index cannot evaluate the effect of cyclic loadings in low level.
   * *Absorbed energy*: Total input energy to the structure, E, or the absorbed hysteretic energy, W, or the ratio, W/E can estimate the damage of the

structure. Many researchs have been done using both experimental and analytical methods. But the numerical relation between the damage level and the amount of absorbed energy is not clear yet.

* *Damage index*: Park, Ang and Wen[4] proposed the combined index of the maximum deformation and absorbed hysteretic energy. This index has strong relation to the damage of the specimens in laboratory tests. However, the empirical factor b has no theoretical background, and has to be defined from many experiments or field researches.
* *Damage function*: Stephens[5] proposed this index based on the low cycle fatigue theory and the maximum deformation. This index also has verified through laboratory tests.

3. Indices using information about only structures
   * *Stiffness degradation*: Stiffness of the damaged structures can be measured in field tests. Nishimura, Fujii, Miyamoto and Kagayama [6] measured stiffness of the several bridges and estimated damage of them.
   * *Natural period*: By measuring the elongated natural period of the bridge piers, Nishimura [7] evaluated the damage of old piers of railway bridges.
   * *Out-view*: Ministry of Construction summarized the manual [8] to judge the damage degree of the structures for retrofit work. The damage degree is evaluated from observation of damaged structures suffering cracks, spalling-off of concrete and rupture of main reinforcement.

Some of these indices are calculated using inelastic response analysis which requires an idealized hysteretic model of the structure. The more precise hysteretic model provides a more precise response at the expense of more calculation time.

For this reason, a simple hysteretic model like the bilinear model is often used to model the structures for damage assessment. Ando, Yamazaki and Katayama[9] studied the relation between the damage of the structures and the spectrum intensity of the earthquake through the earthquake response analysis using bilinear model. Hirao, Nariyuki, Sasada and Masui[10] estimated the damage related energy response spectrum using bilinear model.

However, different hysteretic models result in different earthquake responses. Minami and Osawa [11] evaluated difference of the elastic-plastic response spectra for several different hysteretic models. Sunasaka and Shimizu [12] calculated the index for damage of the structures using bilinear

model and degrading trilinear model. But how precise should the hysteretic model for damage analysis be is not clear.

For the retrofit problems of existing structures, the use of epoxy resin in repaired RC members and steel jackets in strengthening of RC structures have been found to be applicable and effective. The studies on the retrofit problems mainly carried out using experimental procedure. Yamamoto and Imai [13] applied epoxy resin injecting method to repair damaged RC buildings suffered by the 1978 Miyagi-Ken Oki earthquake. French, Thorp and Tsai [14] compared different epoxy repair techniques through the cyclic loading tests. Kawashima, Unjoh and Iida [15] conducted cyclic loading tests of strengthened RC piers using steel jacketing procedure. Though the cyclic loading tests give a basic inelastic behavior of retrofitted structures, it is difficult to simulate realistic behavior during earthquakes.

The research group for the U.S.-Japan cooperative earthquake engineering research program tested a full scale repaired building pseudo-dynamically [16]. Hybrid experiments (pseudo-dynamic tests) provide a very effective, powerful techniques with which to investigate the earthquake responses of such complicated materials as RC members and soils [17-20].

Although experimental studies provide reasonable earthquake response, analytical simulation is often needed for usual existing structures. Jordan and Kreger [21] studied strengthening of RC frames using several kinds of steel jackets analytically. Mahin and Moehle[22] described the factors that should be considered in the evaluation and retrofit of multi-column RC bridge bents. Badoux and Jirsa[23] analyzed static behavior of the RC frames strengthened with steel bracing for seismic retrofit. Miranda and Bertero [24] proposed post-tensioning technique for seismic upgrading of the existing buildings and showed its effectiveness using static and dynamic response analyses. Yamamoto and Umemura[25] static nonlinear response of RC frames retrofitted with a steel brace enclosed. Chandra, Bose and Nath[26] presented analytical study to upgrade old buildings designed before introduction of seismic code.

Recently, the collapse of bridge structures during the 1989 Loma Prieta earthquake brought a large concern on retrofit work, and many researches have been done on this area. Seible and Priestley [27] applied a preliminary damage and performance assessment procedure for the elevated roadways during the Loma Prieta earthquake, and proposed repair and retrofit solutions for the knee

joints. Ohuch, Matsuda and Goto [28] carried out numerical simulations on the collapse and retrofit of the Cypress Viaduct.

During the last decade, seismic retrofit using base isolation system has become of great interest especially for building structures [29-32]. Many buildings were already retrofitted using base isolation concepts. Although concepts of base isolation system was well known from historical ages, it is only with technological development in rubber material that made it applicable to even large and heavy structures [33, 34]. Use of base isolators in bridges is so far mainly limited to newly designed ones. Retrofit work of bridges using seismic isolators is still on the research stage. Buckle and Mayes [35] suggested use of the seismic isolators for bridge structures, and calculated its effect analytically. More plactical experimental studies are required to retrofit real bridges using seismic isolators.

These experimental and analytical studies made great progress on seismic retrofit of existing structures. However, a reasonable index to judge whether the structure can be retrofitted or has to be rebuild has not been established yet. In addition, to check whether the retrofitted structures could survive in future earthquakes is not evaluated precisely either.

1.2 Organization of the Study

This research aims a fundamental study on seismic damage assessment and seismic retrofit of existing RC structures. Earthquake response of existing structures were simulated using both experimental and analytical methods.

In Chapter 2, seismic damage was evaluated using several hysteretic models. Seismic damage was also estimated using several indices, and effect of different hysteretic models on damage assessment is discussed.

In Chapter 3, seismic behavior of repaired and/or strengthened RC members was tested using hybrid experimental system. A description of hybrid experiment procedure used to analyze retrofitted RC members under varying bending loads and constant axial force is presented. And experimentally simulated behavior of these members during earthquakes are discussed.

In Chapter 4, effectiveness of seismic retrofit for a damaged reinforced concrete structure repaired with grouted epoxy resin or steel jackets was quantified analytically using inelastic response analysis with the force-displacement relationship based on extended fiber model. Fiber modeling technique is basic and easy to apply for RC structures without complicated calculations such as nonlinear finite element methods. Hence, the proposed analytically method is easily applicable to the real retrofitted structures.

In Chapter 5, effectiveness of a seismic isolator in retrofitting a RC bridge pier was studied using hybrid experimental system and numerical simulations. A high-damping rubber (HDR) bearing was tested using substructured hybrid experimental system. The bridge pier was assumed as an analytical substructure while a seismic isolator was assumed as an experimental substructure. The results were then compared with the analytical response of the original non-isolated pier. The effectiveness of the isolator to the slightly damaged pier for retrofit work is also discussed in Chapter 5.

Finally, the concluding remarks of the whole chapters are summarized in Chapter 6.

References of Chapter 1

1) Bertero, V.V., "Seismic upgrading of existing structures", Proc. of the 10th World Conference on Earthquake Engineering, Madrid, Spain, Vol. 9, pp. 5101-5106, 1992.
2) Park, Y.J., Ang, A.H-S. and Wen, Y.K., *Seismic Damage Analysis and Damage-Limiting Design of RC Buildings,* Research Report, University of Illinois, Structural Research Series, No. 516, 1984.
3) Housner, G.W., "Behavior of structures during earthquakes", *Journal of Engineering Mechanics Division, ASCE,* Vol. 85, No. EM4, pp. 109-129, 1959.
4) Park, Y.J., Ang, A.H-S. and Wen, Y.K., "Mechanistic seismic damage model for reinforced concrete", *Journal of Structural Engineering, ASCE,* Vol. 111, No. 4, pp. 722-739, 1985.
5) Stephens, J., "A damage function using structural response", *Proc. of ASCE Convention,* 1985.
6) Nishimura, A., Fujii, M., Miyamoto, A. and Kagayama, T., "Sensitivity of mechanical behavior of bridges for their damage assessment", *Proc. of Japan Society of Civil Engineers,* No. 380/I-7, pp. 355-364, 1987 (in Japanese).
7) Nishimura, A, "Judgment of the structural integrity of bridge foundation with the percussion test for structure response", *Proc. of the 8th Japan Earthquake Engineering Symposium,* Vol. 2, pp. 2163-2168, 1990 (in Japanese).
8) Public Works Research Institute, *Manual for Repair Methods for Civil Engineering Structures Damaged by Earthquakes,* 1986 (in Japanese).
9) Ando, Y., Yamazaki, F. and Katayama, T., "Damage estimation of structures based on indices of earthquake ground motion", *Proc. of the 8th Japan Earthquake Engineering Symposium,* Vol. 1, pp. 715-720, 1990 (in Japanese).
10) Hirao, K., Nariyuki, Y., Sasada, S. and Masui J., "On the quantitative relation between effective Fourier spectrum of input earthquake motions and energy response spectrum of SDOF structures", *Proc. of Japan Society of civil Engineers,* No. 410/I-12, pp. 225-234, 1989.
11) Minami, T. and Osawa, Y., "Elastic-plastic response spectra for different hysteretic rules", *Earthquake Engineering and Structural Dynamics,* Vol. 16, pp. 555-568, 1988.
12) Sunasaka, Y. and Shimizu, Y., "A method of estimating aftershock effects on seismic damage of structures", *Proc. of the 8th Japan Earthquake Engineering Symposium,* Vol. 2, pp. 2037-2042, 1990 (in Japanese).

13) Yamamoto, Y. and Imai, H., "A case study on repair effect of an earthquake-damaged R/C structure repaired by injecting epoxy resin", *Proc. of the 30th Symposium on Structural Engineering*, pp. 153-161, 1984 (in Japanese).
14) French, C. W., Thorp, G. A. and Tsai, W.-J., "Epoxy repair techniques for earthquake damage", *ACI Structural Journal*, Vol. 87, No. 4, pp. 416-424, 1990.
15) Kawashima, K., Unjoh, S. and Iida, H., "Seismic inspection and seismic strengthening of reinforced concrete bridge piers with termination of main reinforcement at mid-height", *Proc. of the 1st U.S.-Japan Workshop on Seismic Retrofit of Bridges*, pp. 251-279, 1990.
16) Wight, J. K., ed., *Earthquake Effects on Reinforced Concrete Structures*, U.S.-Japan Research, SP-84, ACI, U.S.-Japan Research, 1985.
17) Hakuno, M. and Shidawara, M., "Dynamic failure tests of a member by an earthquake type external force", *Proc. of the 3rd Japan Earthquake Engineering Symposium*, pp. 675-682, 1970.
18) Iemura, H., "Development and future prospect of hybrid experiments", *Proc. of the Japan Society of Civil Engineers*, No.356/I-3, pp. 1-10, 1985 (in Japanese).
19) Takanashi, K. and Nakashima, M., "Japanese activities on on-line testing", *Journal of Engineering Mechanics, ASCE,* Vol. 113, No. 7, 1987.
20) Mahin, S. Shing, P.B., Thewalt, C. and Hanson, R., "Pseudodynamic test method — Current status and future directions", *Journal of Structural Engineering, ASCE,* Vol. 115, No. 8, 1989.
21) Jordan, R. M. and Kreger, M. E., "Evaluation of strengthening schemes and effects on dynamic characteristics of reinforced concrete frames", *Proc. of the 4th U. S. National Conference on Earthquake Engineering*, Vol. 3, pp. 363-372, 1990.
22) Mahin, S.A. and Moehle, J.P., "Assessment and retrofit research for multi-level, multi-column bents", *Proc. of the 1st U.S.-Japan Workshop on Seismic Retrofit of Bridges*, pp. 175-186, 1990.
23) Badoux, M. and Jirsa, J.O., "Steel bracing of RC frames for seismic retrofitting", *Journal of Structural Engineering*, ASCE, Vol. 116, No. 1, pp. 55-74, 1990.
24) Miranda, E. and Bertero, V.V., "Post-tensioning technique for seismic upgrading of existing low-rise buildings", *Proc. of the 4th U. S. National Conference on Earthquake Engineering*, Vol. 3, pp. 393-402, 1990.
25) Yamamoto, Y. and Umemura, H., "Analysis of reinforced concrete frames retrofitted with steel brace", *Proc. of the 10th World Conference on Earthquake Engineering*, Madrid, Spain, Vol. 9, pp. 5187-5192, 1992.
26) Chandra, B., Bose, P.R. and Nath, B.C., "Analytical study of seismically

vulnerable RC buildings and their strengthening", *Proc. of the 10th World Conference on Earthquake Engineering*, Madrid, Spain, Vol. 9, pp. 5149-5154, 1992.

27) Seible, F. and Priestley, M.J.N., "Damage and performance assessment of existing concrete bridges under seismic loads", *Proc. of the 1st U.S.-Japan Workshop on Seismic Retrofit of Bridges*, pp. 203-222, 1990.
28) Ohuchi, H., Matsuda, T. and Goto, Y., "A study on the Cypress Viaduct collapse and seismic performance of a retrofitted bent", *Proc. of the Japan Society of Civil Engineers*, No. 446/I-19, pp. 77-88, 1992.
29) Takeda, T., ed., *Kozobutsu no Menshin, Boshin, Seishin,* Giho-do Shuppan, 1988 (in Japanese).
30) Braga, F. and Zampino, G., "Seismic isolatin of the ancient Bell-Tower of Melfi", *Proc. of the 10th World Conference on Earthquake Engineering*, Madrid, Spain, Vol. 4, pp. 2301-2304, 1992.
31) Keshtkar, H.E. and Hanson, R.D., "Rehabilitation of buildings using multiple levels of passive control", *Proc. of the 10th World Conference on Earthquake Engineering*, Madrid, Spain, Vol. 9, pp. 5155-5158, 1992.
32) Delfosse, G.C. and Delfosse, P.G., "Seismic rehabilitation of a shear wall building by means of base isolation", *Proc. of the 10th World Conference on Earthquake Engineering*, Madrid, Spain, Vol. 9, pp. 5159-5162, 1992.
33) Kelly, J., "Aseismic base isolation: Review and bibliography", *Soil Dynamics and Earthquake Engineering*, Vol. 5, No. 3, pp. 202-216, 1986.
34) Izumi, M., "State-of-the-Art Report: Base isolation and passive seismic response control", *Proc. of the 9th World Conference on Earthquake Engineering*, Tokyo–Kyoto, Japan, Vol. VIII, pp. 385-396, 1988.
35) Buckle, I. G. and Mayes, R. L., "Seismic retrofit of bridges using mechanical energy dissipators", *Proc. of the 4th U.S. National Conference on Earthquake Engineering*, Vol. 3, pp. 305-314, 1990.

2. Seismic Damage Assessment of RC Structures using Different Hysteretic Models

2. 1 General Remarks

Estimation of seismic damage of a structure varies depending on the assumed hysteretic rules and input excitations due to indices being calculated from earthquake response time histories. Different hysteretic models result in different earthquake responses [1)], but how precise hysteretic model is required for damage analysis is not clear.

In this chapter, seismic damage was evaluated using several hysteretic models, assuming that the most precise hysteretic model always gives the right damage assessment. The first part of this chapter describes the effect of hysteretic models on the damage index, and the latter part discusses the effect of hysteretic models on the damage spectra.

2. 2 Hysteretic Models for Force-Deformation Relation

Linear analysis is valid in cases of small response of the structure, and is widely used such as the response spectra method because of its convenience in calculation. However, nonlinear analysis is needed in designing important structures, to check the response during a large future earthquake. In the analysis of real structures, an idealization of their hysteretic behavior is essential, and many idealized hysteretic models have been proposed.

In this study, a skeleton curve was assumed as piecewise linear as shown in **Figure 2.1**. Cracks occur in concrete at point C; reinforcing bars yield at point Y; restoring force shows its maximum value at point M; and the structure collapses at point U. In the following, the four hysteretic models used in this analysis are described. A schematic diagram for each model is shown in **Figure 2.2**.

(a) Linear model

Restoring force relates linearly to the deformation as shown in **Figure 2.2-a**. Initial stiffness (line O-C in **Figure 2.1**) was used for the constant stiffness in the simulation. Although a linear model is seldom used in damage analysis, a simulation was carried out in this study to compare its behavior to the other nonlinear models.

(b) Bilinear model

The bilinear model is the simplest nonlinear model that has two stiffnesses to represent elastic and inelastic behavior as shown in **Figure 2.2-b**. Response may change depending on the connecting point of two stiffness lines. In this study, line O-C and line Y-M in **Figure 2.1** represent two stiffnesses, and the crossing point of these two lines is defined as point A in **Figure 2.2-b**.

(c) 3-parameter model

Park, Reinhorn and Kunnath [2)] proposed this degrading trilinear type hysteretic model as shown in **Figure 2.2-c** for RC structures. The three parameters represent stiffness deterioration, strength deterioration and pinching effect due to the shear cracks. There are many other degrading trilinear models, however, this model was selected in this study because of its strong relation to the damage index which is to be mentioned in the next section. Response based on this model was considered to be true in this study because of the assumption that the most precise hysteretic model always derives the most correct response. The three parameters were set to α=3.0, β=0.62 and γ=1.0 according to reference 2.

(d) Maximum value directed model

An ordinal degrading trilinear model shown in **Figure 2.2-d** was also discussed. To distinguish it from the 3-parameter model clearly, this model is called maximum value directed model in this study. The hysteretic curve of this model directs its previous maximum or minimum point. Although the 3-parameter model shown above gives the precise response, the necessary parameters are difficult to determine exactly. The maximum value directed

model neglects behavior that the 3-parameter model precisely describes; however, it shows that the stiffness deterioration during the loading process is a dominant parameter in determining the global shape of hysteretic load-deformation responses.

2. 3 Damage Indices using Different Hysteretic Models

Using the four hysteretic models described in the previous section, the response of an RC bridge pier was simulated. The model has dimensions of 2 m in diameter, 13 m in height, 100 tonf (0.98 MN) in weight and 250 tonf (2.45 MN) in reaction force of the beams. It was modeled as an SDOF system whose restoring force-deformation relation at its top during one direction loading is shown in **Figure 2.1**, as described in the previous section. Its initial natural frequency was calculated to 2 Hz and the damping ratio of 5% was assumed.

2. 3. 1 Damage Index

Many indices have been proposed for seismic damage analysis; some of them use ductilities, some use only hysteretic energy and the others use a combination of ductility and energy. During an earthquake, RC structures may incur large deformations in one direction as well as undergo cyclic deformations. Park, Ang and Wen proposed the "damage index" in the form of a linear combination of a deformation term and a hysteretic energy term as follows [3]:

$$D = \frac{\delta_m}{\delta_u} + \frac{\beta}{P_y \delta_u} \int dE \qquad (2.1)$$

in which D is the damage index, δ_m is the maximum deformation, δ_u is the ultimate deformation, P_y is the yield strength, $\int dE$ is the absorbed hysteretic energy and β is an empirical coefficient. A damage index of more than 1 represents severe damage or collapse. Among the many indices used to evaluate damage of the structures, the maximum deformation, absorbed hysteretic energy and the linear combination of these two are the basic indices.

2. 3. 2 Input Motions

As input motions affect the response of the structures, several sinusoidal waves and four earthquake records were used in this analysis. The earthquake records used are: the NS component of the El Centro record at the 1940 Imperial valley earthquake, the NS component of the Hachinohe record at the 1968 Tokachi-Oki earthquake, the NS component of the Akita record at the 1983 Nihonkai-Chubu earthquake and the EW component of the SCT record at the 1985 Mexico earthquake.

Figure 2.3 shows their acceleration time histories and **Figure 2.4** shows their response spectra for 5% damping. The SCT record of **Figure 2.3-d** shows a sinusoidal wave form which may induce a resonance response in a structure with a natural period of 2 seconds, while the other 3 records affect the structures in the shorter natural period range. The El Centro record has a relatively short duration of its main shock.

To see the effect of the strength of the input motions, amplification factors of 0.5, 1.0 and 1.5 were used for each input motion.

2. 3. 3 Numerical Simulation on Damage Index

Figure 2.5 shows examples of the hysteretic force-deformation response of each model for the case of the El Centro record. Damage indices for various earthquake records are shown in **Figure 2.6**. They show different tendencies for different input motions. **Figure 2.7** shows the damage indices for the sine waves whose period is from 0.2 to 3.0 seconds. Lines for the linear and the bilinear models show lines similar to the resonance curve.

Further, **Figure 2.8** shows the ratio of the first and the second terms of the damage index, which represent damage due to large deformation and to hysteretic energy, respectively. This figure does not include the linear model because its 2nd term makes no contribution to the damage index. The damage index - time histories are shown in **Figure 2.9**.

(a) Linear model

As the response of the linear model shows no hysteretic behavior and the

deformation is also small compared with other nonlinear models, the damage index is too small in every case. The linear model should not be used in damage analysis.

(b) Bilinear model

The damage index of the bilinear model shows quite different behavior if its response enters the second stiffness or not. If the response does not overcome its yield level as for the SCT record scaled to 0.5 or 1.0 times (**Figure 2.6-d**), the damage index is the same as the linear model. For the sine wave input shown in **Figure 2.7**, it shows the same values as the linear model for small response. However, once the resonance occurs, it shows a larger value than even the 3-parameter model because of its parallelogram shaped hysteretic load-deformation responses shown in **Figure 2.5-b**; i.e., it can absorb more hysteretic energy than the degrading type hysteresis response of **Figure 2.5-c**.

As in **Figures 2.8-a** and **2.8-b**, the ratio between 1st and 2nd terms differs from that in the bilinear and the 3-parameter models. The deformation of the bilinear model is smaller than of the other models in every case which is shown as a solid bar in **Figure 2.8**.

They showed almost the same value for only the El Centro record. There are 2 possible reasons for this phenomena: one is that the dominant period of this record covers the natural period of the assumed model, and the other is its impulsive wave form. **Figure 2.10-a** shows the damage index to a filtered white noise from 1 to 3 Hz which covers the natural period of the model (2 Hz), and **Figure 2.10-b** shows the response to an impulse scaled to 5000 gal. The damage index of the bilinear model and of the 3-parameter model to the filtered white noise showed different values, and the index to the strong impulse showed almost the same values. Thus, this phenomena was caused by the impulsive input motion. The bilinear model estimates the damage with accuracy only for an impulsive input motion.

Furthermore, as the hysteretic loops remained open for weak input motion, the damage due to small cyclic response after the main large response was neglected. This was observable in **Figure 2.9** which shows the damage index time histories. The damage index of the 3-parameter model abruptly increased when the input motion showed the maximum acceleration because of the large inelastic deformation. The damage index continued increasing after the large deformation with the result that damage even for the small cyclic response was

evaluated. On the contrary, the damage index of the bilinear model remained at the same value after the large deformation.

As a result, the bilinear model usually underestimates damage when compared with the 3-parameter model.

(c) Maximum value directed model

As shown in **Figure 2.6**, the difference between the 3-parameter model and the maximum value directed model was at most 3% except when the SCT record was scaled to 1.5 times larger. The judgment, from the damage index, of whether the structure will collapse or not was the same in every simulation. They also showed almost the same values for the sinusoidal waves shown in **Figure 2.7**.

For the SCT record scaled to 1.5 times larger, the area of the hysteresis loops became small for the 3-parameter model compared with the maximum value directed model because of the stiffness degrading in the unloading process and the strength degradation due to absorbed hysteretic energy. This was also observed from the ratio of the 1st term to the 2nd term as shown in **Figure 2.8-c**. The damage index according to the maximum value directed model may differ from the 3-parameter model for the waves which cause numerous large deformations, however, the indices from both models exceeds 1.0 for these strong input motions which result in the same judgment of the structure as totally collapsed. Thus, the maximum value directed model is accurate enough for seismic damage analysis provided that precise earthquake response is unessential.

2. 3. 4 Relation Between the Indices for Earthquake Motions and the Damage Index

Calculation of the damage index requires the time histories of the restoring force and the deformation which are usually estimated from inelastic response analysis. Therefore, a simple equation which approximates the damage index from another simple index of input motion is valid for utilizing the damage indices. In this section, the maximum velocity of the input motion v_{max} and the spectrum intensity SI [4], which are considered to have a high correlation with damage to the structure, are calculated in order to find a correlation with the

damage index using different hysteretic models.

Figure 2.11 shows the correlation between the damage index and the maximum velocity of the input motions v_{max}, and **Figure 2.12** shows the correlation between the damage index and the spectrum intensity *SI*. The spectrum intensity is defined as follows [4].

$$SI = \int_{0.1}^{2.5} S_V(h,T)dT \tag{2.2}$$

in which, h is a damping factor, T is a natural period of a structure and S_V is a velocity response spectrum.

The x-axes of these figures represent v_{max} or *SI* of each earthquake record scaled to 0.5, 1.0 and 1.5 times larger than the original record, and they were sorted according to their values regardless of earthquakes. As the SCT record has somewhat special wave form from the other general earthquake records due to its special ground condition, **Figures 2.11-b** and **2.12-b** were plotted with the results for the SCT records excluded while **Figures 2.11-a** and **2.12-a** were plotted using all records.

As the maximum velocity v_{max} or the spectrum intensity increases to a certain level, the damage index abruptly increases. Although the relationship is nonlinear, linear regression was used in this study because the total number of data are not enough for nonlinear analysis.

The correlation coefficient using the 3-parameter model for the damage index and the maximum velocity v_{max} is 0.85 for the case using all records and 0.9 for the case excluding the SCT record, which is high enough to assume linear function between them. As the maximum velocity exceeds 40 kine, the damage index reached 1 in **Figure 2.11**.

The correlation between the damage index and the spectrum intensity *SI* is also high to have a correlation coefficient of 0.8. *SI* is more suitable to be used for the assessment of general structures located in a wide area than of the individual structure as in this study, because *SI* is defined as the mean velocity response of the structures with natural periods of from 0.1 to 2.5 seconds. The relation of the maximum velocity or the spectrum intensity and the damage index estimated using the bilinear model showed less correlation than the 3-parameter model. Furthermore, the damage index evaluated from v_{max} or *SI* usually showed smaller values than the 3-parameter model, while the maximum

value directed model could be used to estimate an index similar to the 3-parameter model. The bilinear model is inadequate to evaluate the relation between the damage index and an index of the input motion.

Because both the maximum velocity and the spectrum intensity are indices only for the input motion, analysis capable of considering information about the structure is needed especially for special wave forms such as the SCT record.

2. 4 Damage Spectra using Different Hysteretic Models

2. 4. 1 Damage Spectra

In this section, damage of the structures with various natural periods was expressed as the damage spectrum. The damage spectrum can be defined for any index related to damage such as ductility, absorbed hysteretic energy, or the damage index, as a function of the natural period of structure. This section studies the response of the structure model which satisfies the design code subjected to the design earthquake motion.

A skeleton curve assumed as a perfectly elasto-plastic model (**Figure 2.13**) which satisfies the Japanese seismic code for highway bridges [5], was used because of its simplicity. However, the following discussion is valid not only for the perfectly elasto-plastic model but also for arbitrary elasto-plastic model if the stiffness in the plastic range is given. First, the maximum restoring force $P_y = P_u$ was defined to satisfy the horizontal seismic load as follows:

$$\frac{P_y}{m} = \frac{P_u}{m} = k_h \cdot g \tag{2.3}$$

in which, m is the mass of the structure, g is the gravitational acceleration, k_h is the design horizontal seismic coefficient determined by the following equation:

$$k_h = c_Z \cdot c_G \cdot c_I \cdot c_T \cdot k_{h0} \tag{2.4}$$

in which, c_Z is a modification factor for zone, c_G is a modification factor for ground condition, c_I is a modification factor for importance, c_T is a

modification factor for structural response and k_{h0} is a standard design horizontal seismic coefficient which is set to 0.2. k_h should not be less than 0.1.

Using a circular natural frequency ω, the yield deformation δ_y is written as follows:

$$\delta_y = \frac{P_y}{m \cdot \omega^2} \tag{2.5}$$

The ultimate deformation is determined by checking the bearing capacity of RC piers for lateral force. The ultimate strength should satisfy the following equation:

$$\frac{P_u}{m} = k_{he} \cdot g \tag{2.6}$$

in which, k_{he} is an equivalent horizontal seismic coefficient to be checked for bearing capacity of RC piers for lateral force, determined using the next equation:

$$k_{he} = \frac{k_{hc}}{\sqrt{2\mu - 1}} \tag{2.7}$$

in which, μ is an allowable ductility factor, k_{hc} is the horizontal seismic coefficient for checking bearing capacity determined from the following equation:

$$k_{hc} = c_Z \cdot c_I \cdot c_R \cdot k_{hc0} \tag{2.8}$$

in which, c_Z and c_I are the same modification factors as Eq. (2.4), c_R is a modification factor for structural response and k_{hc0} is a standard horizontal seismic coefficient set to 1.0.

From Eqs. (2.3), (2.7) and (2.8), the required ductility factor is derived as follows:

$$\mu = \frac{1}{2}\left(\frac{k_{hc}}{k_h}\right)^2 + \frac{1}{2} \tag{2.9}$$

Let the structure be assumed to collapse in flexural failure, the ultimate deformation is derived as follows:

$$\delta_u = (1 + \mu \cdot \alpha - \alpha) \cdot \delta_y \tag{2.10}$$

in which, α is a safety factor set to 1.5.

Using this procedure, a skeleton curve for a structure with an assumed natural period is determined in the form of deformation – restoring force per unit mass. In this study, c_Z and c_I are set to 1.0, and the other factors are determined for each ground conditions: stiff, medium and soft. A suitable input earthquake record is selected based on the seismic code for each soil condition [5]. In this study, the recommended earthquake record for stiff soil is called Type 1, medium soil is called Type 2 and soft soil is called Type 3. They were multiplied 3 times to check the ultimate behavior of structures.

All parameters for the 3-parameter model were set to 1.0 to make the model undergo a heavy degrading process for the purpose of accentuating the differences among the hysteretic models.

2. 4. 2 Numerical Simulations on Damage Spectra

Figure 2.14 shows the damage spectra for the ductility factor, **Figure 2.15** shows the damage spectra for the absorbed hysteretic energy normalized by the total input energy, and **Figure 2.16** shows the damage spectra for the damage index. In **Figure 2.16**, the lines for β=0.0 are also plotted giving the contribution of only the 1st term of the damage index. As the 1st term and the 2nd term are added linearly, a damage index corresponding to any value of β can be interpolated from this figure.

(a) The maximum value directed model

The maximum value directed model underestimated ductility factors of less than 10% for short period structures (**Figure 2.14**). In addition, it showed the same estimates as the 3-parameter model for the structures whose natural period is longer than 1.0 second on stiff ground (**Figure 2.14-a**), longer than 1.3 seconds on medium ground (**Figure 2.14-b**), and longer than 1.5 seconds

on soft ground (**Figure 2.14-c**).

On the contrary, this model overestimated hysteretic energy in the short period range (**Figure 2.15**). This difference was caused by the strength degradation process existing in the 3-parameter model due to the large deflection. For the structures whose natural period is longer than 2.0 seconds, this model showed the same estimates of the absorbed hysteretic energy as the 3-parameter model.

This model gave the same damage index as the 3-parameter model (**Figure 2.16**). As the 1st term of the damage index is defined as the ratio of the maximum deformation to the ultimate deformation instead of to the yield deformation similar to the ductility factor, the difference in the ductility factor had little effect on the damage index. Furthermore, the 1st term of the damage index gave smaller values than the 3-parameter model to the short period structures and the 2nd term gave larger values, resulting in a smaller difference as a total. The difference between the maximum value directed model and the 3-parameter model was less than 5%.

(b) The bilinear model

The bilinear model underestimated the ductility factor by about 20% in the short period range, and overestimated it at most 20% for the long period range (**Figure 2.14**). This model is the same as the linear model unless the deformation becomes larger than the yield point. It shows abrupt change of its nature around the yield point.

The bilinear model underestimated the normalized ratio of the hysteretic energy to the total input energy by at most 20% in the range of periods longer than 1.0 second, and overestimated it in the shorter period (**Figure 2.15**).

The bilinear model also underestimated the damage index (**Figure 2.16**). The judgment for vulnerability of whether the structure will collapse or not is almost the same as with the 3-parameter model. However, the index according to the bilinear model should be handled carefully because the index showed only half the value of the 3-parameter model for some periods.

2. 5 Conclusions

The effects of the different hysteretic models on the damage index were studied. On the assumption that a precise inelastic hysteretic model called the 3-parameter model will show the real damage to the RC structures, more simple hysteretic models were examined for their ability to approximate the damage index and the damage spectra. The main conclusions are as follows:

(1) The bilinear model usually underestimates the damage index compared with a precise hysteretic model such as the 3-parameter model. Damage assessment of RC structures requires at least the maximum value directed model.

(2) The maximum value directed model approximates the damage index to within 5% accuracy except for an input motion with numerous cyclic waves of large amplitude such as the SCT record of the 1985 Mexico earthquake. However, the decision of whether the structure will collapse or not is the same as with the 3-parameter model, even for the SCT record. Degrading of the strength and unloading stiffness due to the cyclic loadings can be neglected for damage analysis unless a precise earthquake response is needed.

(3) The damage index can be evaluated with high accuracy from the maximum velocity or the spectrum intensity of the input motion. However, the relation between the index of the input motion and the damage index using the bilinear model showed less correlation than the 3-parameter model, whereas the maximum value directed model showed the same high correlation as the 3-parameter model. The bilinear model is inadequate to evaluate the relation between the damage index and an index of the input motion.

(4) The damage spectra for the damage index, ductility and the normalized hysteretic energy were calculated using the bilinear model, the maximum value directed model, and the 3-parameter model. The damage spectra using the maximum value directed model showed errors of at most 10% compared with the 3-parameter model, while the bilinear model underestimated or overestimated the damage spectra by at most 50%. The damage spectra for ductility and the hysteretic energy should be calculated using a precise hysteretic model, and at least the maximum value directed model for the damage index spectra.

References of Chapter 2

1) Minami, T. and Osawa, Y., "Elastic-plastic response spectra for different hysteretic rules", *Earthquake Engineering and Structural Dynamics*, Vol. 16, pp. 555-568, 1988.
2) Park, Y.J., Reinhorn, A.M. and Kunnath S.K., "Seismic damage analysis of reinforced concrete buildings", *Proc. of the 9th World Conference on Earthquake Engineering*, Japan, Vol. VII, pp. 211-216, 1988.
3) Park, Y.J., Ang, A.H-S. and Wen, Y.K., "Mechanistic seismic damage model for reinforced concrete", *Journal of Structural Engineering, ASCE*, Vol. 111, No. 4, pp. 722-739, 1985.
4) Housner, G.W. , "Behavior of structures during earthquakes", *Journal of Engineering Mechanics Division, ASCE*, Vol. 85, No. EM4, pp. 109, 1959.
5) Japan Road Association, *Seismic Design Code, Specifications for Highway Bridges in Japan*, Part V, 1990 (in Japanese).

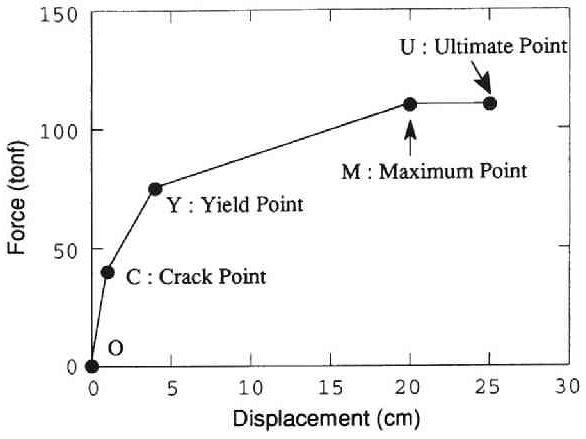

Figure 2.1 Force-deformation curve for RC member.

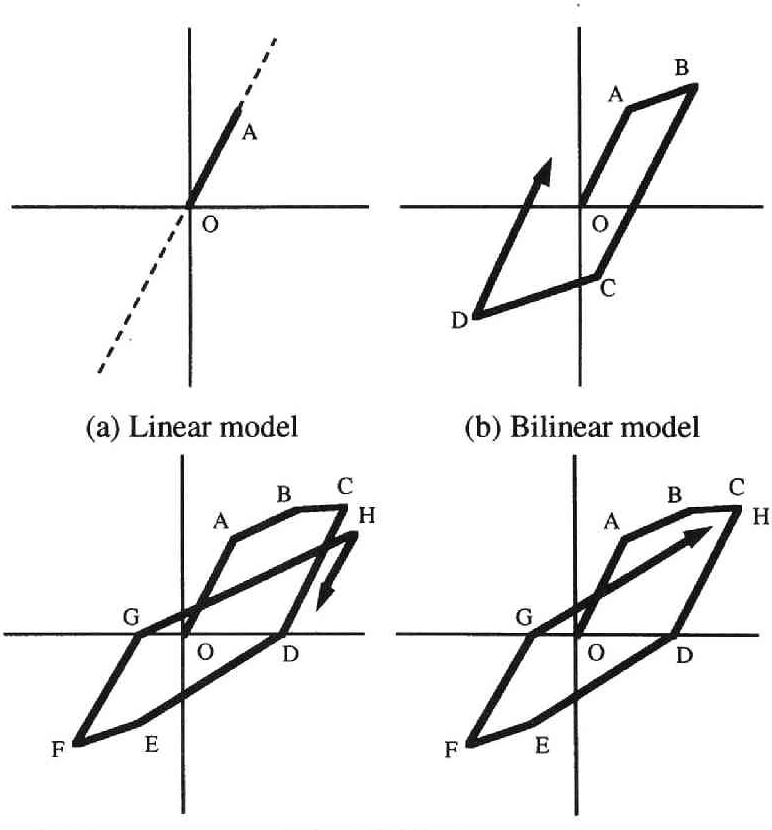

(a) Linear model (b) Bilinear model

(c) 3-parameter model (d) Maximum value directed model

Figure 2.2 Hysteretic models used in analysis.

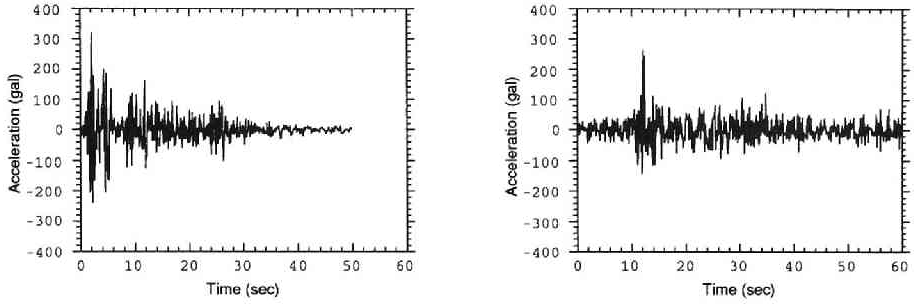

(a) El Centro (b) Hachinohe

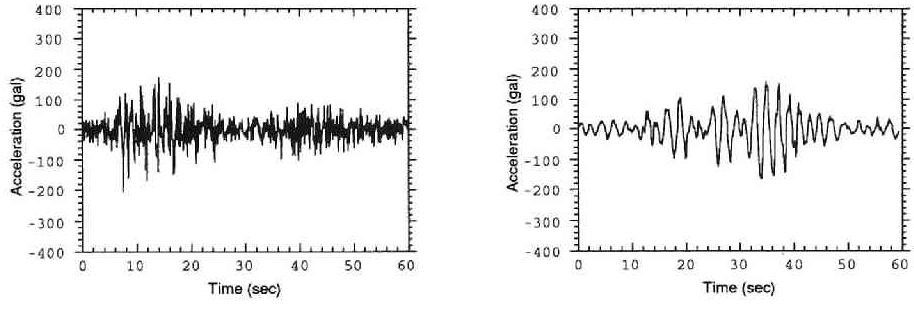

(c) Akita (d) SCT

Figure 2.3 Earthquake records used in this study.

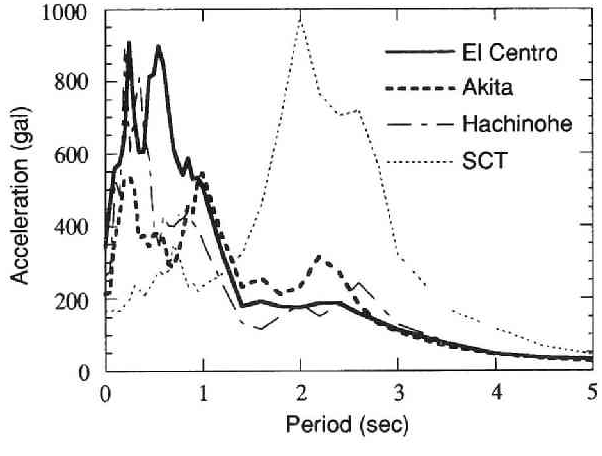

Figure 2.4 Response spectra of input motions.

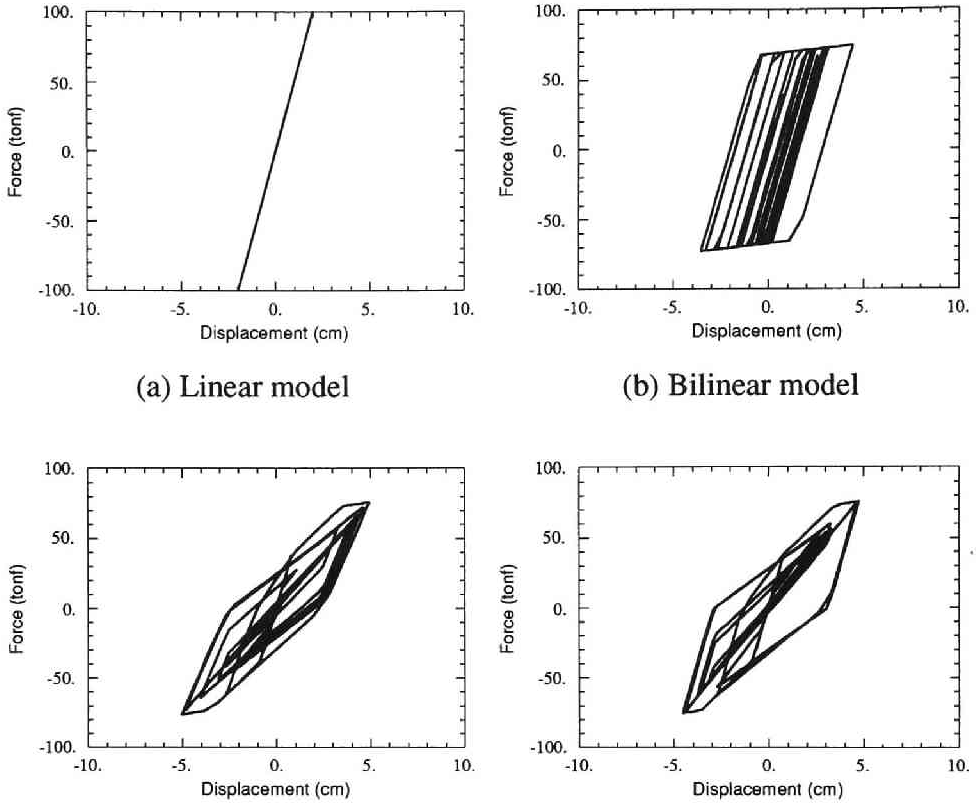

(a) Linear model (b) Bilinear model

(c) 3-parameter model (d) Maximum value directed model

Figure 2.5 Hysteretic responses for the El Centro record.

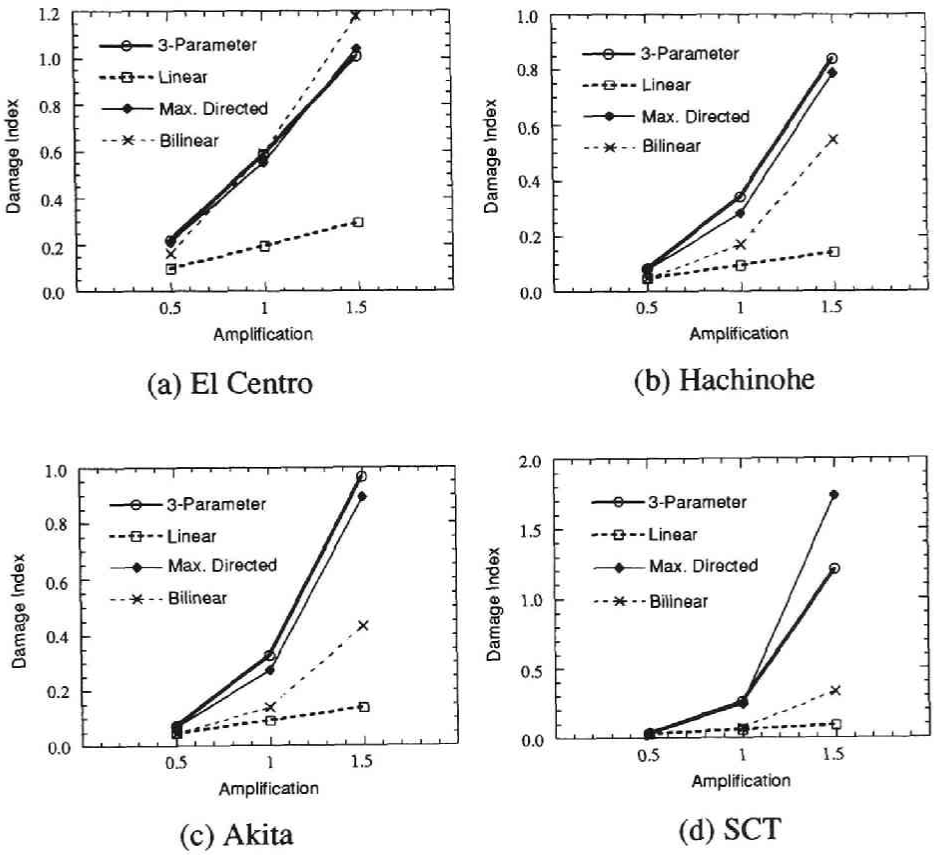

Figure 2.6 Damage index for different hysteretic models and input motions.

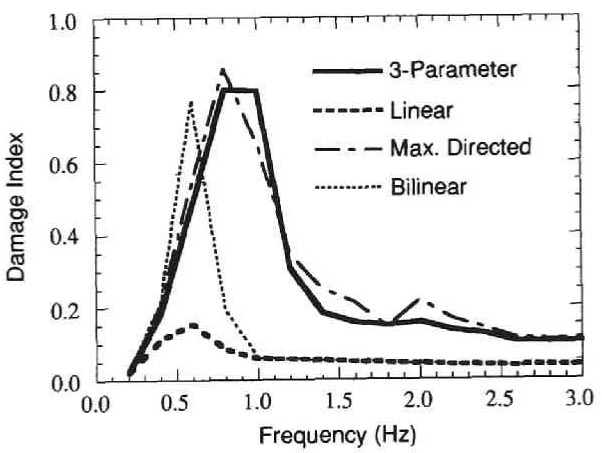

Figure 2.7 Damage index for various periods of sinusoidal excitations.

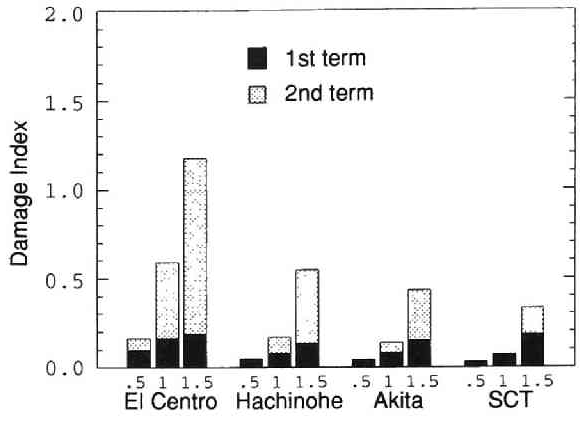

(a) Bilinear model

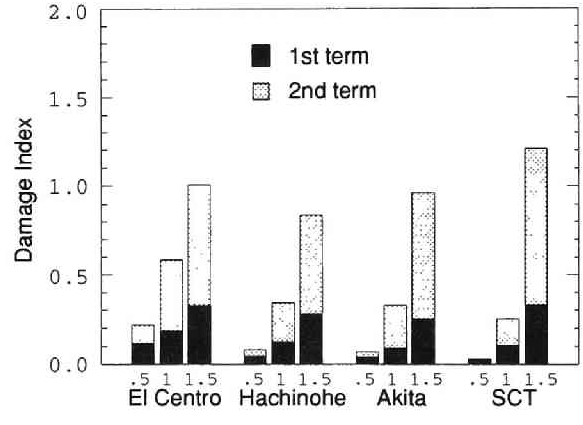

(b) 3-parameter model

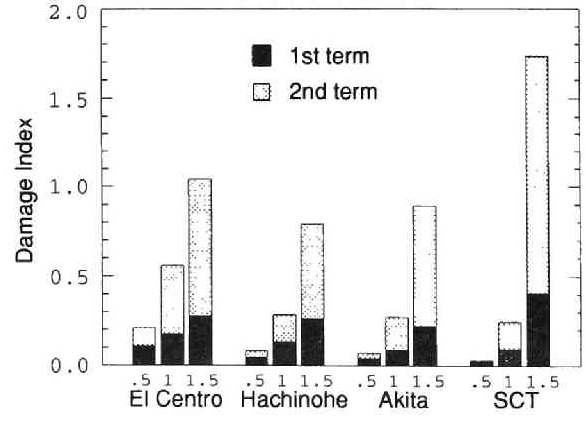

(c) Maximum value directed model

Figure 2.8 Ratio of 1st and 2nd terms of damage index.

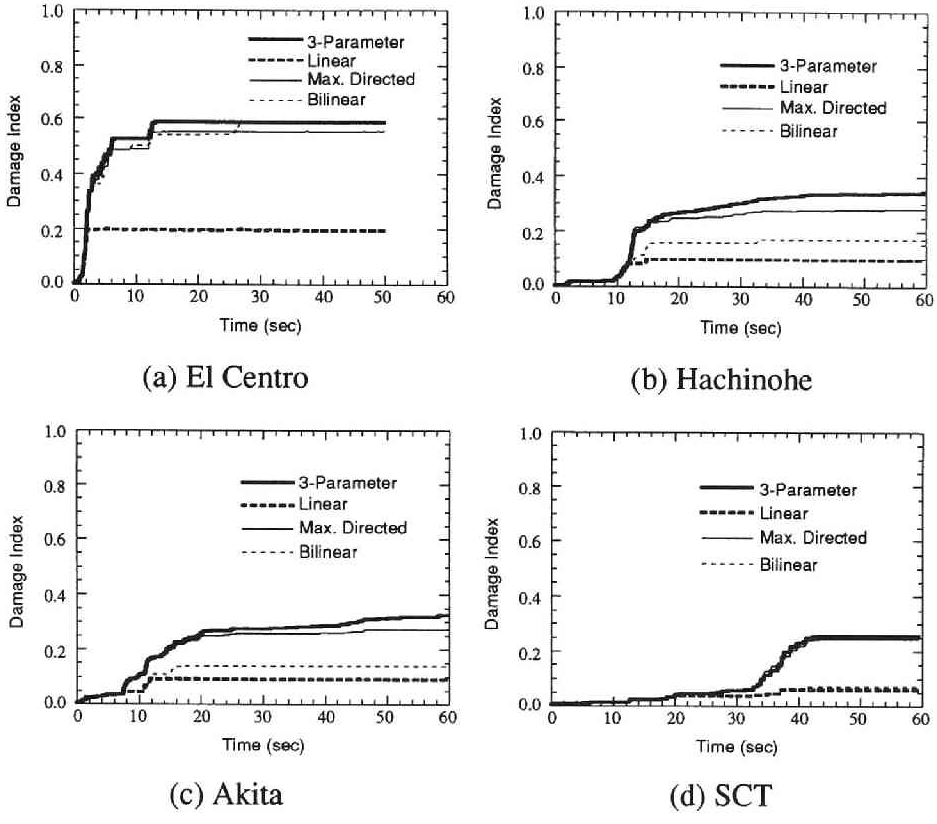

Figure 2.9 Damage index time histories of different hysteretic models.

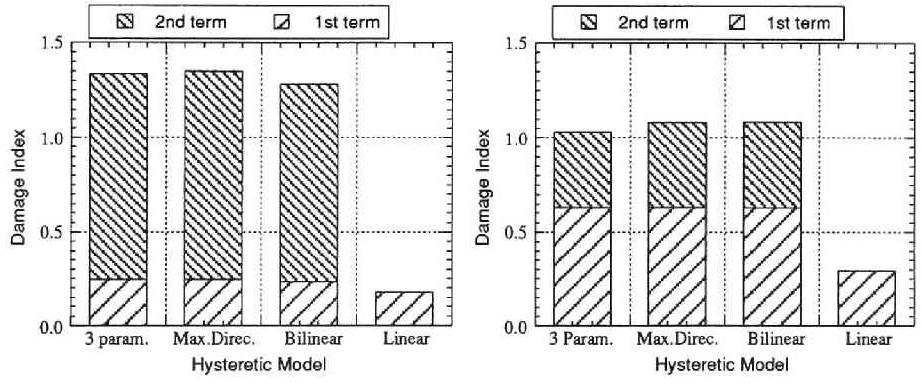

Figure 2.10
Ratio of 1st and 2nd terms of damage index for different input motions.

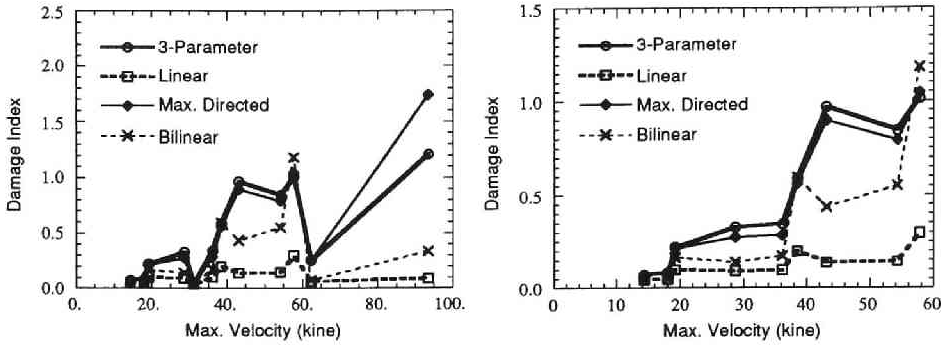

(a) Using all data (b) Excluding SCT records

Figure 2.11
Relation of damage index to the maximum velocity of input motions.

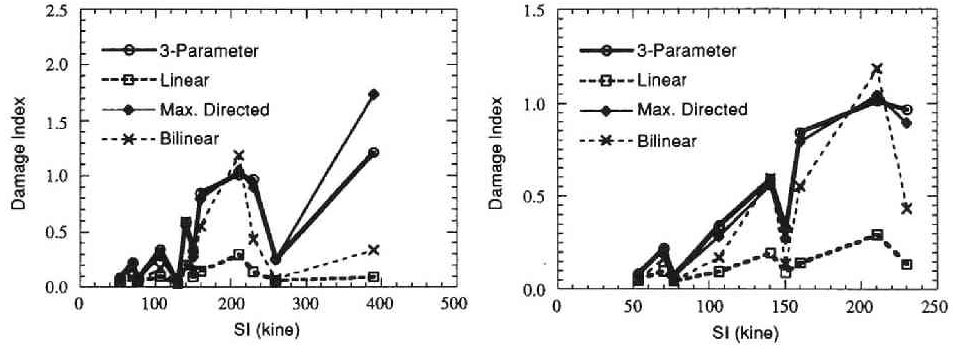

(a) Using all data (b) Excluding SCT records

Figure 2.12 Relation of damage index to spectral intensity; SI.

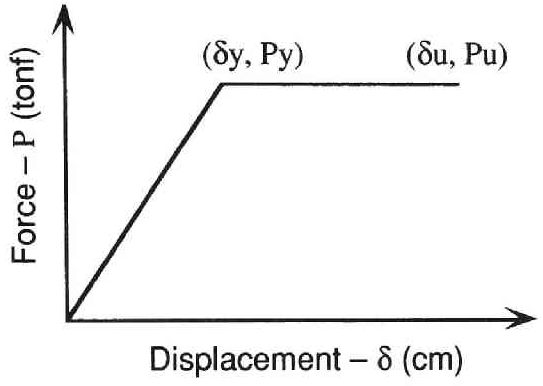

Figure 2.13 Perfectly elasto-plastic model assumed for damage spectra.

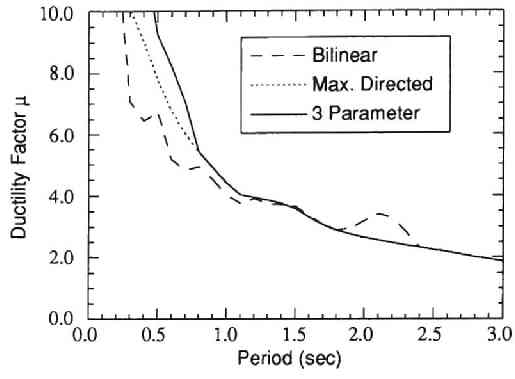

(a) Type 1 earthquake

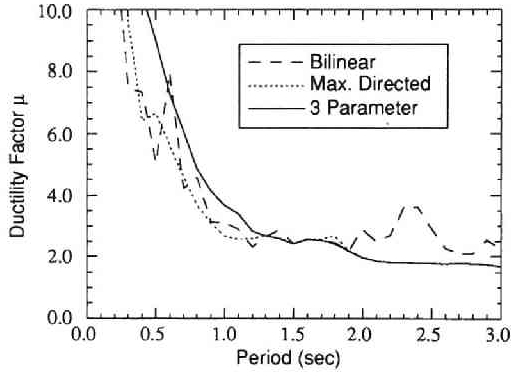

(b) Type 2 earthquake

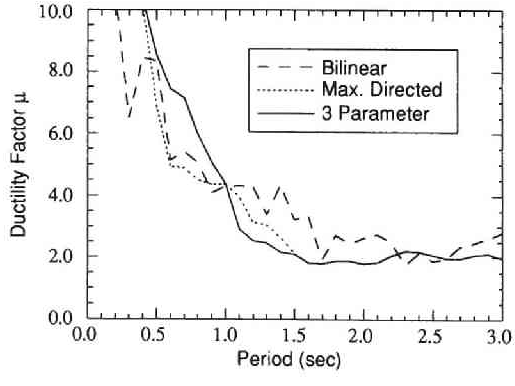

(c) Type 3 earthquake

Figure 2.14 Damage spectra for ductility factor.

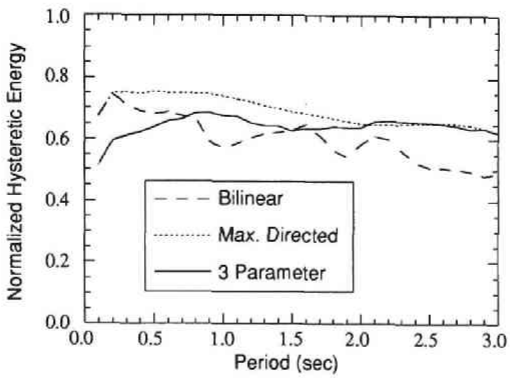

(a) Type 1 earthquake

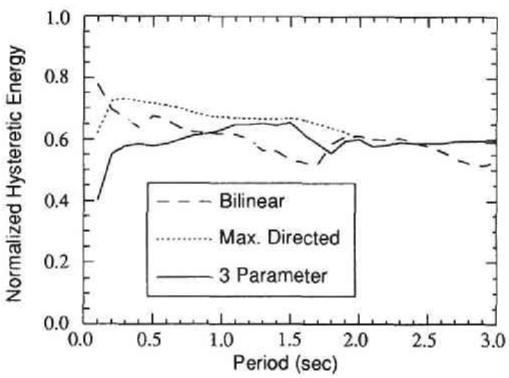

(b) Type 2 earthquake

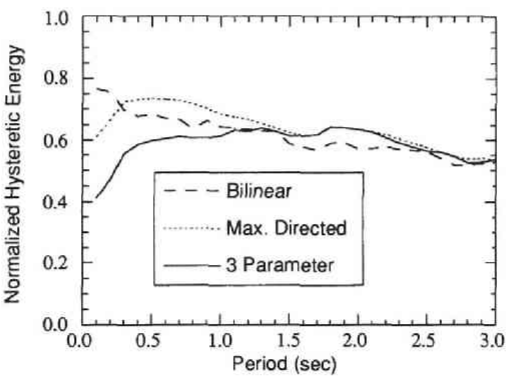

(c) Type 3 earthquake

Figure 2.15 Damage spectra for absorbed hysteretic energy.

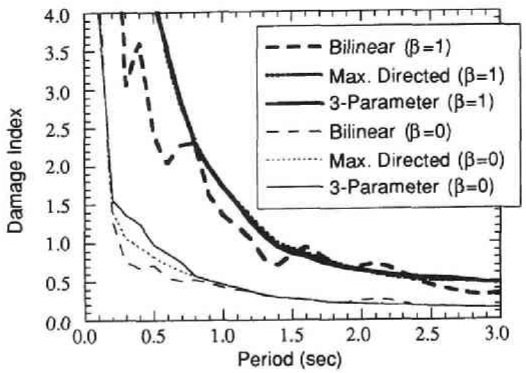

(a) Type 1 earthquake

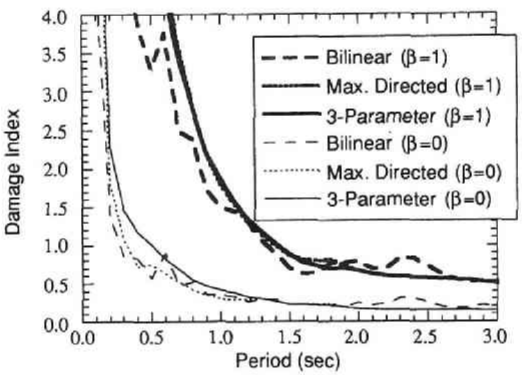

(b) Type 2 earthquake

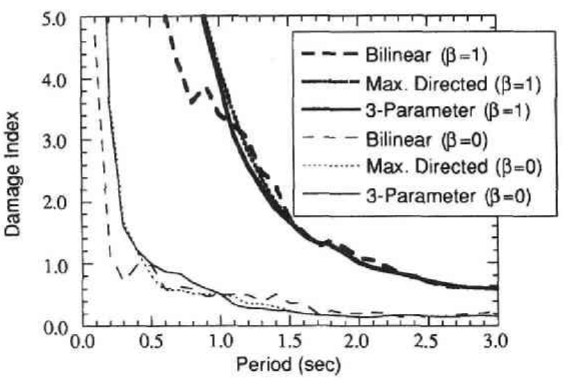

(c) Type 3 earthquake

Figure 2.16 Damage spectra for damage index.

3. Hybrid Experiments on Repaired RC Members Subjected to Earthquake Motion

3. 1 General Remarks

In this chapter, seismic behavior of repaired RC members is evaluated by hybrid experimental system.

A description of HYLSER (Hybrid Loading System of Earthquake Response) used to analyze repaired RC members under varying bending loads and constant axial force, and an analysis of the stiffness deterioration process for these members during earthquakes are given. A comparison of the energy-absorbing capability of the original and repaired members also is made.

3. 2 Hybrid Loading System of Earthquake Response (HYLSER)

3. 2. 1 Test Pieces

Eleven specimens were used, all having the dimensions 100×150×1900 mm (**Figure 3.1**) and a distance between supports of 1500 mm. Two specimens were doubly reinforced by deformed bars D16 (steel ratio p=3.1%), whereas the rest were doubly reinforced by D10 bars (p=1.1%). Concrete was confined by providing stirrups (6 mm in diameter) every 70 mm. Mechanical properties of the concrete and reinforcing bars are shown in **Tables 3.1** and **3.2**.

3. 2. 2 HYLSER System

A hybrid loading system of earthquake response, called HYLSER (**Figure 3.2** and **Photo 3.1**), was used to test specimens modeled as a single-degree-of-freedom system (**Figure 3.3**). A personal computer was used to solve the equation of motion in order to obtain the deformation at the next time step.

$$m\ddot{x}(t) + c\dot{x}(t) + F(x(t)) = -m\ddot{z}(t) \tag{3.1}$$

in which, m is the mass; $x(t)$ is the relative displacement at time t; c is the damping constant; $F(x(t))$ is the hysteretic restoring force at time t; $\ddot{z}$ is the ground acceleration; and a dot (.) indicates the time derivative.

Dividing Eq.(3.1) by m leads to

$$\ddot{x}(t)+\frac{c}{m}\dot{x}(t)+\frac{F(x(t))}{m}=-\ddot{z}(t) \tag{3.2}$$

Considering the initial condition, the third term of Eq.(3.2) becomes

$$\frac{F(x(0))}{m}=\omega^2 \tag{3.3}$$

in which, ω is the initial natural angular frequency. ω is calculated from

$$\omega=\frac{2\pi}{T'} \tag{3.4}$$

in which, T' is the initial natural period of the modeled structure (**Figure 3.3**). Using Eqs.(3.3) and (3.4), corresponding mass used in the experiments for a given structure is determined from

$$m=\frac{F(x(0))}{\omega^2}=\frac{F(x(0))}{4\pi^2}T'^2 \tag{3.5}$$

In addition, the second term of Eq.(3.2) can be calculated with known relation of

$$\frac{c}{m}=2h\omega \tag{3.6}$$

in which, h is the damping ratio. We assumed T'=0.5 sec and h=0.02 for all cases.

Both the linear acceleration and central differential methods were used for the step-by-step integration. In solving Eq.(3.1), $F(x(t))$ could be estimated directly from the on-line experiment. The actuator controls the midspan of the specimen using the computed displacement $x(t)$ sent through a DA (digital to analog) converter. In return, the computer gets the measured restoring force

$F(x(t))$ from the actuator received through an AD (analog to digital) converter. The flowchart for this on-line procedure is given in **Figure 3.4.**

The axial force-generating mechanism, in which a constant axial force is sustained by high-pressure oil built up by pressurizing air is shown in **Figure 3.5.** The three values of the axial load used; N = 4.0 tonf (39 kN), 2.0 tonf (20 kN) and 2.7 tonf (27 kN) which reflect values for real bridge piers based on Ref. 1).

The NS-components of the El Centro record (**Figure 3.6-a**) at the 1940 Imperial Valley earthquake and the Hachinohe record (**Figure 3.6-b**) at the 1968 Tokachi-Oki earthquake were the input earthquake excitations used. 30 seconds of these records were used. They were set to have the maximum values in the range of 100 to 300 gal (cm/sec^2). During the experiment the specimens were pseudo-dynamically tested over a period about 80 times longer in order to observe detail of the response. The schedule of loadings for the entire experiment is shown in **Table 3.3.**

3. 3 Repair Work

The three repair methods used are

(a) Type I: The Epoxy Resin Grouting Method:

Most of the test pieces were repaired by this method. First, mixed epoxy resin and sand were put on the heavily damaged parts, then, setting pipes were attached to the cracks (**Photo 3.2**), and sealed with epoxy bond (**Photo 3.3**). After that, epoxy resin was grouted into the cracks using the BICS (Balloon Injector for Concrete Structures) [2] at a low pressure of about 3 kgf/cm^2 (0.3 MPa) as shown in **Photo 3.4.** The BICS is diagrammed in **Figure 3.7.**

(b) Type II: The Reinforcing Bar Welding Method:

Two specimens, in which the reinforcing bars had buckled, were repaired by this method. First the axial force was unloaded, and the concrete around the damaged bars removed. The same type of steel as in the damaged bars (two times the length of the buckled segment) was welded to the reinforcing bar (**Photo 3.5**), after which the segment was repaired with a mixture of epoxy resin and sand. Epoxy resin was grouted into the cracks by the BICS device used for Type I repair.

(c) Type III: The Steel Plate Covering Method:

Three specimens were repaired by this method. The damaged segment (**Figure 3.8-a**) was filled with mixture of epoxy resin and sand (**Figure 3.8-b**), after which steel plates were bonded to the damaged part with epoxy resin (**Figure 3.8-c**). Epoxy resin then was grouted into the cracks by the technique used for Type I (**Photo 3.6**).

The steel plates used were the same length as the damaged segment of concrete for specimen 5, but twice the length of the damaged segment for specimens 1 and 10. The thickness of the steel plate used was computed as having the same moment of inertia as the original reinforcing bars; that is, the moment of inertia of the specimen was restored to the original value by the steel plates used, assuming that the damaged reinforcing bars were totally incapacitated.

This method is much easier to use than the Type II method in that no unloading of the axial force nor removal of the concrete around the damaged part is necessary. Nevertheless, careful attention must be paid to how the steel plates are bonded to the damaged segment.

3. 4 Experimental Results

3. 4. 1 Original Specimens

Data for the original specimens were taken from a previous study [3]. For example, the cracks of No. 4 specimen after the loading test is shown in **Photo 3.7**. The main results for the original specimens were that

(1) a high axial force resulted in a higher yielding level and lower ductility of the specimens.

(2) the stiffness of the specimens with higher reinforcement ratios (specimens 10 and 11) was 50% more than that of the others, but the yielding loads were 100% more.

(3) when a high axial force was acting, a specimen failed with just one large plastic deformation.

3. 4. 2 Type I Repair (The Epoxy Resin Grouting Method)

The hysteretic load-deformation responses shown in **Figure 3.9** are for three similar specimens subjected to different input levels of acceleration. Note that the original maximum values for the restoring force were reached even after repair. In tests without axial force [3], damage took place not to the repaired segment but adjacent to it. In tests made under axial force, cracking and crushing of the concrete appeared midspan in the test pieces. This is because damage to the reinforcing bars at the center was severe.

For a maximum acceleration of 300 gal (**Figure 3.9-c**), the maximum restoring force was almost the same as before repairs were made; but, reduced ductility caused early crushing of the repaired specimen (**Photos 3.8** and **3.9**). For specimens in which the reinforcing bars are badly buckled, repair by this method does not restore the original high strength under dynamic loads; therefore, Type I repair should be used with caution.

3. 4. 3 Type II Repair (The Reinforcing Bar Welding Method)

The hysteretic responses before and after repair of specimens are shown in **Figure 3.10**. After repair, the specimen was stronger in one direction than in the other. This was because the two repaired reinforcing bars were located on one side of the specimen.

3. 4. 4 Second Loading without Repair

In a previous study [3], specimens with minor cracks were adequately repaired with epoxy resin. In the study reported here, strong acceleration also was applied to unrepaired specimens to obtain heavily damaged specimens and to observe the destruction process. All the test pieces were damaged at their midspans. Two of them (specimens 1 and 5) collapsed, but the specimen with the high reinforcement ratio (specimen 10) was not completely crushed. After the first large deformation, however, the specimen simply folded and never again straightened.

Large deformations were present after only a few cycles (**Figures 3.11-b, 3.12-b**). This means that all the specimens were severely damaged after the first loading tests. As the yielding accelerations of the reinforcing bars were

estimated to be 90-120 gal [3], these bars might already have yielded after the first loading tests.

3. 4. 5 Type III Repair (The Steel Plate Covering Method)

A comparison of **Figures 3.11-a** and **3.11-c**, and of **Figures 3.12-a** and **3.12-c**, shows an increase in the restoring-force capacities of the repaired specimens. Two causes can be cited: In calculating the thickness of the steel plate, the old reinforcing bars were assumed to be totally ineffective; whereas, in reality, these may have retained some resistances. Also, as the location of the plastic hinge moved from the center to the edge of the steel plate, a larger force was needed to bend the specimens.

After the third loading, strong accelerations again was applied to the repaired specimens (Type III), without any further repair, to observe their behavior in an extreme state. The hysteretic responses shown in **Figures 3.11-d** and **3.12-d**, specimen 5 whose steel plate was as long as its damaged part, was severely mangled (**Photo 3.10**), the concrete being crushed at the edge of the steel plate under compression. In contrast, the other specimens, whose steel plates were twice the length of their damaged parts, did not suffer great damage. The steel plates came away from these specimens at midlength, and many cracks developed in the concrete in the vicinity of their midspans. The hysteretic responses for these specimens also were stable; accordingly, the length of the steel plate to be used in repairs must be carefully considered. In addition, further study is needed to determine the adequate thickness of the steel plates.

3. 4. 6 Cross Sections of the Repaired Specimen

One of the specimens was then cut into several pieces using the diamond cutter (**Photo 3.11**). **Figure 3.13** shows the places at which the specimen was cut, and **Figure 3.14** shows the cross sectional views of the specimen. The solid lines are cracks of the first loading test filled with epoxy resin, the dotted lines are new cracks of the second loading test, and the shadowed areas are epoxy mortar used to repair the broken unconfirmed segment. The loading direction was vertical in this figure. The following things were observed:

(1) Epoxy resin was filled even in the cracks of 0.1 mm wide. Accordingly, it was verified that repair work has been successfully done.

(2) The cracks of the second loading test were much less than those of the first

loading test. And they did not appear in the same region of the first loading, nor the unconfined concrete did not fall as before. These were caused by the higher tensile strength of the repaired specimen with the grouted epoxy resin.

(3) The cracks of the second loading were totally wider than those of the first loading. As the cracks were less than before, deformation might be concentrated to those cracks.

3. 5 The Stiffness Deterioration Process

3. 5. 1 Suitable Index for Stiffness Deterioration

There are many definitions of equivalent stiffness. For example, the slope between the origin and the point of maximum restoring force is the well known definition for the equivalent stiffness. But this equivalent stiffness underestimates the stiffness when the center of the hysteretic response curves goes away from the origin [4]. For this reason, we looked for other definitions of stiffness to obtain a parameter for describing the stiffness deteriorating process. We considered two definitions as shown graphically in **Figure 3.15**.

The "equivalent stiffness", K_{eq}, is defined as the slope between the midpoint of two zero points of restoring forces and the point of maximum restoring force in a half cycle. Taking into account the half cycle of the hysteretic responses, from time t_1 to t_4, K_{eq} can be written

$$K_{eq} = \frac{F(x(t_2))}{x(t_2) - \dfrac{x(t_1) + x(t_4)}{2}} \tag{3.7}$$

in which, t_1 is the time when the response curve crosses the x-axis, $F(x(t_1))=0$; t_2 the time when the restoring force has its maximum value; and t_4 the time when the restoring force again is zero, $F(x(t_4))=0$. In contrast, the "unloading stiffness", K_u, is defined as the slope between the starting and end points of the unloading process.

$$K_u = \frac{F(x(t_3))}{x(t_3) - x(t_4)} \tag{3.8}$$

in which, t_3 is the time when unloading begins. These two stiffnesses were compared for all the tested specimens in order to obtain an adequate description of the stiffness deterioration process.

The stiffness deterioration process for specimen 6 in terms of the two defined stiffnesses is shown in **Figure 3.16**. At about 2 seconds, both stiffnesses begin to deteriorate, after which the equivalent stiffness, K_{eq}, increases somewhat, whereas the unloading stiffness, K_u, remains almost constant. A similar comparison (**Figure 3.17**) was made for specimen 5, on which a second loading was imposed without repairing the damage sustained during the initial loading. About 2 seconds into the second loading test (32 seconds after initiation of the test), the specimen collapsed. Interestingly, at the start of the 2nd loading, K_{eq} regained its initial undeteriorated stiffness value. Also K_{eq} became exceedingly small when deformation was large, resulting in an abrupt drop in the computed K_{eq} value. For these two reasons, the stiffness deterioration process cannot be properly described by equivalent stiffness (K_{eq}).

Although the unloading stiffness (K_u) also varied, its trend was as expected for a degrading system. The K_u stiffness therefore is considered an adequate index of the stiffness deterioration process.

3. 5. 2 Stiffness Deterioration Process in Repaired Specimens

Three time histories of the K_u unloading stiffness are shown in **Figure 3.18**. K_u began to decrease (initially markedly) when the specimen was undergoing severe deformation. This was about 2 seconds after the beginning of loading when the El Centro record was the input used (**Figures 3.18-b, c**), and after about 8 seconds for the Hachinohe record (**Figure 3.18-a**). K_u took almost constant value after the maximum response of the specimen. Both processes would have been similar if the input earthquake motions had been the same. In general, we conclude that the characteristics of the input earthquake are the dominant factors in stiffness deterioration; the characteristics of the specimens have little effect on it.

The final deterioration ratios shown in **Table 3.4** are defined as the ratio of the K_u unloading stiffness at the end of the test to the K_u at the beginning; smaller values represent greater deterioration. For all the specimens, except No. 1, the deterioration ratios of the repaired specimens are larger than those of the

unrepaired specimens.

The initial stiffnesses of the specimens repaired by the epoxy resin grouting method (Type I) are about 80% those of the unrepaired originals. For the originals, the deterioration ratio is proportional to the strength of the input acceleration; whereas, there is no correlation for the repaired specimens (see **Figures 3.16-a**, **3.18-b** and **Table 3.4**). Possibly, the difference in the amount of epoxy resin used in relation to the degree of damage may have produced the variations in the characteristics of the repaired test pieces.

The deterioration ratios of specimens repaired by the reinforcing bar welding method (Type II) and the steel plate covering method (Type III) are larger than the original ratios, particularly for Type II specimens which are much larger (**Figure 3.18-c** and **Table 3.4**). During the experiment, we observed that deformations of repaired specimens were smaller than those of the unrepaired originals. The initial stiffnesses of specimens repaired by the Types II and III methods are about 100 to 110% those of the unrepaired specimens.

3. 6 Energy Dissipation

Energy-absorbing capabilities should be taken account when investigating damage to specimens. Energy partitioning is calculated from the following equation derived from the equation of motion, Eq.(3.1);

$$m\int_0^t \ddot{x}\dot{x}dt + c\int_0^t \dot{x}^2 dt + \int_{x(0)}^{x(t)} F(x)dx = -m\int_0^t \ddot{z}\dot{x}dt \qquad (3.9)$$

The first term on the left side of Eq.(3.9) represents the kinetic energy, W_K, of a specimen at time t; the second the absorbed viscous damping energy, W_C, and the third the absorbed hysteretic energy, W_H. The right side of Eq.(3.9) represents the energy imparted, E, by earthquake motion. The absorbed hysteretic energy, W_H, is a major factor in the structural damage produced by cyclic loadings. It is calculated as being the area enclosed by the hysteretic response curves. Each term of Eq.(3.9) per a half cycle of the hysteresis responses is calculated step by step for all the tested specimens.

The difference between the hysteretic energy dissipation of the original specimens and that of the repaired specimens can be estimated. First, the ratios of W_H and W_C during earthquake response are compared. There is little

difference between the energy participation of the original specimens and that of the repaired material, except when the input acceleration is not strong (**Figure 3.19-a**). The ratio of the damping energy, W_C, for the repaired specimen is considerably larger and the participation of the hysteretic energy, W_H, less than that of the original. This is because the elastic range of the RC members was wider after repair. When the input is low, specimens behave like elastic members.

As the input earthquake becomes stronger, the difference between the energy participation ratio of the repaired members and that of the originals decreases, (**Figures 3.19-b** and **c**). For instance, there is no difference when the input acceleration was the El Centro record with maximum values set at 200 and 250 gal. This means that the same maximum deformation is to be expected from the same degree of earthquake motion even after repair.

The ratio of the hysteretic energy (W_{HT}) dissipated during one experiment to the total input energy (E_T) is plotted in **Figure 3.20**. The broken line shows $W_{HT}=E_T$. The solid line is derived from the least square fit of a straight line:

$$W_{HT} = aE_T - b \tag{3.10}$$

in which, a=0.68; b=3.4. The ratio of W_{HT} to E_T is derived from Eq.(3.10) when W_{HT}, $E_T \geq 0$:

$$\frac{W_{HT}}{E_T} = \begin{cases} 0 & (0 \leq E_T \leq 5) \\ a - \dfrac{b}{E_T} & (E_T > 5) \end{cases} \tag{3.11}$$

The total absorbed hysteretic energy is in proportion to the total input energy. For a low input excitation of $E_T \leq 5$ tonf·cm (0.5 kN·m), the total E_T input energy changes to W_C and W_K; i.e., $W_{HT}=0$. As the input earthquake becomes stronger, the contribution of W_H increases, and for a large input excitation, the ratio of W_{HT} to E_T is almost constant. Let E_T in Eq.(3.11) be infinity, then the ratio of W_{HT} to E_T becomes a=0.68.

Figure 3.20 shows that the ratio of W_{HT} to E_T is not affected by any difference in the specimens or the input acceleration, except for a low range of E_T as discussed before (**Figure 3.19**). Because a constant damping ratio of h = 0.02 was assumed for all cases, no effect of the damping ratio need be considered.

3.7 Seismic Risk of Unrepaired Damaged Members

The damaged members could be left unrepaired after an earthquake if damage is not so serious. The response, however, for the next earthquake is quite different compared with a new specimen. This section discusses effect of the unrepaired damge to the future seismic response using the damage index which is shown in Chapter 2.

The first term of the damage index shown in Eq. (2.1) represents damage suffered by the maximum deflection, and the second term represents damage due to the energy absorbing procedure discussed in the previous section. The damage index takes values between 0 and 1, where 1 expresses total collapse.

Figure 3.21 shows the damage indices time histories of the specimens. To see effect of unrepaired damage for the future response, specimens 1 and 7 were compaired in **Figure 3.21-a**; an input acceleration for the second loading of specimen 1 and for the first loading of specimen 7 were the same. For the same reason, **Figure 3.21-b** compares specimens 2 and 6. The damage indices, D, became larger than 1 in all cases of **Figure 3.21**; it signifies collapse of the specimens which corresponds to the experimental results.

D of specimen 6 became 1 at 13 seconds from the beginning of the experiment (a broken line in **Figure 3.21-b**), and it increased little to the last value of 1.1. D of specimen 2, to the contrary, took 1 at only 2 seconds from the beginning of the second loading test, which is shown in a solid line of **Figure 3.21-b**.

For specimens 1 and 7 shown in **Figure 3.21-a**, their damage indices reached1 simultaneously, but they behave quite different after that. D of specimen 1 increased rapidly and the specimen collaplsed while D of specimen 7 stays 1.7. The damage index, D, showed effect of unrepaired damage to the future seismic behavior numerically.

The values of the first term and the second term of the damage index are also plotted in **Figure 3.21**. The first term increases when the input acceleration becomes large; at 2 second for the El Centro record and at 10 second for the Hachinohe record. After that, it keeps the same value during a response. The second term keeps on increasing throughtout a response. As the input earthquake motions were strong and short, the effect of the first term to D was high, which shows damage resulting from the large deflection was major.

3. 7 Conclusions

The stiffness-deteriorating and energy-absorbing processes of repaired RC members were studied, with the main results being that as follows.

(1) Specimens repaired by the epoxy resin grouting method showed similar dynamic behavior if their reinforcing bars had not buckled.

(2) Specimens repaired by the reinforcing bar welding method showed asymmetric hysteretic load-deformation responses when only one side had been repaired.

(3) Specimens repaired by the steel plate covering method could bear more load than the unrepaired originals when the thickness of the steel plates had been selected as having the same moment of inertia as the original reinforcing bars.

(4) Stiffness deterioration can be estimated from the unloading stiffness, K_u.

(5) The characteristics of the input accelerogram, not those of the specimens, are the major factors operating in stiffness deterioration.

(6) Stiffness deterioration in repaired specimens depends on the method of repair. The process in a specimen repaired by the epoxy resin grouting method is similar to that of the unrepaired original; whereas, the stiffness of specimens repaired by the reinforcing bar welding and steel plate covering methods deteriorated only 50% in comparison to values for unrepaired specimens.

(7) The ratios of the initial stiffnesses of the repaired specimens to those of the unrepaired originals were about 80% for the epoxy resin grouting method and about 100-110% for the reinforcing bar welding and steel plate covering methods.

(8) The ratio of the hysteretic energy dissipated during one loading to the total input energy was an almost constant 70% when the constant damping ratio was used and the input earthquake was strong enough to produce inelastic deformation.

(9) The damage indices time histories verified that the seismic risk of

unrepaired specimens with cracks were much higher than new specimens.

References of Chapter 3

1) Hanshin Highway Public Corporation, "Deformation of RC bridge piers during earthquake motion", *Research Data for the Technical Committee of Seismic Design*, No. 8-3, 1981 (in Japanese).
2) Sho-Bond Construction Co., Ltd., "The BICS technique", *Sho-Bond Catalog*, 1981 (in Japanese).
3) Iemura, H., "Hybrid experiments on earthquake failure criteria of reinforced concrete structures", *Proc. of the 8th World Conference on Earthquake Engineering*, U.S.A., Vol. VI, pp. 103-110, 1984.
4) Yamada, Y. and Iemura, H., "Inelastic aseismic design of reinforced concrete structures", *The 12th Congress of International Association for Bridge and Structural Engineering*, Vancouver, BC, Canada, pp. 1198-1199, 1984.

Table 3.1 Strength of concrete.

Compression	$300 kgf / cm^2$	$(29 MPa)$
Tension	$30 kgf / cm^2$	$(2.9 MPa)$
Young's Modulus	$1.4 \times 10^5 kgf / cm^2$	$(14 GPa)$

Table 3.2 Mechanical properties of the reinforcing bars.

	D10	D16
Nominal Diameter	$0.953 cm$	$1.590 cm$
Section Area	$0.713 cm^2$	$1.986 cm^2$
Yield Stress	$3800 kgf / cm^2$	$(373 MPa)$
Young's Modulus	$2.1 \times 10^6 kgf / cm^2$	$(205 GPa)$

Table 3.3 Sequences of loading. Type I: epoxy resin grouting method; Type II: reinforcing bar welding method; Type III: steel plate covering method; E, El Centro NS (The 1940 Imperial Valley Earthquake, U.S.A.); H, Hachinohe NS (The 1968 Tokachi-oki Earthquake, Japan); digits 100-300, maximum acceleration in gal=cm/sec^2.

No.	steel ratio p	axial force N	initial loading	second loading	loading after repair			ultimate loading
					Type I	Type II	Type III	
1	1.1%	4.0 t	100 H	250 E			100 H	250 E
2			150 H	200 E	150 H			
3			250 H		250 H			
4			300 H		300 H			
5			150 E	300 E			150 E	300 E
6			200 E		200 E			
7			250 E		250 E			
8			300 E		300 E			
9		2.0 t	150 E	300 E		150 E		
10	3.1%	2.7 t	150 E	250 E			150 E	300 E
11			300 E			300 E		

Table 3.4 Deterioration ratio of stiffness. Type I: epoxy resin grouting method; Type II: reinforcing bar welding method; Type III: steel plate covering method; E, El Centro NS (The 1940 Imperial Valley Earthquake, U.S.A.); H, Hachinohe NS (The 1968 Tokachi-oki Earthquake, Japan); digits 100-300, maximum acceleration in gal=cm/sec^2.

No.	steel ratio p	axial force N	initial loading	second loading	loading after repair			ultimate loading
					Type I	Type II	Type III	
1	1.1%	4.0 t	0.73 →	0.54			→ 0.67	→ 0.50
2			0.58 →	0.48	→ 0.83			
3			0.46		→ 0.55			
4			0.46		→ 0.58			
5			0.56 →	0.31			→ 0.59	→ 0.59
6			0.46		→ 0.48			
7			0.40		→ 0.68			
8			0.35		→ 0.40			
9		2.0 t	0.46 →	0.32		→ 0.85		
10	3.1%	2.7 t	0.80 →	0.50			→ 0.85	→ 0.36
11			0.30			→ 0.59		

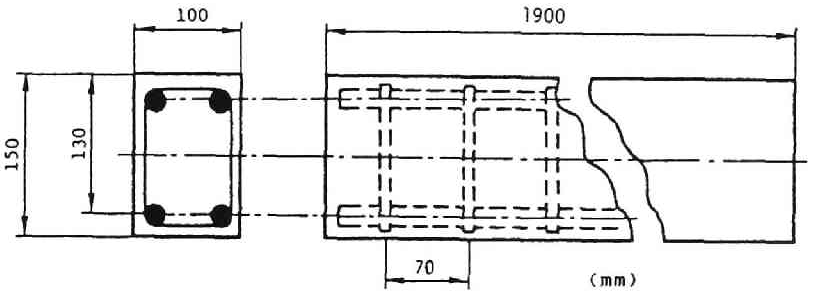

Figure 3.1 Specimen dimensions.

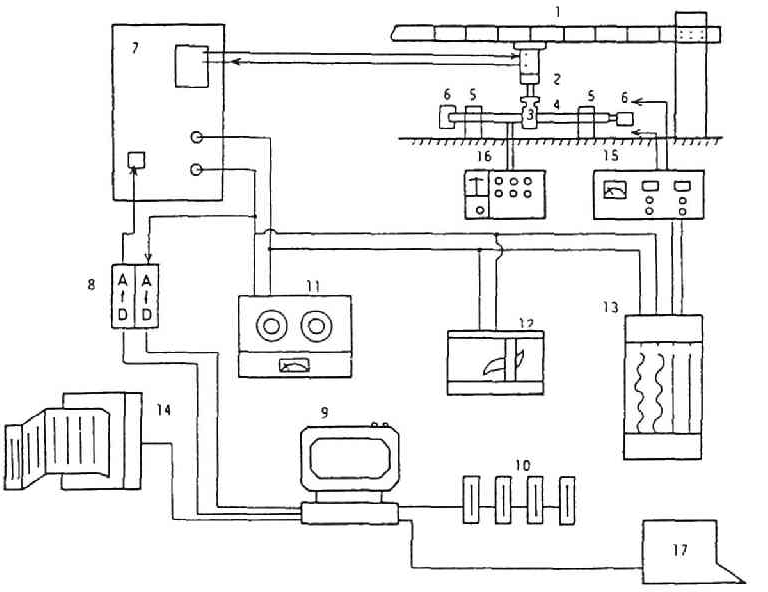

1. Frame
2. Actuator
3. Loading Frame
4. Test Piece
5. Simple Support
6. Axial Force System
7. Central Controller
8. AD-DA Converter
9. Microcomputer
10. Floppy Disk
11. Data Recorder
12. X-Y Recorder
13. Pen Recorder
14. Line Printer
15. Dynamic Strain Gage
16. Strain Gage (Static)
17. Kyoto Univ. Data Processing Center

Figure 3.2 HYLSER (Hybrid Loading System of Earthquake Response) diagram.

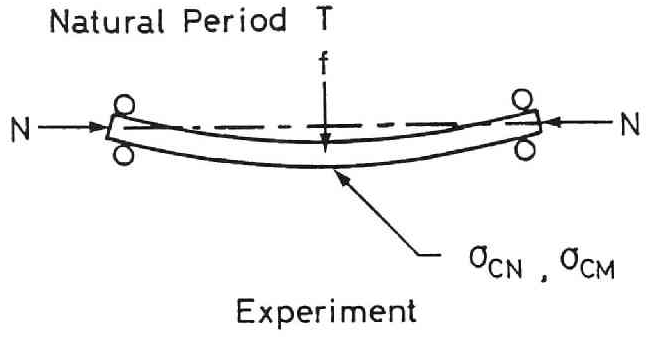

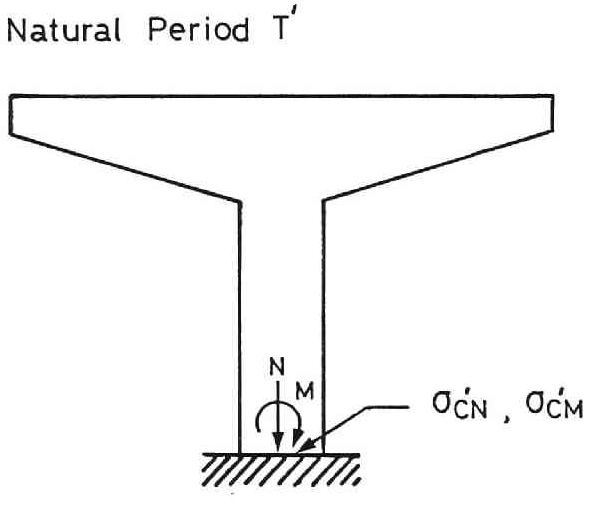

$$T = T'$$

$$\sigma_{CN} = \sigma'_{CN}$$

$$\sigma_{CN} / \sigma_{CM} = \sigma'_{CN} / \sigma'_{CM}$$

Figure 3.3 Bridge pier and its experimental model.

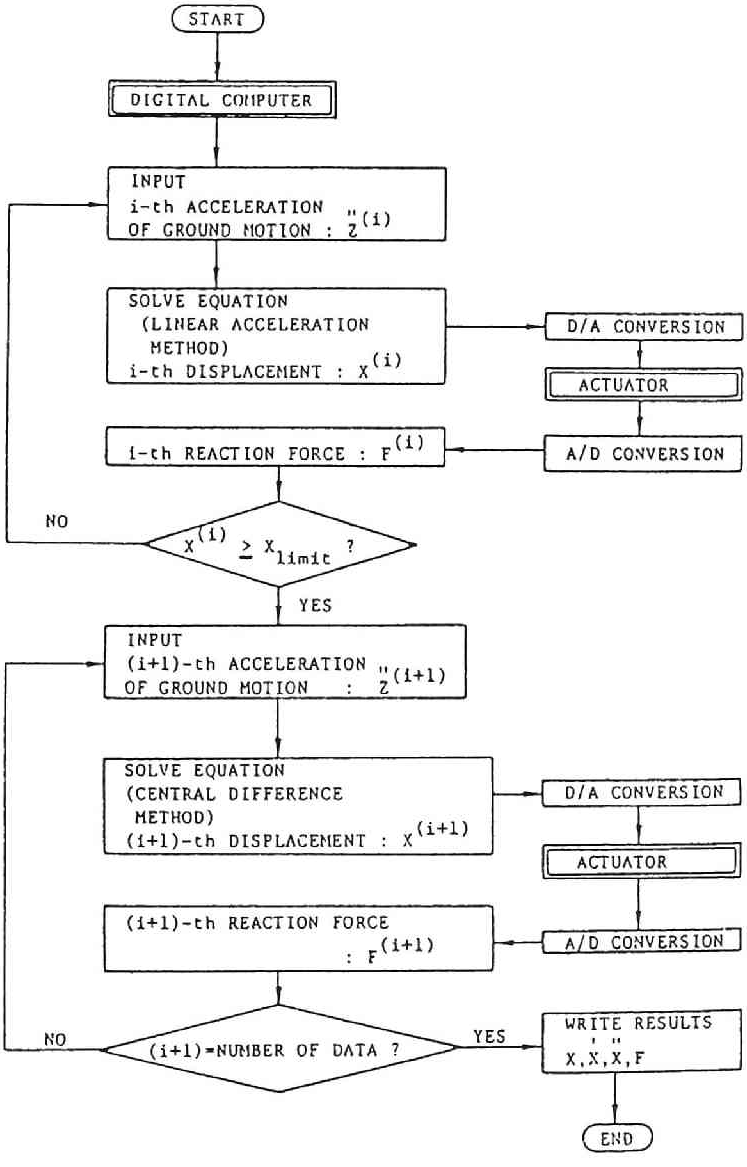

Figure 3.4 HYLSER flow chart.

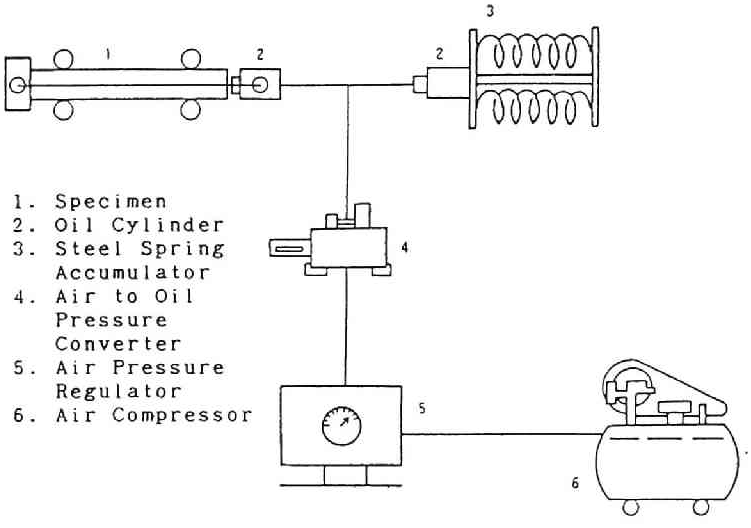

Figure 3.5 Mechanism for generating axial force.

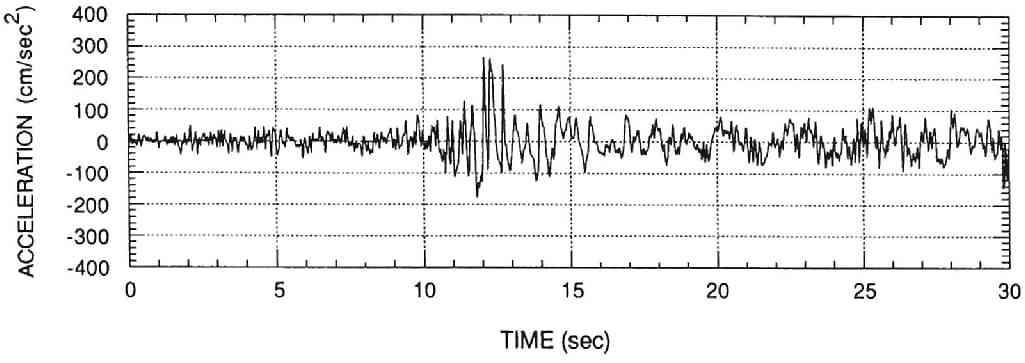

(a) The NS component of the El Centro record.
(The 1940 Imperial Valley Earthquake, U.S.A.)

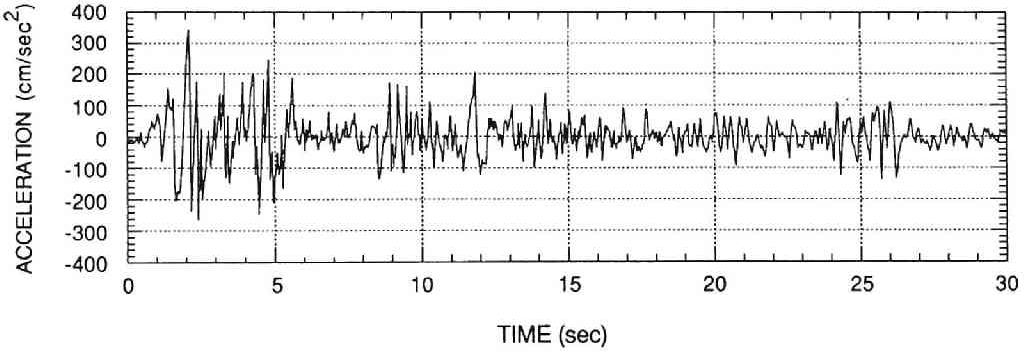

(b) The NS component of the Hachinohe record.
(The 1968 Tokachi-oki Earthquake, Japan)

Figure 3.6 Earthquake records used in the experiments.

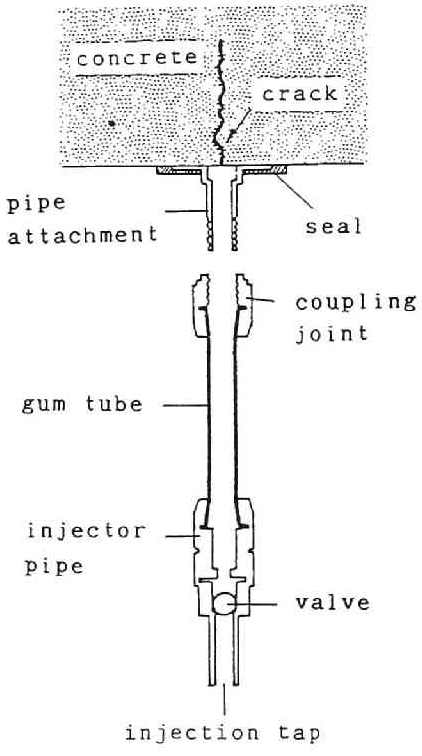

Figure 3.7 BICS (Balloon Injector for Concrete Structures) [2)]

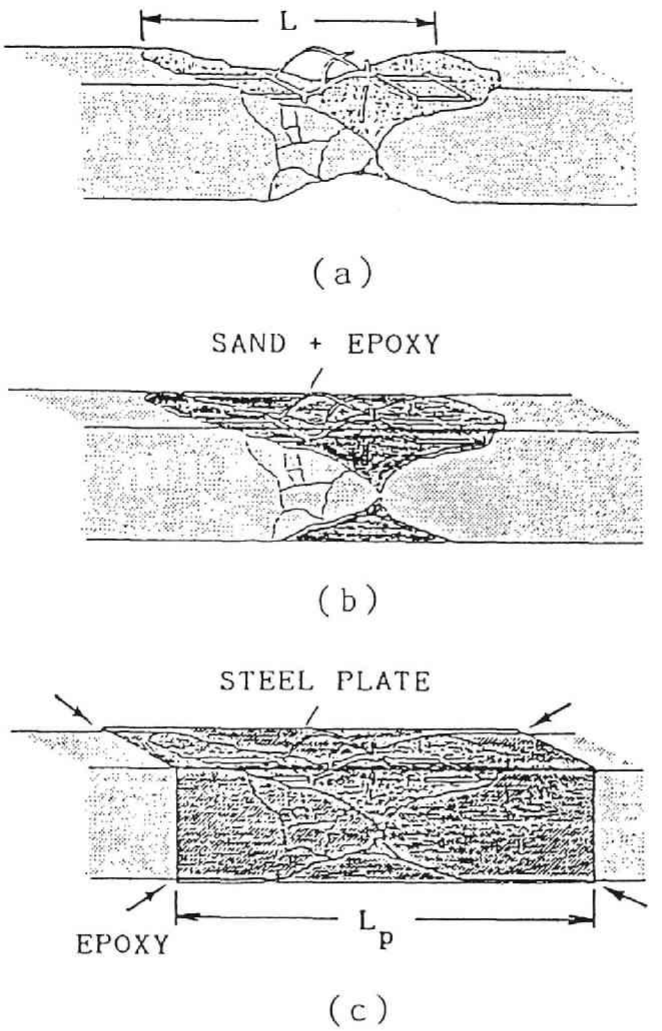

Figure 3.8 Steel plate covering method.
(a) Damaged segment. (L: length of damaged segment)
(b) Fill with sand and epoxy resin mixture.
(c) Cap with a steel plate and bond with epoxy resin. (L_p: length of the steel plate) L_p=L for specimen 5. L_p=2L for specimens 1 and 10.

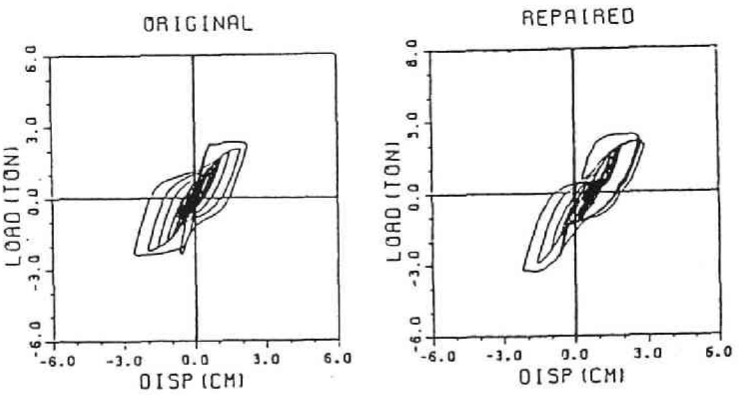

(a) Specimen 6 (El Centro, 200 gal)

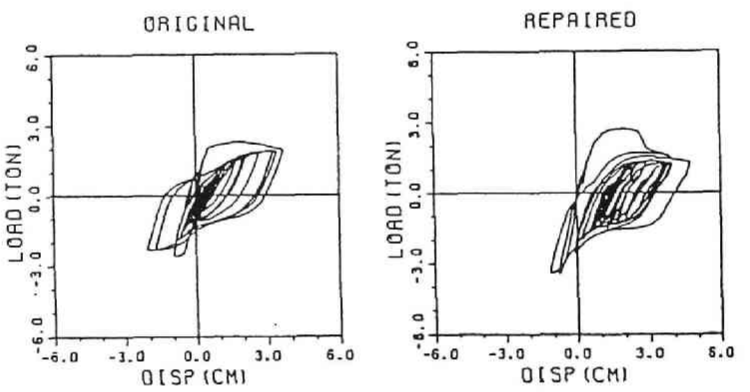

(b) Specimen 7 (El Centro, 250 gal)

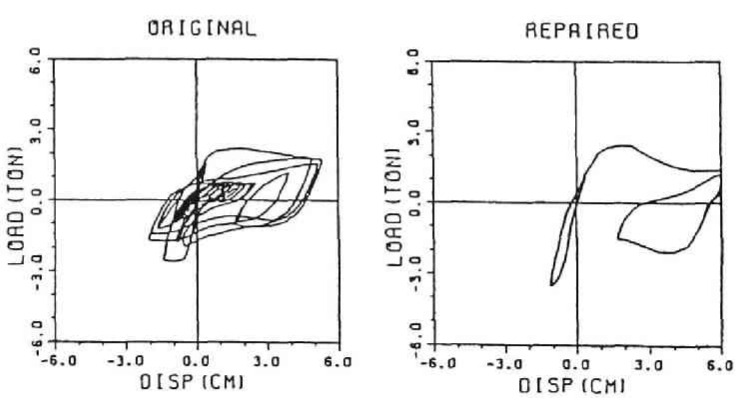

(c) Specimen 8 (El Centro, 300 gal)

Figure 3.9 Hysteretic responses for the original and repaired specimens. (Repaired by the epoxy resin grouting method; Type I)

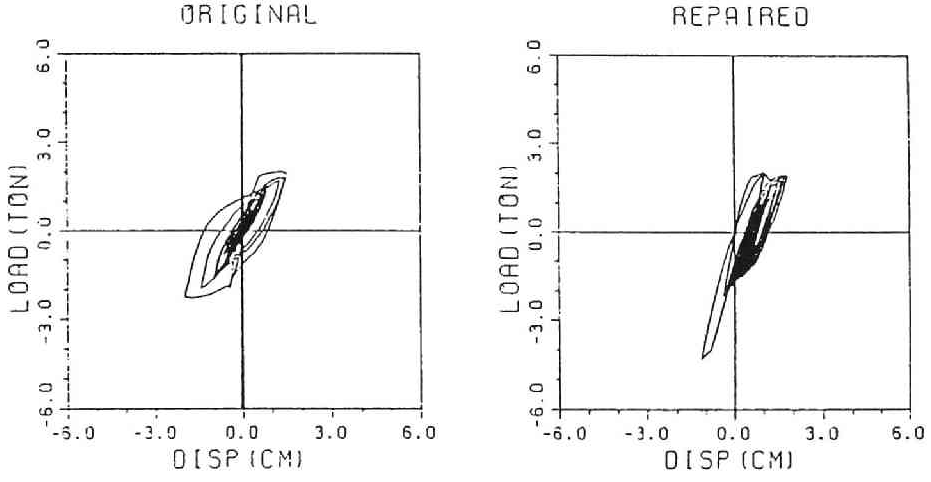

Figure 3.10 Hysteretic responses for the original and repaired specimen 9. (Repaired by the reinforcing bar welding method; Type II)

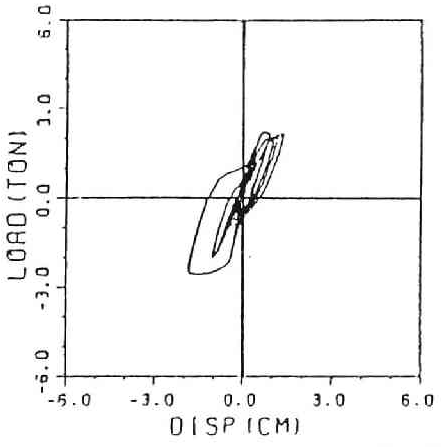

(a) Initial loading (max. 150gal).

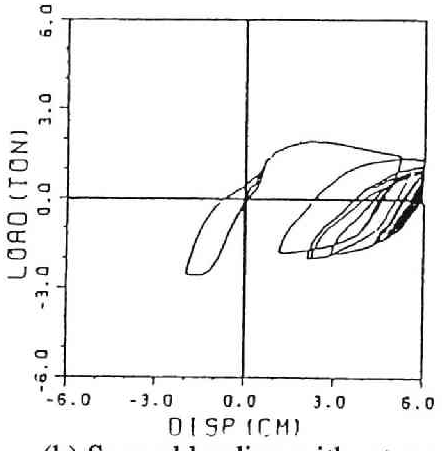

(b) Second loading without repair (max. 300gal).

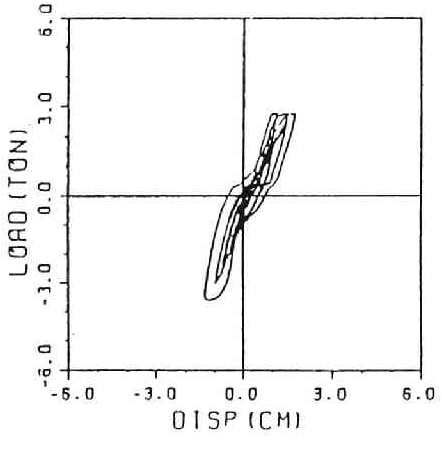

(c) Loading after repair (max. 150gal).

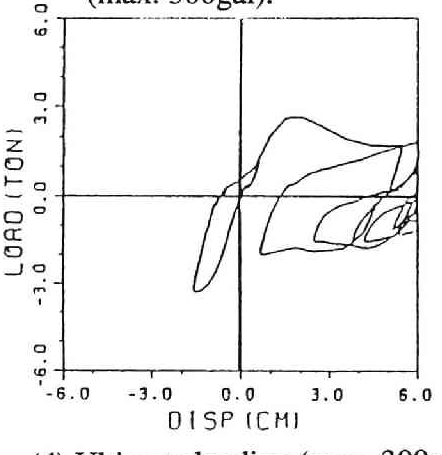

(d) Ultimate loading (max. 300gal).

Figure 3.11 Hysteretic responses for the original and repaired specimen 5. (Repaired by the steel plate covering method; Type III)

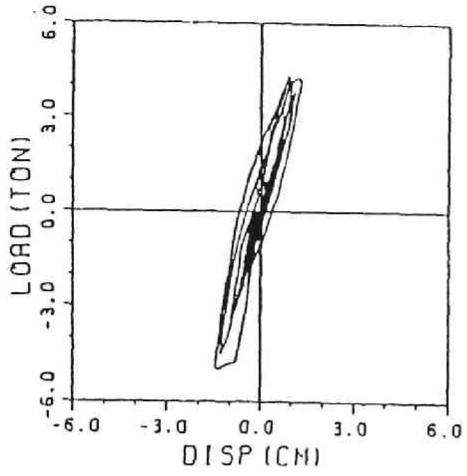

(a) Initial loading (max. 150gal).

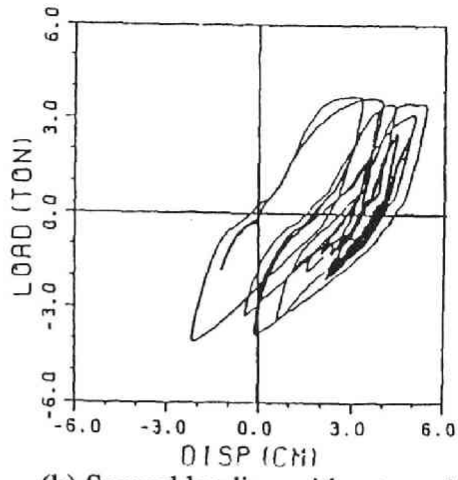

(b) Second loading without repair (max. 250gal).

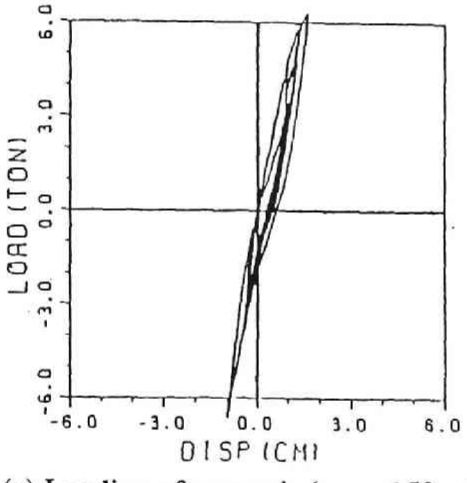

(c) Loading after repair (max. 150gal).

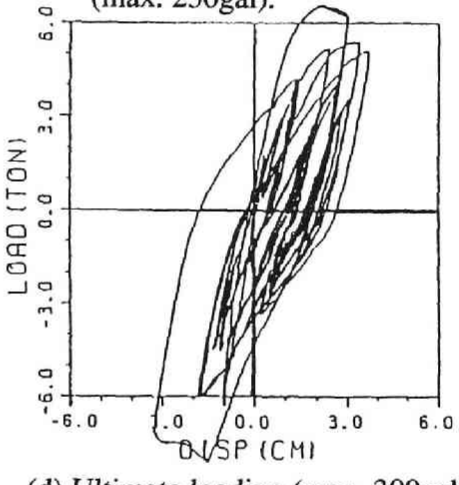

(d) Ultimate loading (max. 300gal).

Figure 3.12 Hysteretic responses for the original and repaired specimen 10. (Repaired by the steel plate covering method; Type III)

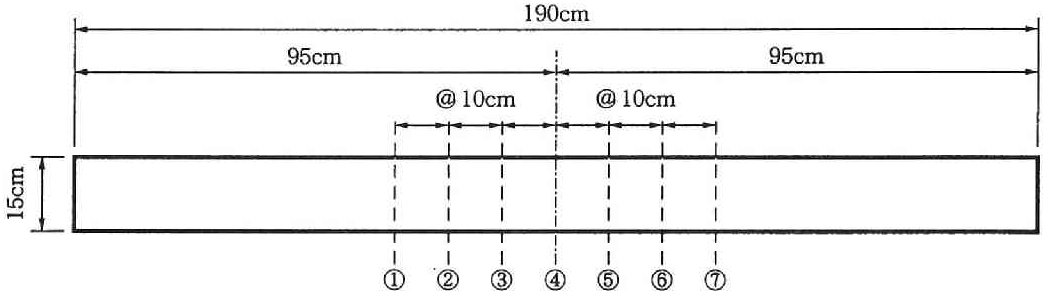

Figure 3.13 Section numbers at which the specimen was cut.

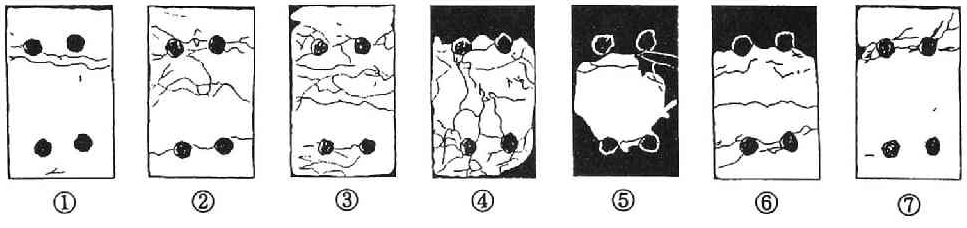

Figure 3.14 Cross sectional views of the specimen.

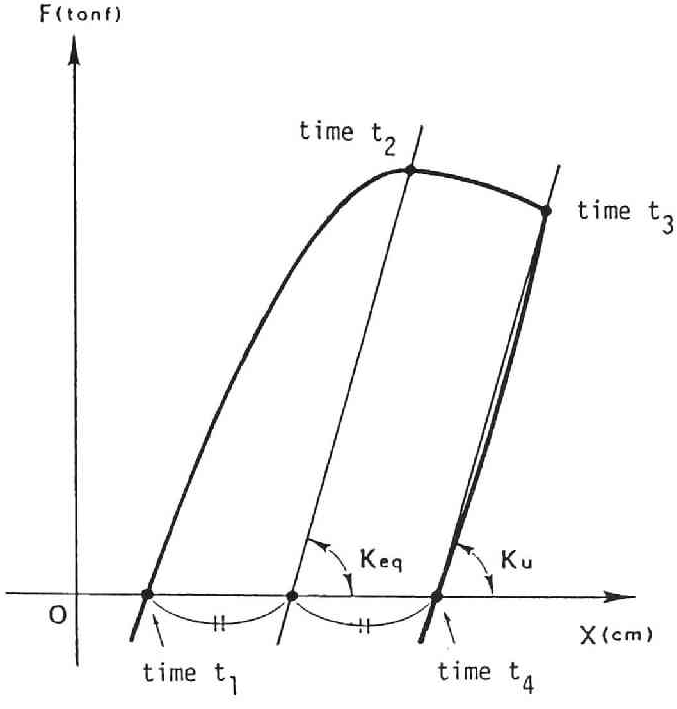

Figure 3.15 The unloading stiffness, K_u, and the equivalent stiffness, K_{eq}. The hysteretic response curve crosses the x-axis at time t_1 and has its maximum value at time t_2. The unloading process begins at time t_3. The restoring force again becomes zero at time t_4.

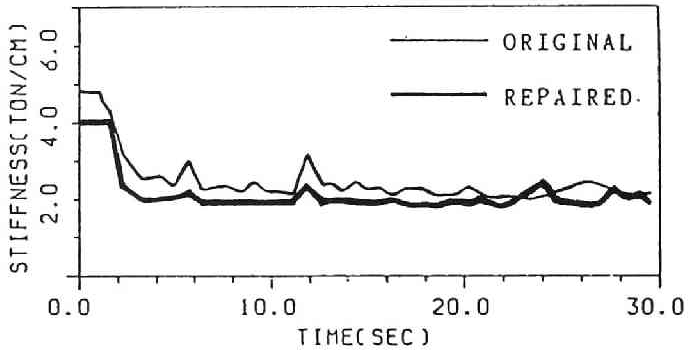

(a) K_u

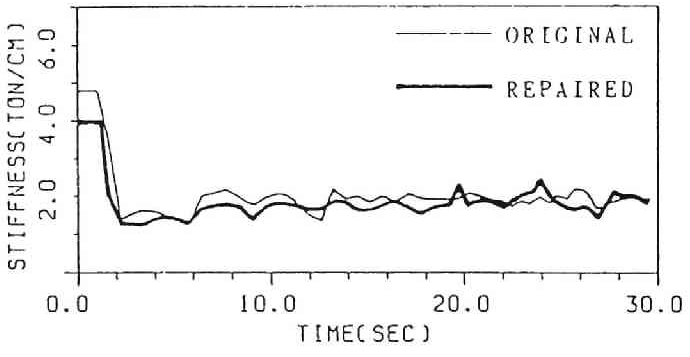

(b) K_{eq}

Figure 3.16 Stiffness-time histories of the original and repaired specimen 6. (El Centro, 200 gal. Repaired by the epoxy resin grouting method; Type I)

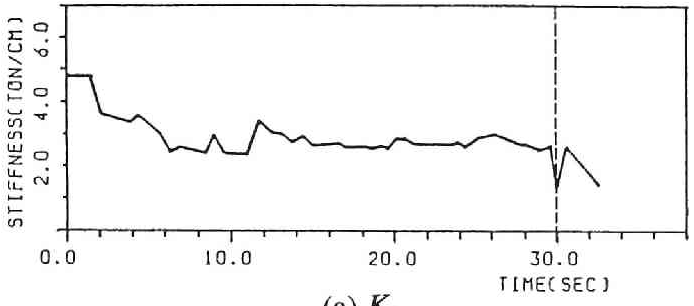

(a) K_u

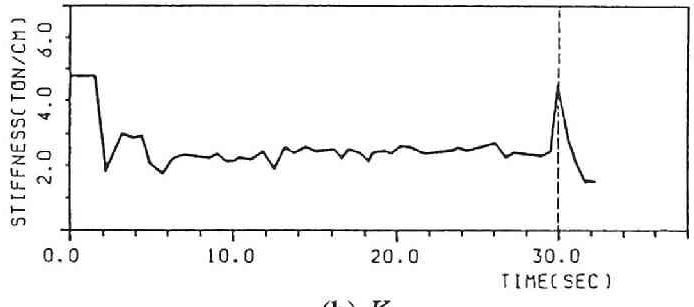

(b) K_{eq}

Figure 3.17 Stiffness-time histories of specimen 5.
(Initial loading, 0-30 sec: El Centro, 150 gal. Second loading, 30-32 sec: El Centro, 300 gal).

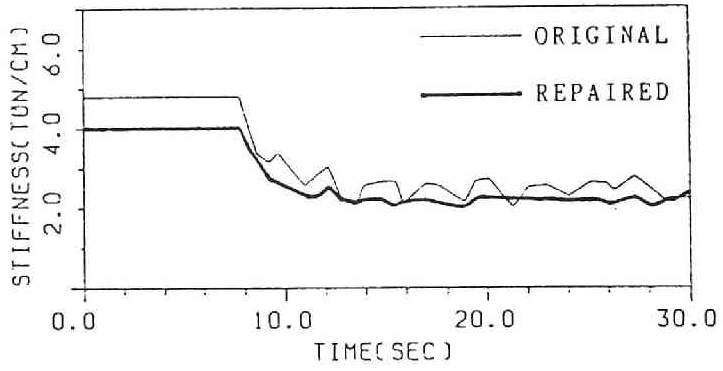

(a) Specimen 4 (Hachinohe, 300 gal. Repaired with the epoxy resin grouting method; Type I)

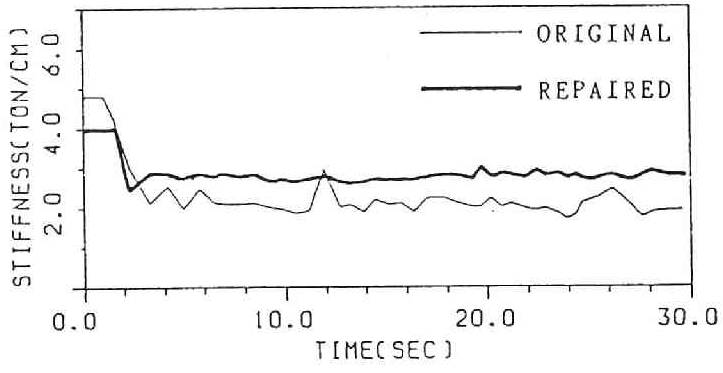

(b) Specimen 7 (El Centro, 250 gal. Repaired with the epoxy resin grouting method; Type I)

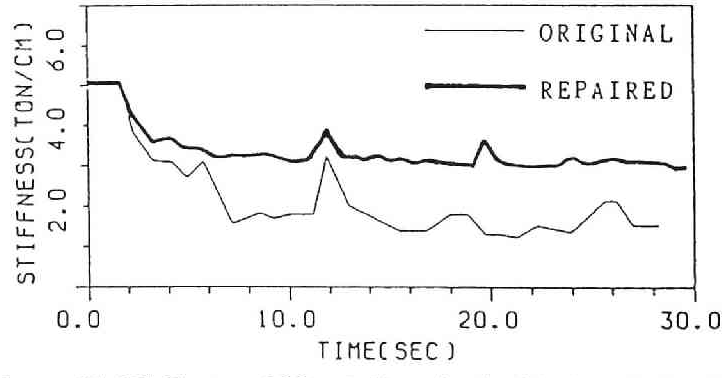

(c) Specimen 11 (El Centro, 300 gal. Repaired with the reinforcing bar welding method; Type II)

Figure 3.18 Examples of stiffness-time histories.

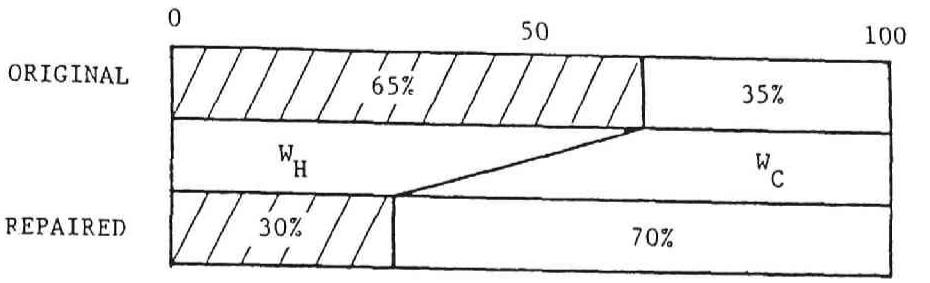

(a) Specimen 2 (Hachinohe, 150 gal).

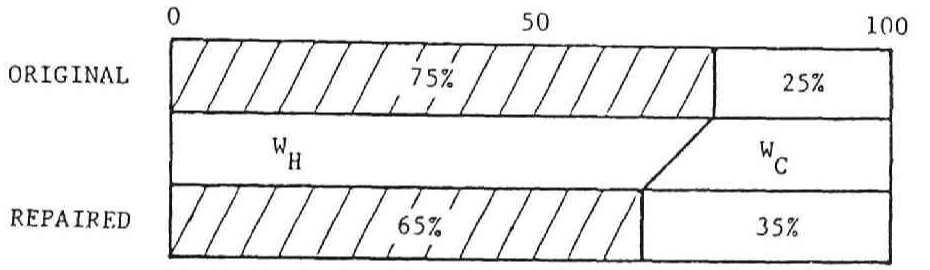

(b) Specimen 4 (Hachinohe, 300 gal).

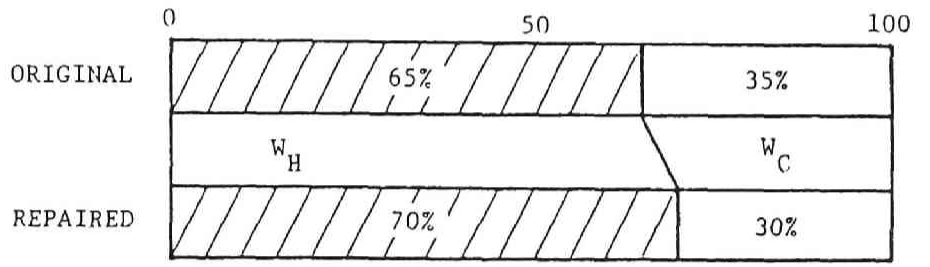

(c) Specimen 7 (El Centro, 250 gal).

Figure 3.19 Energy participation ratios (W_H: hysteretic energy. W_C: damping energy).

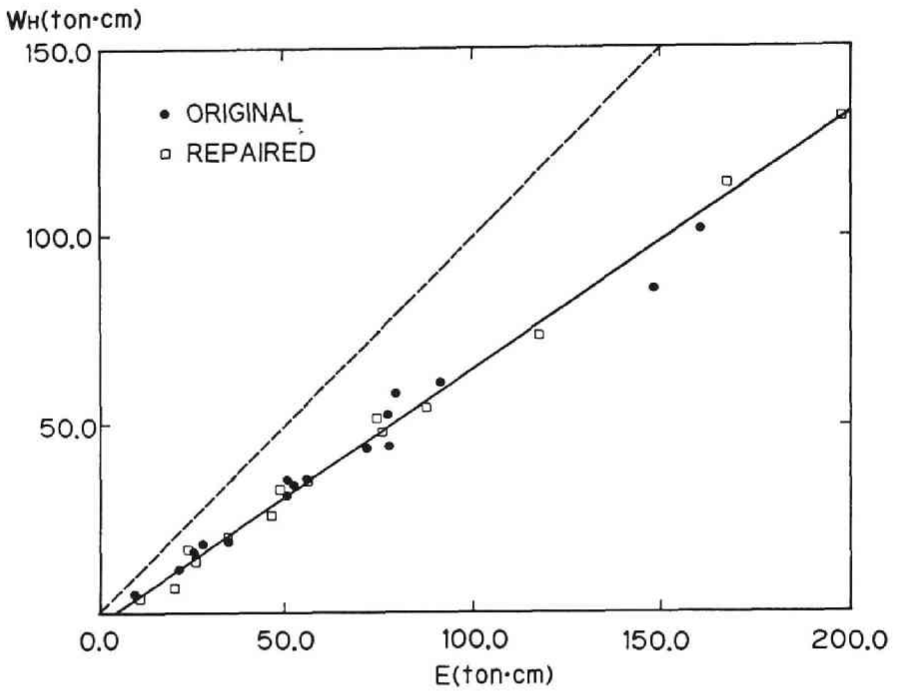

Figure 3.20 Relation of the hysteretic energy, W_H, to the total energy, E_T.

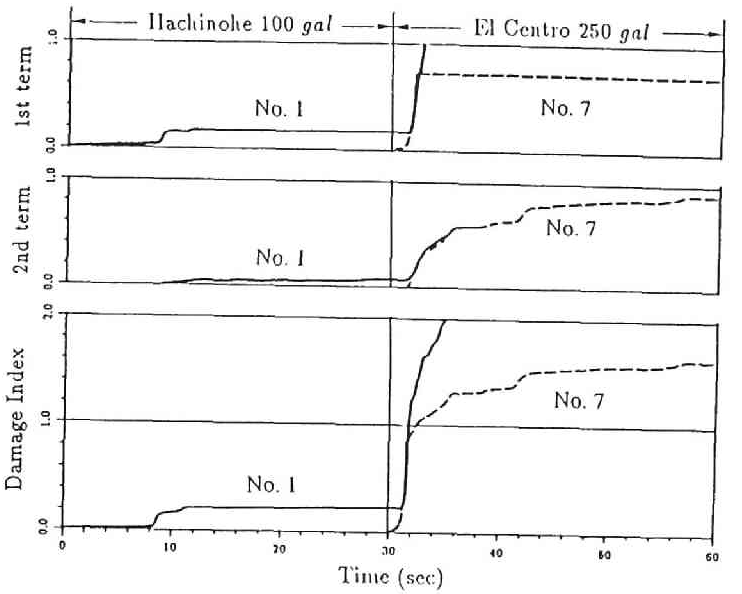

(a) Specimens 1 and 7.

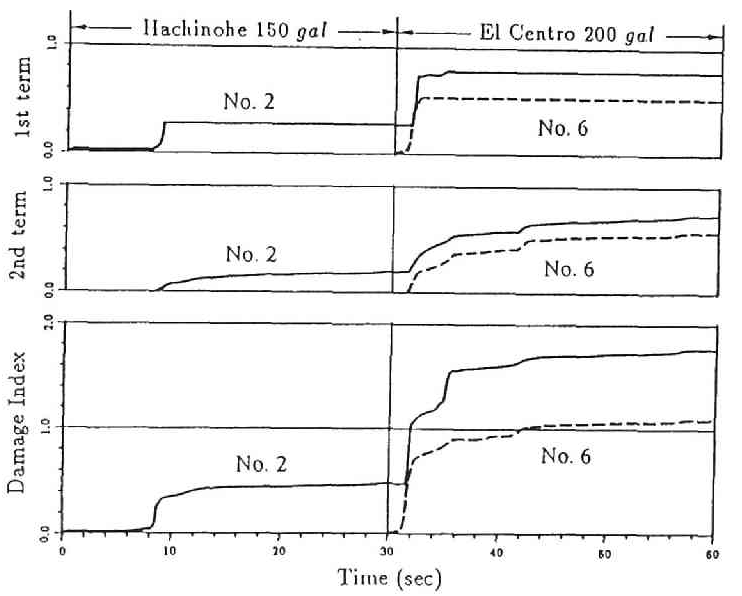

(b) Specimens 2 and 6.

Figure 3.21 Damage indices - time histories.

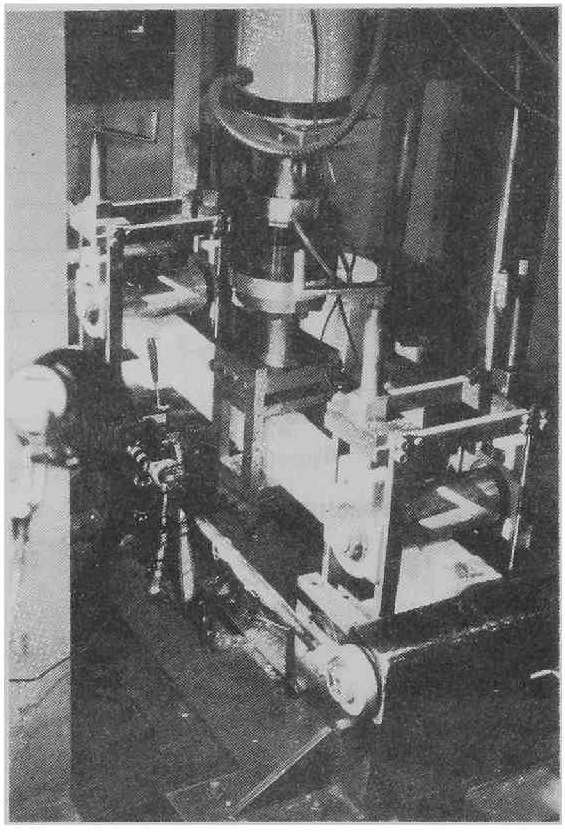

Photo 3.1 Hybrid loading system of earthquake response.

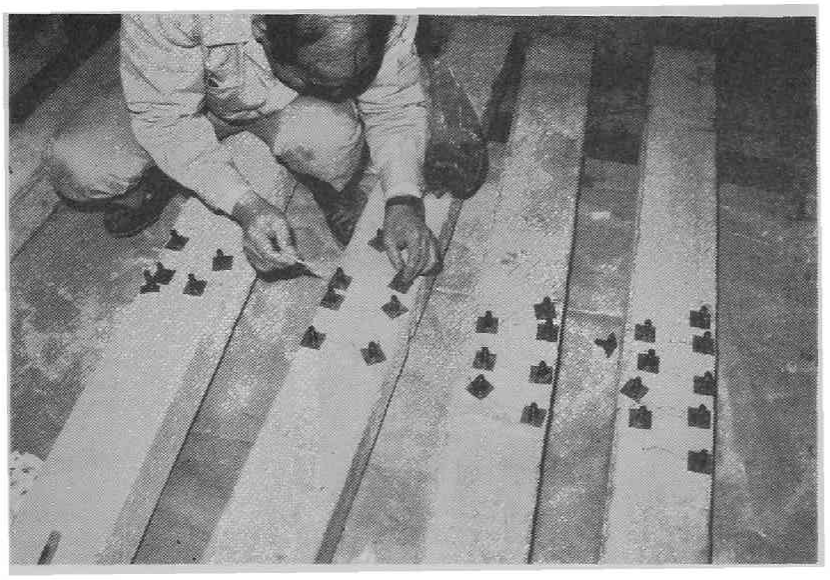

Photo 3.2 Type I repair: Setting pipes on the cracks.

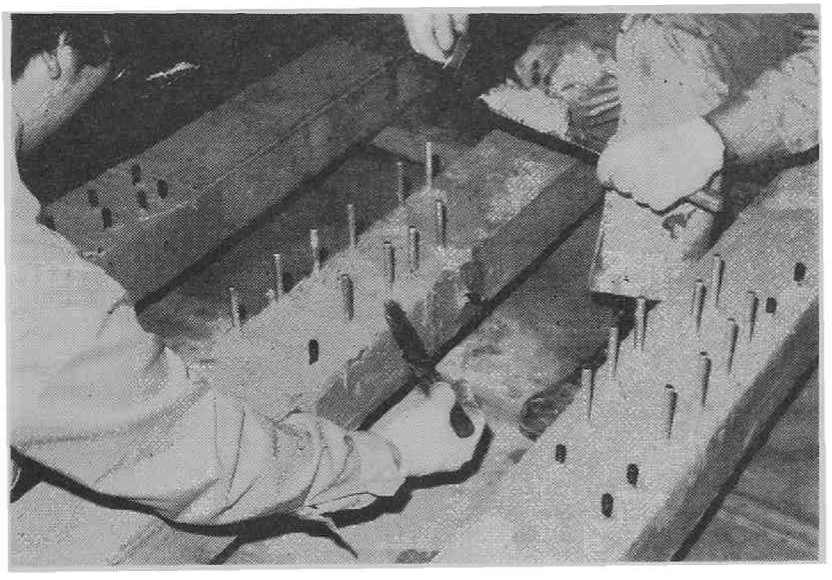

Photo 3.3 Type I repair: Sealing cracks with epoxy bond.

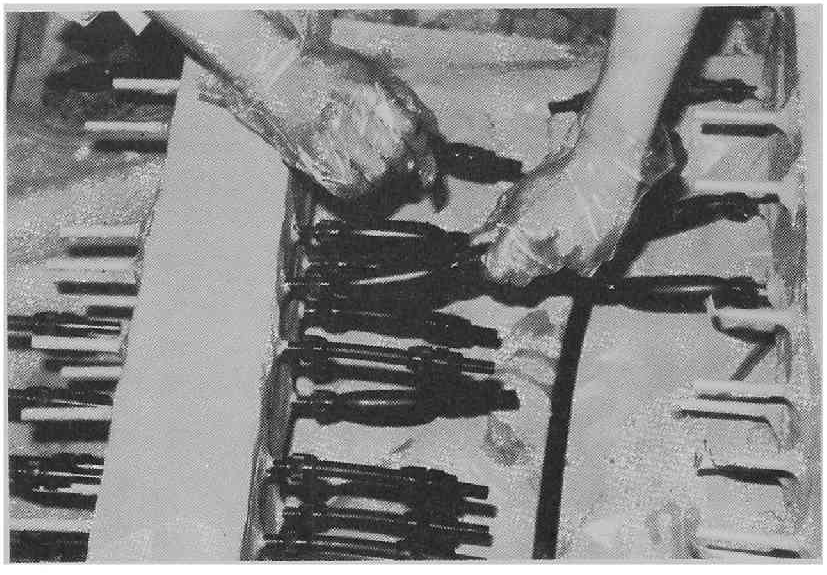

Photo 3.4 Type I repair: Grouting epoxy resin into gum tubes.

Photo 3.5 Type II repair: Welding new steel to the reinforcing bars.

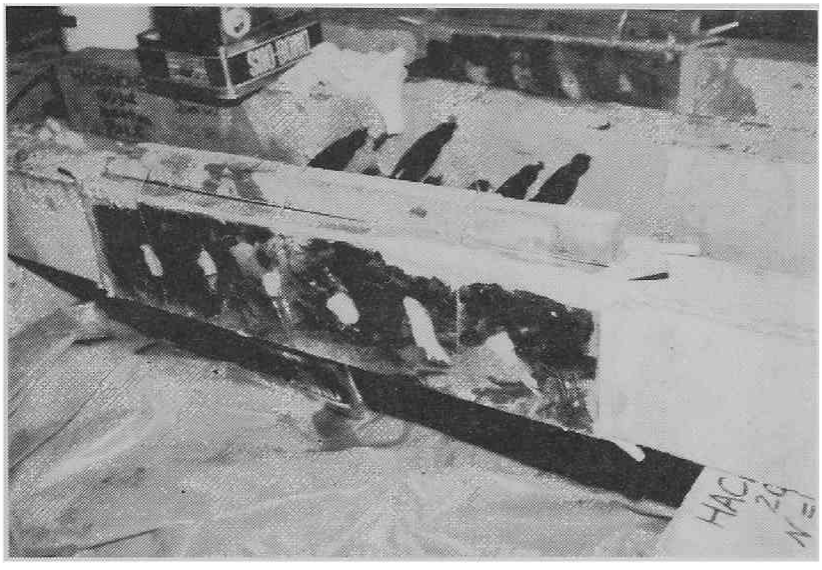

Photo 3.6 Type III repair: Setting steel plates around the specimen.

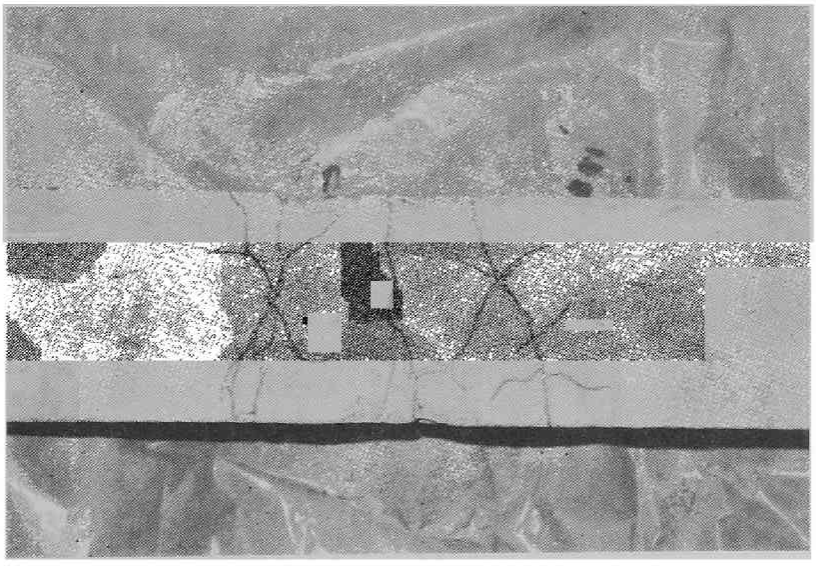

Photo 3.7 Cracks after the initial loading test of No. 4 specimen.

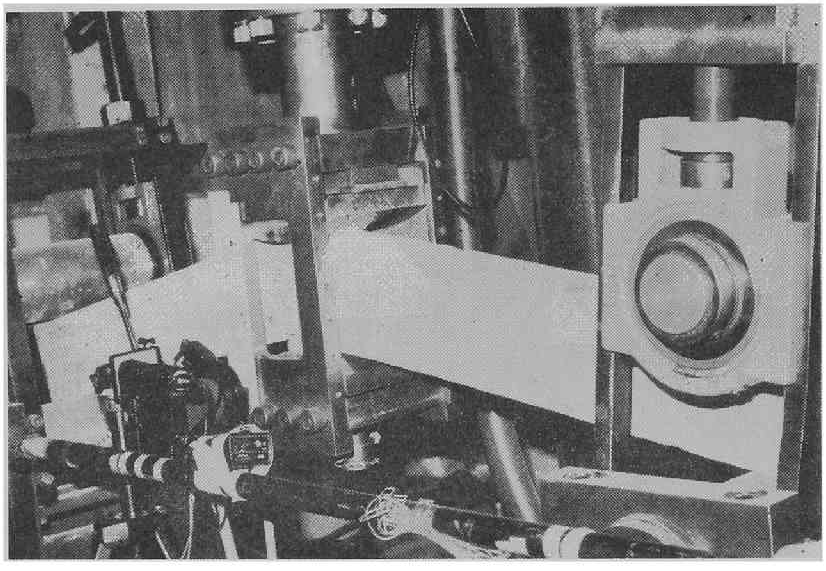

Photo 3.8 No. 8 specimen crushed after the second loading.

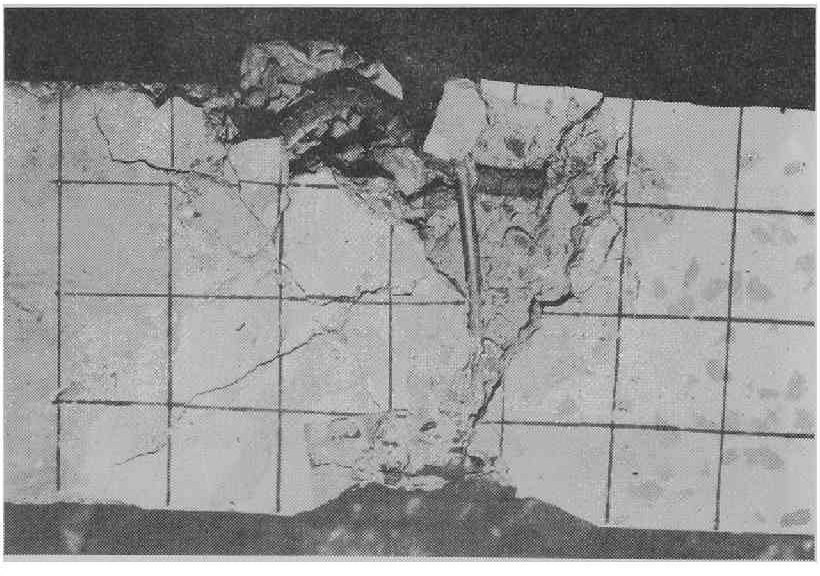

Photo 3.9 Crushed segment of No. 8 specimen.

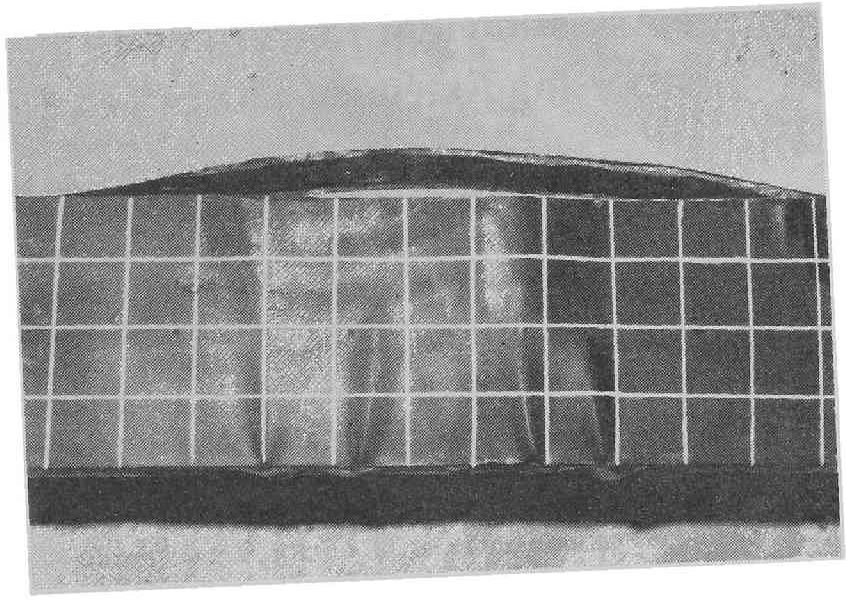

Photo 3.10 Buckled steel plate at midlength after loading tests.

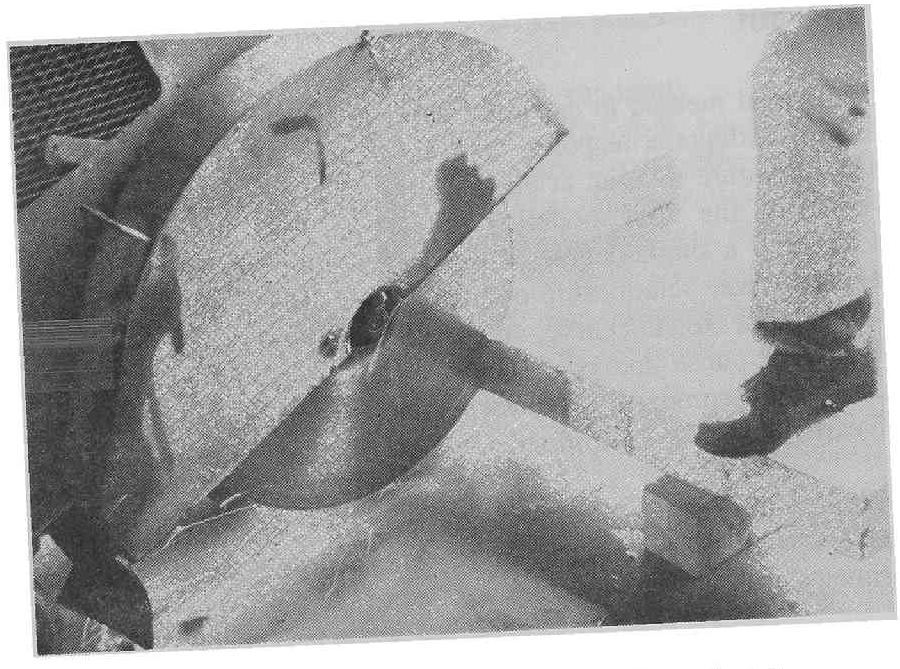

Photo 3.11 Diamond cutter used to cut specimens.

4. Inelastic Earthquake Response Analysis and Damage Assessment of Retrofitted RC Structures using Extended Fiber Model

4. 1 General Remarks

In this chapter, effectiveness of retrofit is evaluated analytically using extended fiber model.

The first part of this chapter introduces the method of analysis, the second part shows the verification examples using the test results of repaired reinforced concrete specimen, and the last part describes the application of this method to strengthening of bridge piers with reinforcements terminated at mid-height.

4. 2 Simplified Procedure to Quantify Effectiveness of Seismic Retrofit

Analytical method to calculate ultimate strength of RC bridge pier was applied to earthquake response analysis of retrofitted RC structures. First, moment-curvature relation at each section of a retrofitted RC structure was derived using the fiber modeling procedure. Then the force-displacement relationship of a single-degree-of-freedom system was derived based on the moment-curvature relationship of each section. Using the force-displacement relationship as a skeleton curve, an inelastic hysteretic model was assumed for earthquake response analysis. Lastly, effectiveness of seismic retrofit was evaluated from comparison between inelastic earthquake response during a future earthquake of the retrofitted structure and that of the original.

This simplified method does not calculate precise moment-curvature relation at each time step. Nevertheless, it shows good agreement with experiments as discussed in the next chapter.

Figure 4.1 shows the total flowchart of the proposed method. Precise procedure is described in the following.

4.2.1 Fiber Model including Repair Material

Conventional fiber modeling technique for RC structures [1] can be easily extended to include the repair material, such as epoxy resin and steel jacket. The ordinal fiber modeling technique calculates the stress of each fiber element based on the actual location of steel and concrete. The extended fiber model proposed here uses the same equation for the resin, of which real location is unknown, based on the approximated ratio of the resin to the total area of the cross section.

The assumed constitutive laws are shown in **Figure 4.2** and **Table 4.1**. **Figure 4.2-a** shows the assumed stress-strain relation of the confined and the unconfined concrete based on the Kent-Park model [2]. (Note that the plus strain in **Figure 4.2** means tensile strain.)

The reinforcing bars were modeled as shown in **Figure 4.2-b**. A maximum strength plateau was added to a bilinear curve in order to describe the ultimate behavior. Steel jacket was assumed to contribute to the moment-curvature relation of each section as additional reinforcing bars. Hence, the whole concrete of the retrofitted part is confined by the steel jackets.

As the grouted epoxy resin usually locates randomly in each section, precise location is unpredictable from outside. Therefore, epoxy resin was defined as an area ratio of its existence in this study. Epoxy resin was assumed to behave partially linear like **Figure 4.2-c**. The confined epoxy resin was assumed to withstand any tensile and compression force, and the unconfined epoxy resin was assumed to crush in compression. Young's modulus of epoxy resin is almost 10% of concrete, but is larger than concrete in tension. The nominal values for epoxy resin were determined from the tensile and the compression tests of the small test pieces.

Four critical points were determined using this extended fiber model as shown in **Figure 4.3**. These were the crack point (ϕ_{cr}, M_{cr}) where cracks of the concrete appear, the yield point (ϕ_y, M_y) where yield of the reinforcing bars occur, the maximum point (ϕ_{max}, M_{max}) where crush of the cover concrete occur, and the ultimate point (ϕ_u, M_u) where the core concrete crushes or the strength of the structure decreases to the assumed level. Four linear segments were used to connect these four critical points, so that the

moment-curvature relation was assumed to be piecewise linear.

An iterative technique was used to estimate the bending moment M which satisfies the equilibrium condition for the axial load acting on the section. This procedure is shown in the flowchart of **Figure 4.1**.

4.2.2 Hysteretic Model using Skeleton Curve

The force-displacement relationship was derived based on the moment-curvature relationship of each section. **Figure 4.4** shows examples of the loading point and the corresponding deformation for a simple beam and a bridge pier model. The deformation δ is calculated from integral of curvatures corresponding to the four critical moments mentioned above as follows:

$$\delta = \int_0^L \phi y \cdot dy \tag{4.1}$$

where y is measured from the pier top for a bridge pier, and from the support for a simple beam; L is a pier height for the pier model, and half a span length for a simple beam as shown in **Figure 4.4**.

Four points similar to the moment-curvature relationships were determined to approximate the relationship to piecewise linear in four lines as shown in **Figure 4.5**.

Using the force-displacement relationship as a skeleton curve, an inelastic hysteretic model was assumed for earthquake response analysis. One of the suitable hysteretic models for RC structures, 3-parameter model [3], was used in this study, which were precisely mentioned in Chapter 2. This inelastic model achieves various hysteretic properties using three parameters; α, β and γ. α represents stiffness degradation, β represents strength degradation due to hysteretic energy absorption, and γ represents pinching behavior through crack-opening and crack-closing procedure.

4.2.3 Effectiveness of Seismic Retrofit

Inelastic earthquake response analysis was carried out for the estimated model using several earthquake records. Then, response of the retrofitted structure during a future earthquake was compared with the original one to evaluate effectiveness of seismic retrofit. Three indices were used to evaluate quantitative effect of seismic retrofit; these were ductility, hysteretic energy

and the damage index [4]. Among the many indices used to evaluate response [4-10], ductility, energy absorbing capacity and a linear combination of these two are the basic indices. In evaluation of retrofit effect, the maximum restoring force under static loading is the most important checking point. However, ductility and energy absorbing capacities are also important for seismic retrofit in terms of earthquake hazard mitigation.

Ductility is defined as the ratio of the maximum deformation response δ_m to the yield deformation δ_y. Hysteretic energy is calculated as the area surrounded by the hysteretic load-deformation response curves which has strong correlation with the accumulated damage. Damage index is expressed as follows which were already mentioned in Chapter 2.

$$D = \frac{\delta_m}{\delta_u} + \frac{\beta}{P_y \delta_u} \int dE \tag{4.2}$$

in which, D is the damage index, δ_m is the maximum deformation response, δ_u is the defined ultimate deformation as shown in **Figure 4.5**, P_y is the yield strength also shown in **Figure 4.5**, $\int dE$ is the absorbed hysteretic energy and β is an empirical coefficient which takes the same value as β of the 3-parameter model. Note that δ_m is different from the static deformation at the maximum restoring force δ_{max} of **Figure 4.5**. A damage index of more than 1 represents severe damage or collapse.

4. 3 Verification Examples using Test Results

The models used in the experiments mentioned in Chapter 3 were numerically simulated using the proposed analytical procedure for verification.

4.3.1 Model for Simulations

A model of the specimen was divided into 50 sections and each section was divided into 52 fibers. **Figure 4.6** shows the discrete fiber elements for a cross section of the specimen. Repair had been done at the mid-span of the simple beam. Area of epoxy resin in each section was determined from the cross-sectional views of the repaired specimen cut into pieces after the loading tests mentioned in Chapter 3. Epoxy resin exists quite randomly in each

section, which shows difficulty in modeling this section exactly using ordinal fiber modeling technique or the finite element method. Therefore, the ratio of epoxy resin to the total area of each section was evaluated and was used as an average ratio of epoxy resin in each fiber; i.e., the estimated area of each fiber was assumed as epoxy resin. From the cross sectional view, epoxy resin was assumed to take 50% of the section area at the center span and linearly decreased to 0% at 30 *cm* from the center in each direction.

4.3.2 Static Load-Deformation Relation

First, force-deformation relation was compared between experiment and analysis shown in **Figure 4.7**. The experimental result for the original member had been derived from the static loading test while the results for the retrofitted members had been estimated from the skeleton curves of the hybrid loading tests. The ultimate point was defined to have the same strength as the yield point (where the reinforcing bars yield) or the 80% of the maximum restoring force.

The relation for the original specimen, the solid lines in **Figure 4.7**, shows good agreement between experiment and analysis except for the small range of deformation. As the tensile strength of concrete was neglected as shown in **Table 4.1**, the yield point of the reinforcing bars was underestimated. Assuming the tensile strength of concrete would improve the matching of analytically obtained relation with the experimental result in the small range of deformation. For the retrofitted specimens (the broken lines and the dotted lines in **Figure 4.7**), the analysis underestimated the strength compared with the experiments. Considering that the skeleton curves of the dynamic loading tests usually show higher strength, the analytically obtained force-deformation relation could give reasonable estimation.

Comparing the analytical force-deformation relation between the original and the retrofitted members, the retrofitted members showed higher yield strength and higher maximum strength than the original. Furthermore, the initial stiffness of the retrofitted member with grouted epoxy resin became smaller than the original while that of the retrofitted member with steel jackets became larger. These phenomena were also shown from the experimental results.

4.3.3 Hysteretic Load-Deformation Responses

Figures 4.8 (a)-(h) show some of the results comparing the experimental

and analytical hysteretic load-deformation responses before and after repair work with epoxy resin. These figures correspond to specimens 1-8 of the hybrid loading tests described in Chapter 3. Analytically obtained hysteretic responses successfully simulated the experimental results. Repaired specimens became stiffer than originals because the grouted epoxy resin has higher tensile strength than concrete. The evaluated maximum responses showed similar values as the experiments. The only significant difference was the behavior during strong earthquake motions such as the El Centro record with the maximum acceleration scaled to 300 gal shown in **Figure 4.8-h**. The analytical results showed stable hysteretic responses even for the strong input motions while the specimen collapsed in the experiments. This is probably due to the assumption of completely retrofitted steel materials used in the analysis, but in reality the buckled reinforcing steel bars in the specimen were ineffective. This simplified analysis estimates seismic response time histories of the total pier. On the contrary, response time histories of each fiber nor status of steel at each time step are not evaluated in this analysis. Degrading Young's modulus of damaged steel might be needed to consider precisely the effect of the first loading to the second loading.

4.3.4 Indices for Energy Dissipation and Damage

Figure 4.9 compares analytically obtained hysteretic energy with experimentally obtained hysteretic energy and **Figure 4.10** compares their corresponding damage indices. The dashed line means the same values were obtained from both the experiments and the analysis. All dots scattered around this line, which shows the estimated hysteretic energy and damage index were in good agreement with the experimental results. Hysteretic energy of original specimens was estimated to an accuracy within 10% for weak input motions.

The damage indices were also estimated with errors of only 0.1-0.2. However, this analysis underestimated hysteretic energy 20-30% for strong input motions because of its stable hysteretic responses as discussed before. For repaired specimens, ratio of epoxy resin to concrete in each fiber was determined from only one specimen shown in Chapter 3 (**Figure 3.14**), and the identical values were assumed for all the repaired specimens. Therefore, errors in estimations were larger than the original specimens. However, the judgement, from the damage index, whether the specimen will collapse or not; i.e., the damage index overcomes 1.0 or not, was the same for all the specimens.

4. 4 Application to Bridge Pier with Terminated Reinforcement

Some old bridge piers constructed under old codes have insufficient anchorage length and termination of their main reinforcement [11]. These structures might suffer a brittle shear failure at mid-height where the reinforcement terminated and need strengthening for future earthquakes. Use of steel jackets has been found applicable from experiments to prevent brittle failure [11]. The proposed analytical method was then applied to evaluate effect of strengthening for the bridge piers with reinforcements terminated at mid-height.

4.4.1 Model for Simulations

T-shape bridge pier of $13m$ high shown in **Figure 4.11** was modeled to have the terminated main reinforcement. This pier was designed basically on the specification of highway bridge piers [12] and 30% of the main reinforcing bars were intentionally terminated at 3.0 m high to model an old type pier. The cross section has rectangle shape of 3.5 m $\times$ 3.0 m as shown in **Figure 4.12.**

Then, the pier was divided into 50 sections and the moment-curvature relationship of each section was calculated using more than 120 fibers as shown in **Figure 4.13. Figure 4.13(a)** shows the discrete fiber elements for a cross section below the termination point for the reinforcing bars and **Figure 4.13(b)** shows that of above the termination point. As in this figure, the inner most reinforcing bars were terminated at midheight. **Figure 4.14(a)** shows the calculated moment-curvature relationship for each section of the original pier. The ultimate state was defined as the crush of the core concrete because of its simple calculation. This figure shows that crushing may occur at 3.0 m high where the reinforcement terminated.

Four types of steel jackets were considered: (A) $1mm$ thick plate which covers only at midheight; (B) $2mm$ thick plate which covers only at midheight; (C) $1mm$ thick plate which covers from bottom to midheight; and (D) $2mm$ thick plate which covers from bottom to midheight. For (A) and (B), the pier was covered with the steel jackets only at the midheight where the reinforcing bars had been terminated, i.e., the retrofitted pier has the steel belt at midheight and the no-strengthened pier bottom. The vertical width of the steel jackets for (A) and (B) was set to have the same length as the pier width (=$3.5m$) based on Ref. 11. Steel jackets were assumed to bonded perfectly to the concrete surface through the seismic response regardless of epoxy resin bond. **Figures**

4.14(b) and **4.14(c)** show the moment-curvature relationships for the strengthened bridge pier with steel jackets for cases (A) and (B). Thicker steel jackets gave smaller curvature at the section where the reinforcement had been terminated. The critical place moved from the mid-height to the bottom, which means the strengthening had been done effectively. Note that the pier bottom of (A) and (B) had not been retrofitted.

4.4.2 Static load-Deformation Relation

The calculated force-deformation relationship for the pier top is shown in **Figures 4.15** and **4.16**. **Figure 4.15** shows the comparison between the original and retrofitted piers in cases (A) and (B), and **Figure 4.16** is for cases (C) and (D). The solid line is for the original pier, the dashed line in **Figure 4.15** is for (A) the strengthened pier with $1mm$ thick steel jackets only at midheight; the dotted line in **Figure 4.15** is for (B) the strengthened pier with $2mm$ thick steel jackets only at midheight; and the dashed line in **Figure 4.16** is for (C) the strengthened pier with $1mm$ thick steel jackets from bottom to midheight; the dotted line in **Figure 4.16** is for (D) the strengthened pier with $2mm$ thick steel jackets from bottom to midheight.

The pier bottom where no strengthening had been done became the critical place for the strengthened piers for (A) and (B). Therefore, the ductility decreased because of the stiffer structure with the same ultimate strength as the original. For (C) and (D), both the ductility and the maximum restoring force increased for the retrofitted piers comparing with the original one. The pier with $2mm$ jackets of case (D) showed larger restoring force compared to the $1mm$ jackets of case (D), however, it showed smaller ductility.

4.4.3 Inelastic Earthquake Responses

The inelastic earthquake response analysis was done using the Type 3 earthquake which was recommended in the Japanese seismic code [13] for the soft ground (**Figure 4.17**). Though the original structure may collapse in shear failure, the proposed analytical method cannot determine the failure mode nor the dynamic behavior of each section at each time step because it considers the structure as an SDOF system. Therefore, the parameter γ in the 3-parameter hysteretic model, which represents pinching effect, was set to 0.5 for the original structure to express its shear behavior. The hysteretic responses of them for the 3 times larger input acceleration as the design code are shown in **Figure 4.18**. Strengthened structure showed more stable responses than the

original.

The absorbed hysteretic energy, the damage index of the original and strengthened bridge piers including the other indices are shown in **Table 4.2.** Some indices showed similar values for the original and retrofitted structures. All ductility factors remained about 1, and all the ratios of hysteretic energy to the total input energy were 0.6. Though the absorbed energy became smaller for the partially strengthened structures of (A) and (B), they showed larger values for the damage index because of their low ductility. Furthermore, the retrofitted pier with $2mm$ thick steel jackets showed larger damage index than $1mm$ thick steel jackets for the same reason.

The fully retrofitted piers of (C) and (D) showed smaller displacement responses and larger restoring forces, which means they became stiffer than the original. Though the retrofitted piers showed smaller damage indices, the retrofitted pier with 2mm thick steel jackets of case (D) showed larger damage index than 1mm thick steel jackets of case (C) because of its lower ductility.

Effectiveness of thinner jackets was verified, of which thickness is thick enough to change the critical place from the midheight to the pier bottom. Strengthening at the pier bottom may also be needed to satisfy ductility requirement as in cases (C) and (D). The retrofitted piers in cases (A) and (B) showed more stable hysteretic responses than the original which means the retrofit work decreased the seismic risk, however, their damage indices became larger compared with the original. The failure mode of the structure could not be evaluated with the damage index.

4.4.4 Sensitivity Analysis on Quantity of Epoxy Resin

Amount and precise location of epoxy resin is hard to probe from outside. Therefore, sensitivity was studied on quantity of grouted epoxy resin. 10% and 20% of each strengthened section was assumed to be grouted with epoxy resin. These simulations may represent the case that the pier already had some cracks to be repaired at mid-height, or steel jackets were bonded to the pier with epoxy resin. The thickness of the steel jackets was selected to $1mm$ which covers from the bottom to the midheight (case C).

Figure 4.19 shows the damage index and absorbed hysteretic energy for each case. As epoxy resin increases, the damage index also increases and the hysteretic energy decreases. However, the difference is smaller than 1% for the hysteretic energy and 0.07 for the damage index. Considering the large ratio of

20% for epoxy resin in each section, the quantity of epoxy resin affects little to seismic behavior of strengthened bridge pier. The effect of epoxy resin is small enough to neglect it for seismic response analyses of bridge piers with steel jackets, if the steel jackets are perfectly bonded to the concrete surface.

4. 5 Conclusions

Analytical methods for inelastic earthquake response and damage assessment of retrofitted RC structures was studied. The main conclusions obtained are as follows:

(1) Analytical methods for inelastic earthquake response analysis was proposed using the skeleton curves obtained from the fiber model extended to include repair materials.

(2) Analytically obtained hysteretic load-deformation responses, absorbed hysteretic energy and damage indices were in good agreement with the experimental results. The hysteretic responses of both original and retrofitted RC members can be modeled by the proposed method with high accuracy.

(3) Aseismic behavior of the strengthened bridge pier was simulated, and effectiveness of thinner steel jackets was verified. Existence of epoxy resin in strengthened bridge pier with steel jackets was negligible for dynamic behavior if the steel jackets had been bonded perfectly to the concrete surface during earthquake response.

References of Chapter 4

1) Park, R. and Paulay, T., *Reinforced Concrete Structures*, John Wiley & Sons, New York, 1975.
2) Kent, D. C. and Park, R., "Flexural members with confined concrete", *Journal of the Structural Division*, ASCE, Vol. 97, ST7, pp. 1969-1990, 1971.
3) Park, Y.J., Reinhorn, A.M. and Kunnath, S.K., "Seismic damage analysis of reinforced concrete buildings", *Proc. of the 9th World Conference on Earthquake Engineering*, Vol. VII, pp. 211-216, 1988.
4) Park, Y.J., Ang, A.H.-S. and Wen, Y.K., "Seismic Damage Analysis and Damage-Limiting Design of RC Buildings", *Research Report, University of Illinois*, No. 516, October 1984.
5) Park, Y.J. and Ang, A.H.-S., "Mechanistic seismic damage model for reinforced concrete", *Journal of Structural Engineering*, ASCE, Vol. 111, pp. 722-739, 1985.
6) Japan Road Association, *Manual for Seismic Countermeasure Methods for Roads against Earthquakes*, 1988 (in Japanese).
7) Dong, W., Chiang, W.-L., Shah, H.C. and Wong, F.S., "Failure possibility of existing buildings", *Civil Engineering Systems*, Vol. 6, No. 4, pp. 170-179, 1989.
8) Dipasquale, E. and Cakmak, A.S., "On the relation between local and global damage indices", *NCEER*, No. 89-0034, 1989.
9) Kawashima, K. and Unjoh, S., "An inspection method of seismic vulnerability of existing highway bridges", *Proc. of the Japan Society of Civil Engineers*, No. 416/I-13, pp. 155-162, 1990.
10) Nishimura, A., "Judgement of the structural integrity of bridge foundation with the percussion test for structure response", *Proc. of the 8th Japan Earthquake Engineering Symposium*, pp. 2163-2168, 1990 (in Japanese).
11) Kawashima, K., Unjoh, S. and Iida, H., "Seismic inspection and seismic strengthening of reinforced concrete bridge piers with termination of main reinforcement at mid-height", *Proc. of the 1st U.S.-Japan Workshop on Seismic Retrofit of Bridges*, pp. 251-279, 1990.
12) Hanshin Highway Public Corporation, *General Figures for Reinforced Concrete Structures*, 1991.
13) Japan Road Association, *Seismic Design Code, Specifications for Highway Bridges in Japan*, Part V, 1990 (in Japanese).

Table 4.1 Assumed constitutive laws for concrete, steel and epoxy resin.

(a) Concrete (Based on Ref. 2)

Unconfined	Confined
for $\varepsilon_c \le -0.0035$ $f_c = 0$	for $\varepsilon_c \le \varepsilon_{20c}$ $f_c = 0.2 f_c'$
for $-0.0035 < \varepsilon_c \le -0.002$ $f_c = (\varepsilon_c + 0.0035) f_c' / 0.0015$	for $\varepsilon_{20c} < \varepsilon_c \le -0.002$ $f_c = f_c' \{1 - Z(\varepsilon_c - 0.002)\}$
for $-0.002 < \varepsilon_c \le 0$ $f_c = -f_c' \{2\varepsilon_c / 0.002 - (\varepsilon_c / 0.002)^2\}$	
for $\varepsilon_c > 0$ $f_c = 0$	
Z: parameter for the slope of the falling branch[2)] $f_c' = -196$ kgf / cm^2 (−19 MPa) ε_{20c}:strain at which concrete stress becomes $0.2 f_c'$	

(b) steel stress-strain relationship

for $\varepsilon_s \le -\varepsilon_{su}$, $\varepsilon_s > \varepsilon_{su}$ $f_s = f_{su}$
for $-\varepsilon_{su} < \varepsilon_s \le -\varepsilon_{sy}$, $\varepsilon_{sy} < \varepsilon_s \le \varepsilon_{su}$ $f_s = (\varepsilon_s - \varepsilon_{sy})(f_{su} - f_{sy}) / (\varepsilon_{su} - \varepsilon_{sy}) + f_{sy}$
for $-\varepsilon_{sy} < \varepsilon_s \le \varepsilon_{sy}$ $f_s = E_s \varepsilon_s$
$E_s = 2{,}100{,}000$ kgf / cm^2 (0.21 TPa) $f_{sy} = 3{,}500$ kgf / cm^2 (0.34 GPa) $f_{su} = 5{,}000$ kgf / cm^2 (0.49 GPa) $\varepsilon_{sy} = 0.001667$ $\varepsilon_{su} = 0.2$

(c) epoxy resin stress-strain relationship

Unconfined	Confined
for $\varepsilon_e \le -\varepsilon_m$ $f_e = 0$	for $\varepsilon_e \le -\varepsilon_m$ $f_e = -f_e'$
for $-\varepsilon_m < \varepsilon_e \le \varepsilon_m$ $f_e = E_e \varepsilon_e$	
for $\varepsilon_e > \varepsilon_m$ $f_e = f_e'$	
$E_e = 25{,}000$ kgf / cm^2 (2.5GPa) $\varepsilon_m = 0.02$ $f_e' = 500$ kgf / cm^2 (49 MPa)	

Table 4.2 Response of original and strengthened bridge piers.

	Original	(A) Partially Strengthened with 1 mm steel	(B) Partially Strengthened with 2 mm steel	(C) Fully Strengthened with 1 mm steel	(D) Fully Strengthened with 2 mm steel
Ductility Factor;μ	1.12	1.09	1.09	1.03	0.98
Maximum Displacement (cm)	8.1	7.7	7.5	7.6	7.3
Maximum Force (tonf)	743.1	743.3	743.7	781.6	804.0
Maximum Velocity (kine)	60.7	58.2	57.5	59.7	60.3
Damage Index	0.52	0.55	0.60	0.41	0.42
1st term of Damage Index	0.11	0.11	0.12	0.09	0.09
2nd term of Damage Index	0.42	0.44	0.48	0.32	0.33
Hysteretic Energy; W_H (tonf·cm)	47573	43959	43452	44226	42853
Total Input Energy; E (tonf·cm)	79463	72789	71818	73792	71825
W_H/E	0.599	0.604	0.605	0.599	0.597

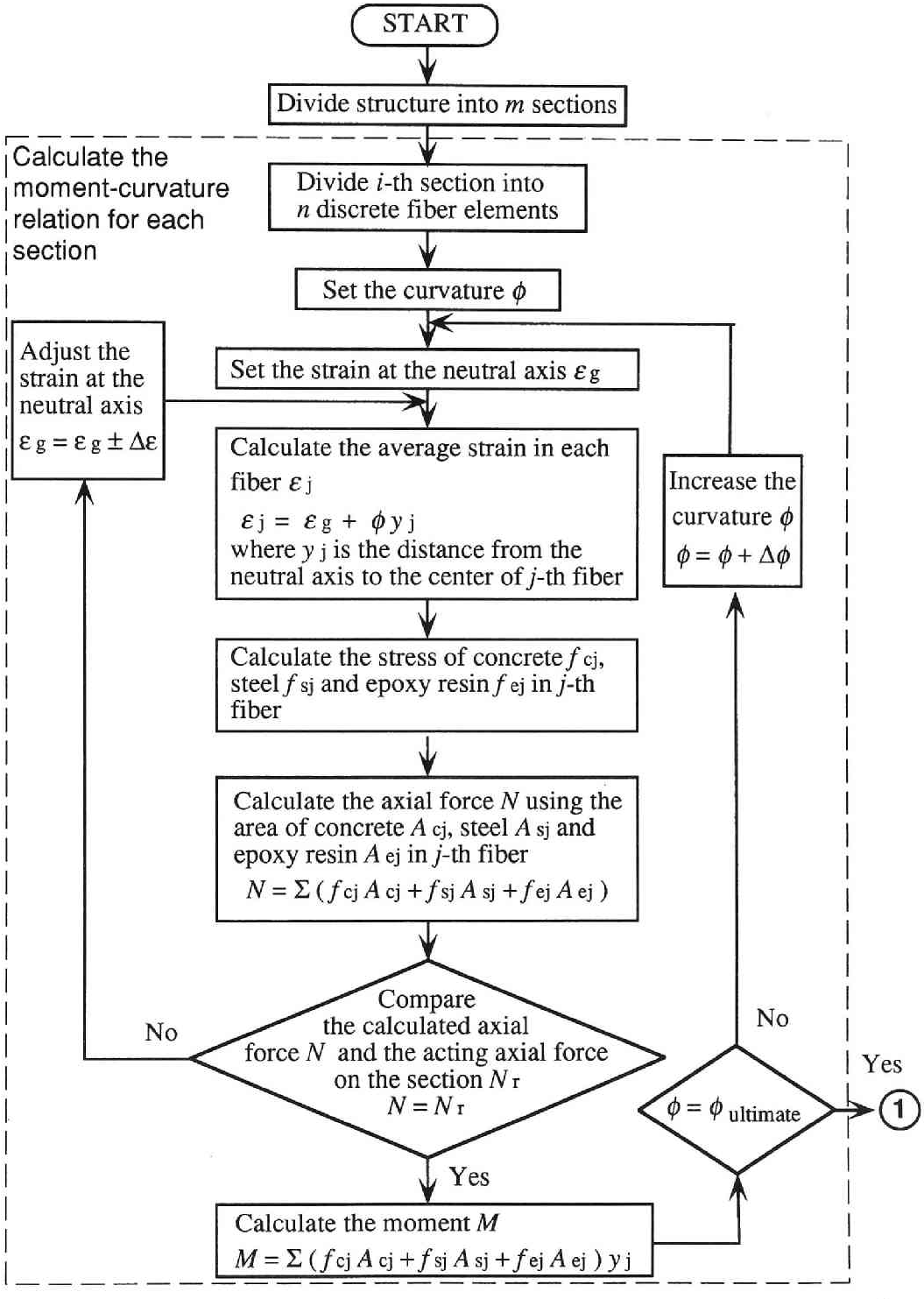

Figure 4.1 Flowchart of the procedure to quantify effectiveness of seismic retrofit.

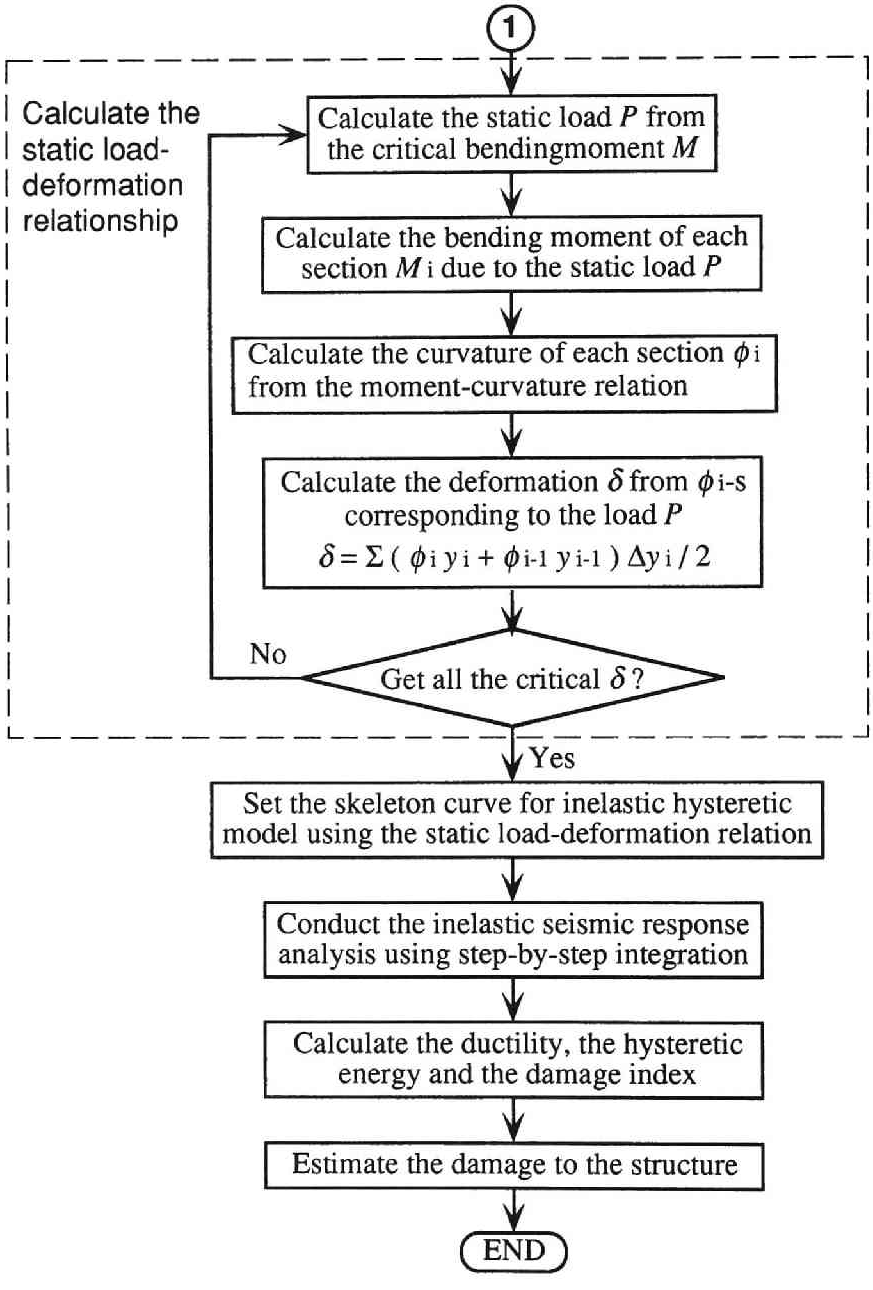

Figure 4.1 Continued.

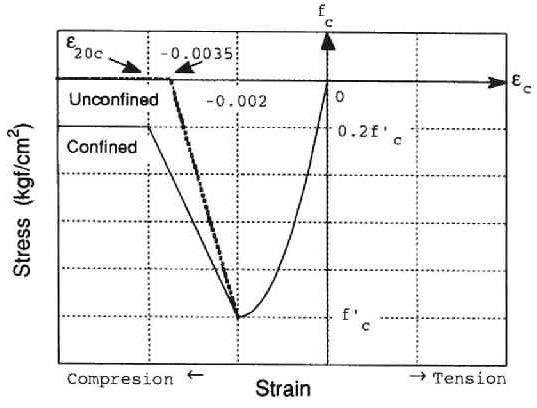

(a) Concrete

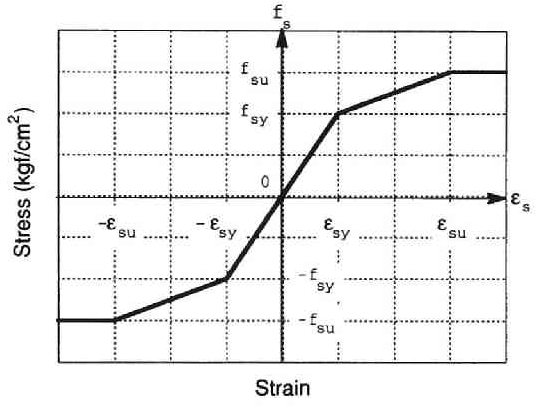

(b) Steel

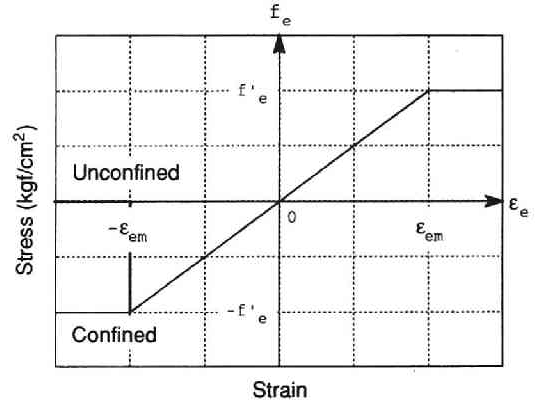

(c) Epoxy resin

Figure 4.2 Assumed stress-strain relationship.

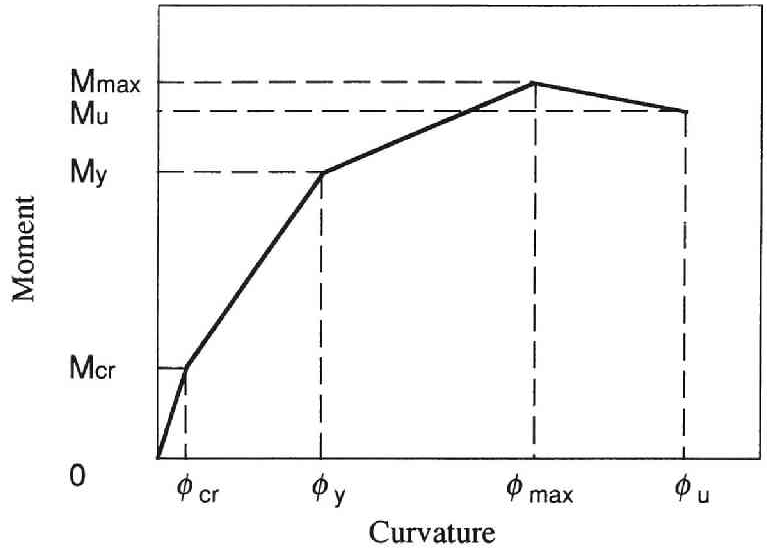

Figure 4.3 Assumed moment-curvature relationship.

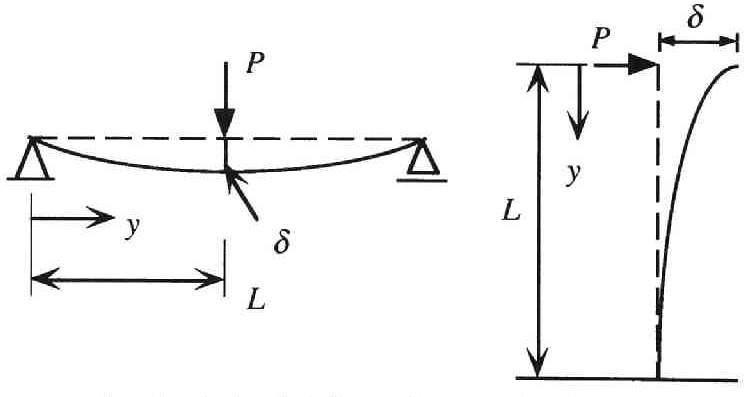

Figure 4.4 Static load-deformation relation based on the moment-curvature relation of each section.

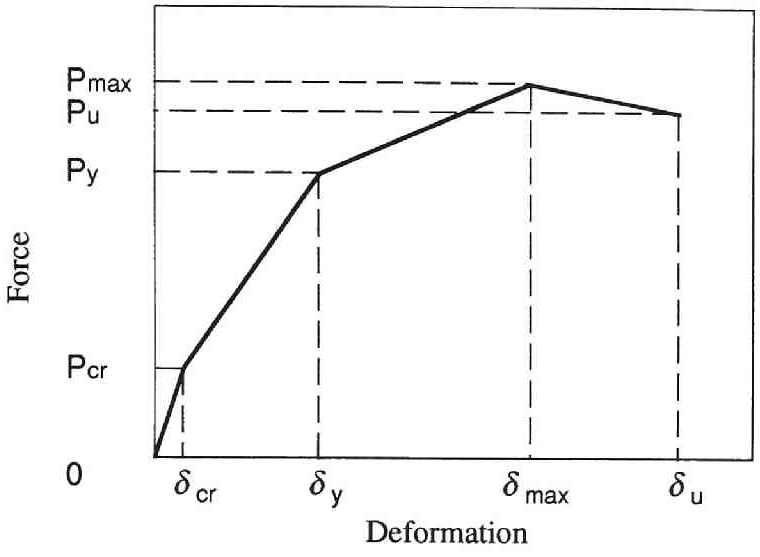

Figure 4.5 Assumed skeleton curve using staticload-deformation relationship.

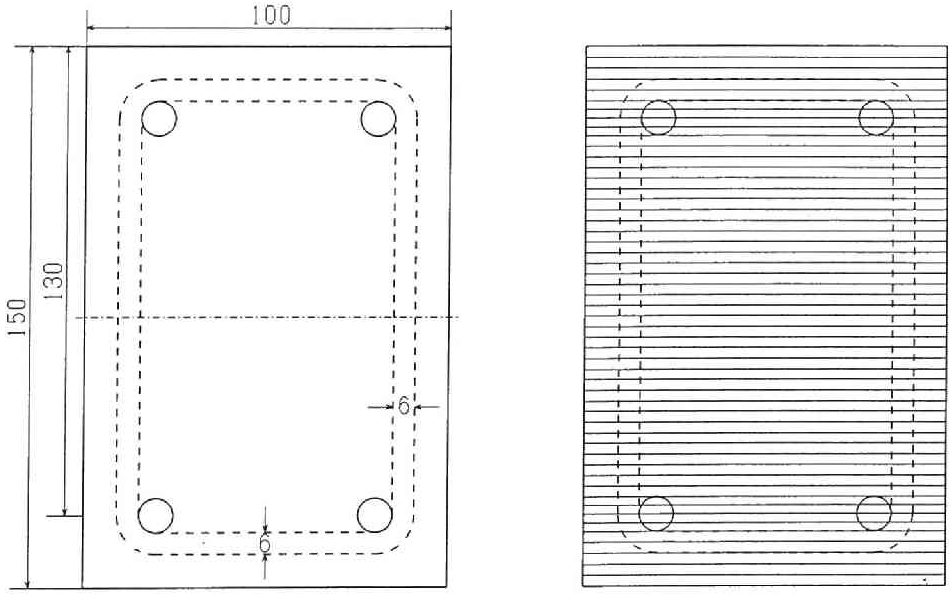

Figure 4.6 Discrete fiber elements for a cross section of the specimen.

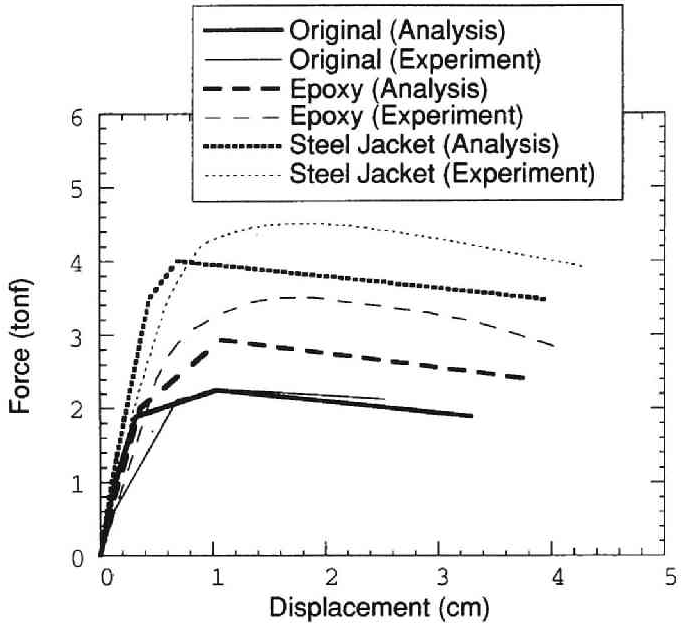

Figure 4.7 Force-displacement relation of analytical and experimental results

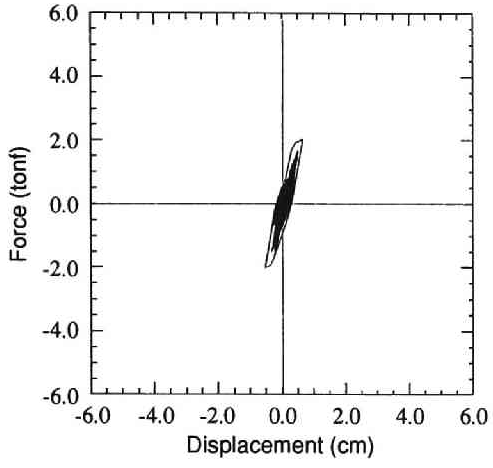

(i) Analytical result for original specimen.

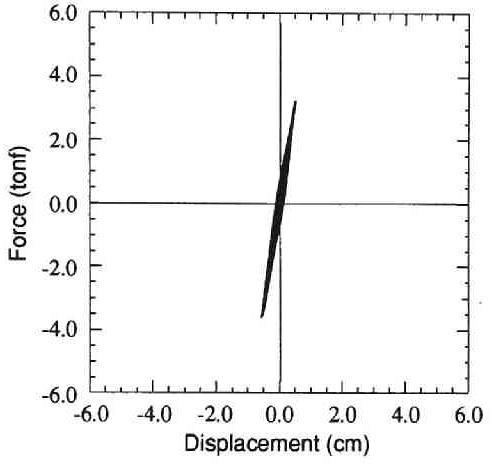

(ii) Analytical result for repaired specimen.

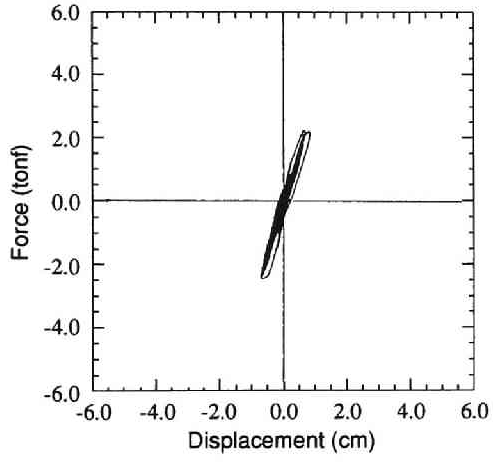

(iii) Experimental result for original specimen.

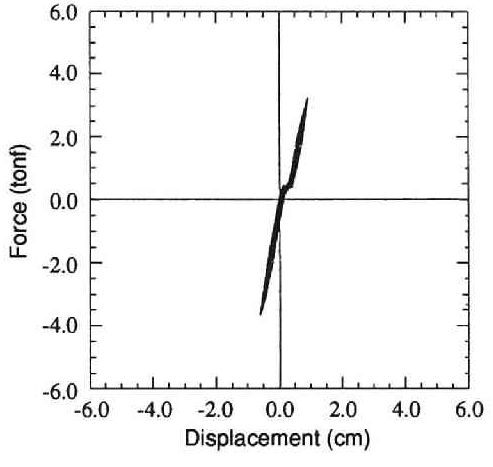

(iv) Experimental result for repaired specimen.

Figure 4.8 (a) Comparison of hysteretic loops between analysis and experiment for original and repaired specimens.
(No. 1 specimen of Chapter 3, Hachinohe record A_{max}=100 gal, Repaired with steel plate covering method)

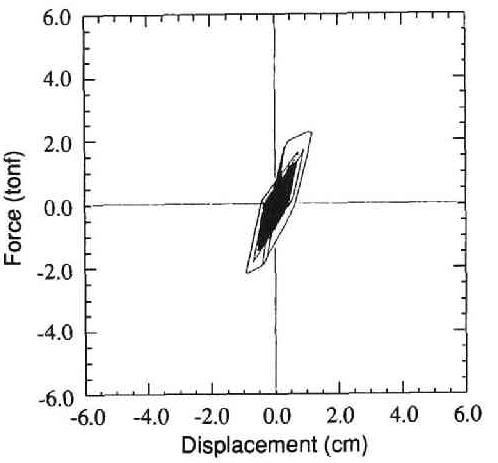

(i) Analytical result for original specimen.

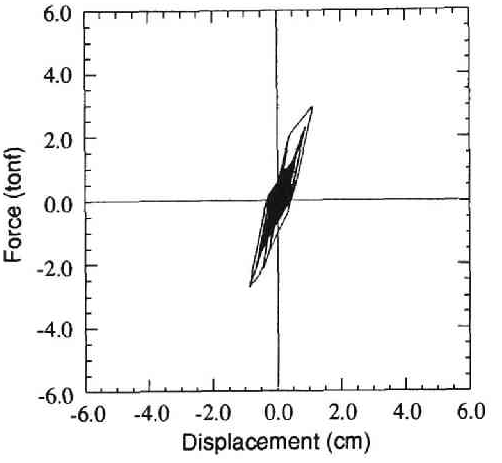

(ii) Analytical result for repaired specimen.

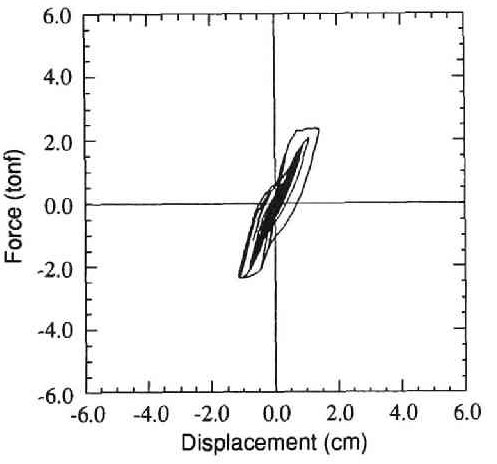

(iii) Experimental result for original specimen.

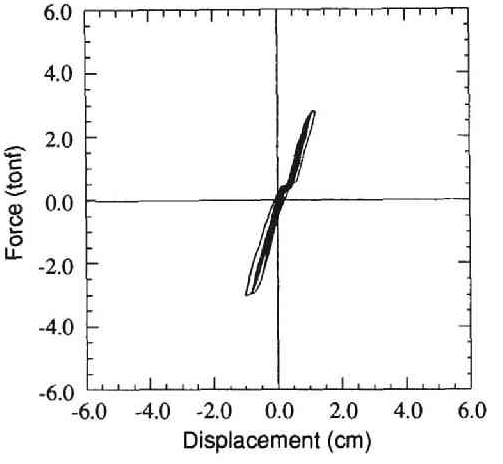

(iv) Experimental result for repaired specimen.

Figure 4.8 (b) Comparison of hysteretic loops between analysis and experiment for original and repaired specimens.
(No. 2 specimen of Chapter 3, Hachinohe record A_{max}=150 gal, Repaired with epoxy resin grouting method)

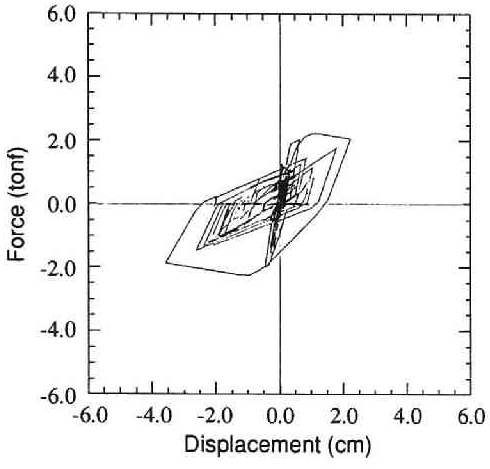

(i) Analytical result for original specimen.

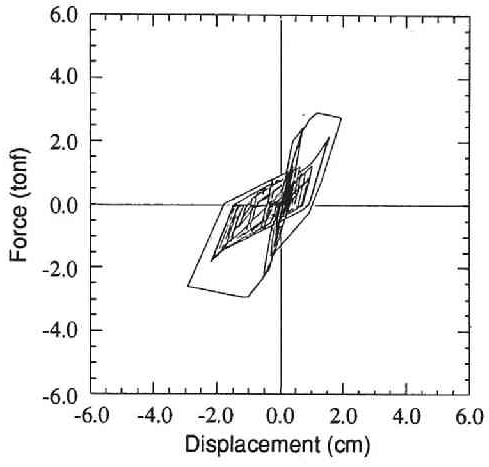

(ii) Analytical result for repaired specimen.

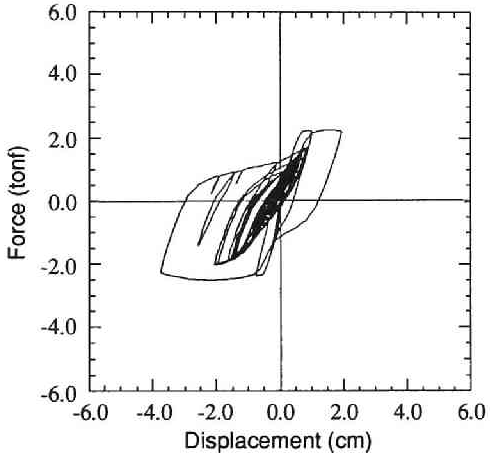

(iii) Experimental result for original specimen.

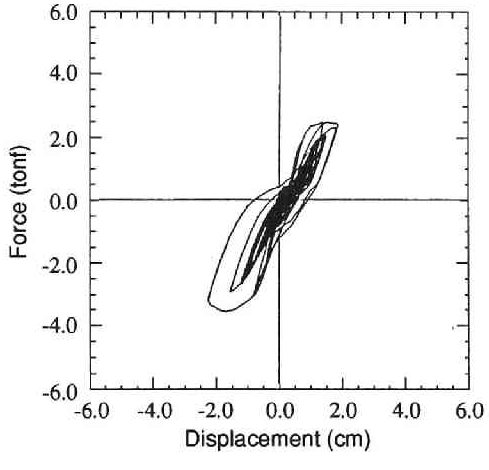

(iv) Experimental result for repaired specimen.

Figure 4.8 (c) Comparison of hysteretic loops between analysis and experiment for original and repaired specimens.
(No. 3 specimen of Chapter 3, Hachinohe record A_{max}=250 gal, Repaired with epoxy resin grouting method)

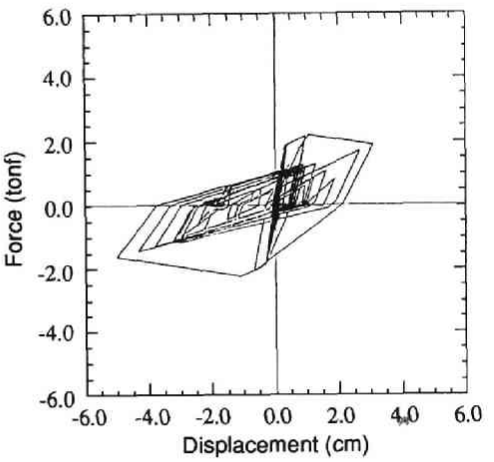

(i) Analytical result for original specimen.

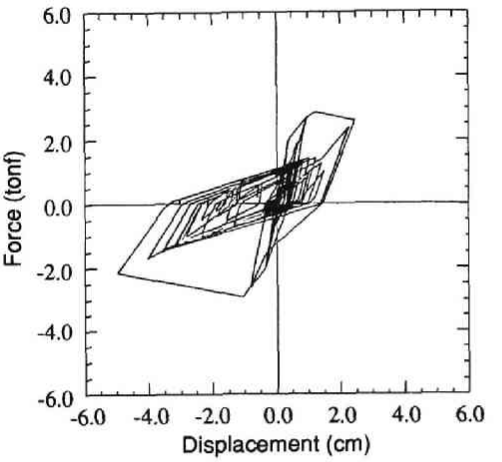

(ii) Analytical result for repaired specimen.

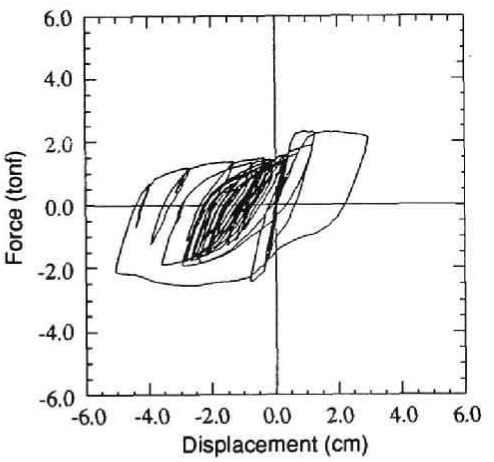

(iii) Experimental result for original specimen.

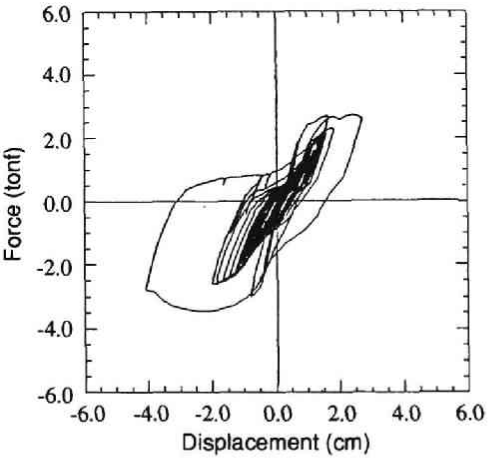

(iv) Experimental result for repaired specimen.

Figure 4.8 (d) Comparison of hysteretic loops between analysis and experiment for original and repaired specimens.
(No. 4 specimen of Chapter 3, Hachinohe record A_{max}=300 gal, Repaired with epoxy resin grouting method)

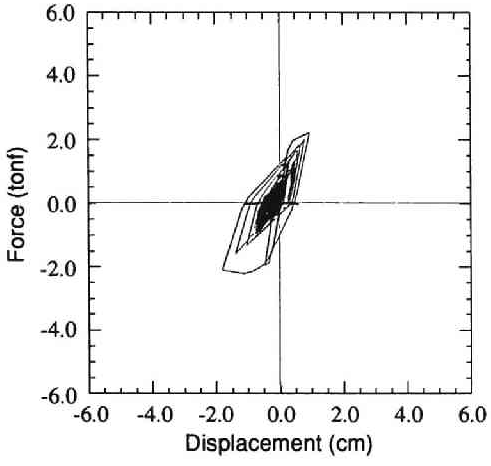

(i) Analytical result for original specimen.

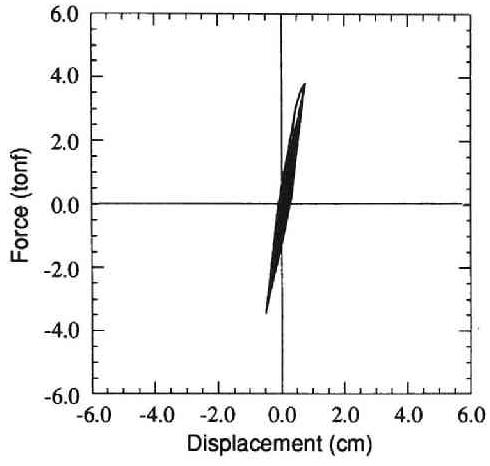

(ii) Analytical result for repaired specimen.

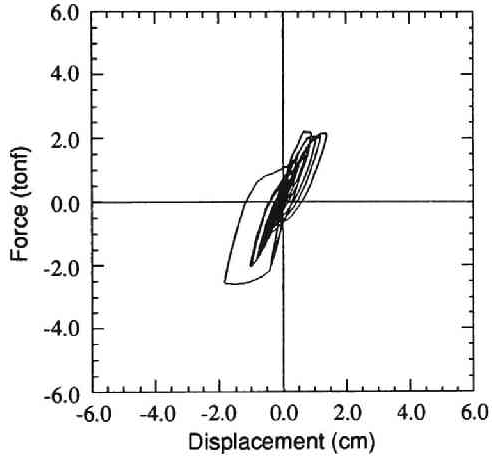

(iii) Experimental result for original specimen.

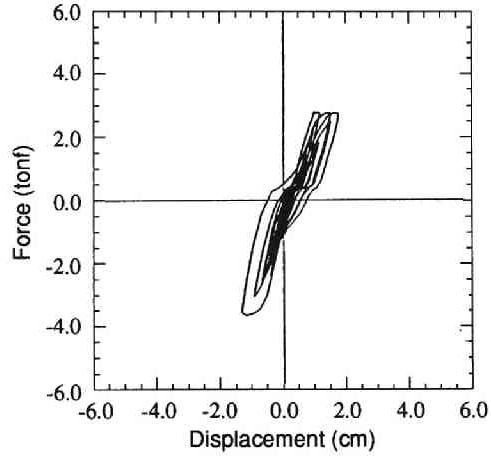

(iv) Experimental result for repaired specimen.

Figure 4.8 (e) Comparison of hysteretic loops between analysis and experiment for original and repaired specimens.
(No. 5 specimen of Chapter 3, El Centro record A_{max}=150 gal, Repaired with steel plate covering method)

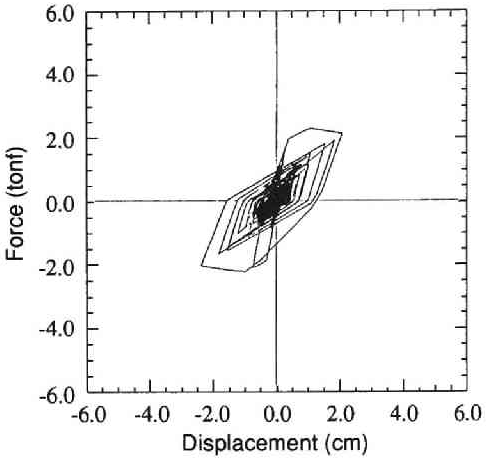

(i) Analytical result for original specimen.

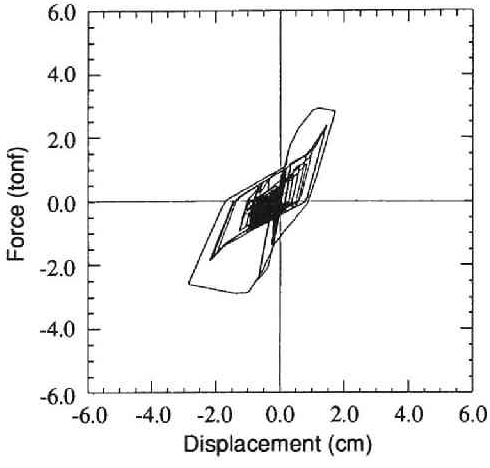

(ii) Analytical result for repaired specimen.

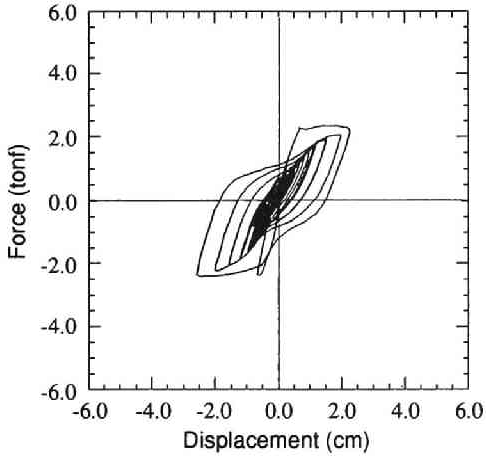

(iii) Experimental result for original specimen.

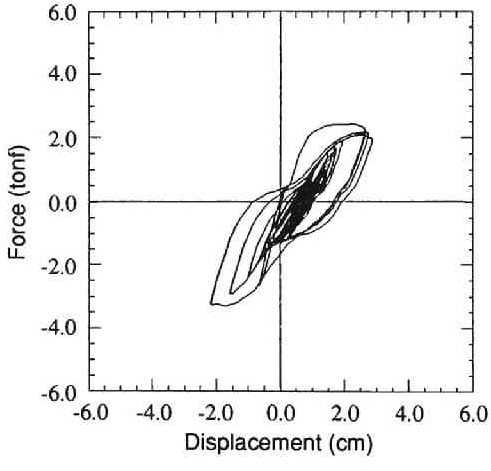

(iv) Experimental result for repaired specimen.

Figure 4.8 (f) Comparison of hysteretic loops between analysis and experiment for original and repaired specimens.
(No. 6 specimen of Chapter 3, El Centro record A_{max}=200 gal, Repaired with epoxy resin grouting method)

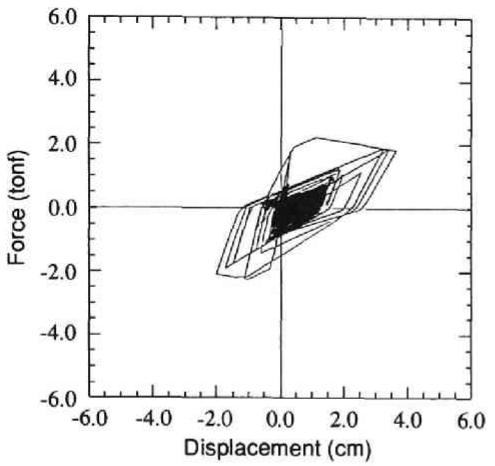

(i) Analytical result for original specimen.

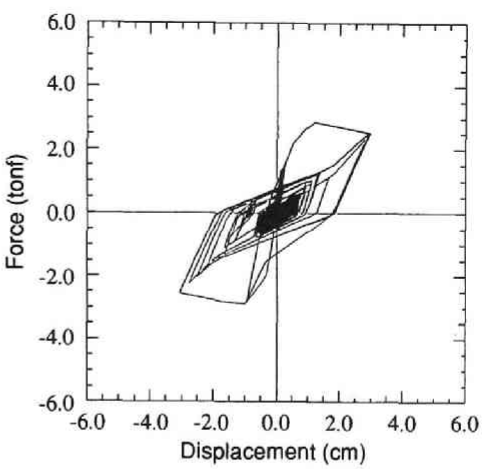

(ii) Analytical result for repaired specimen.

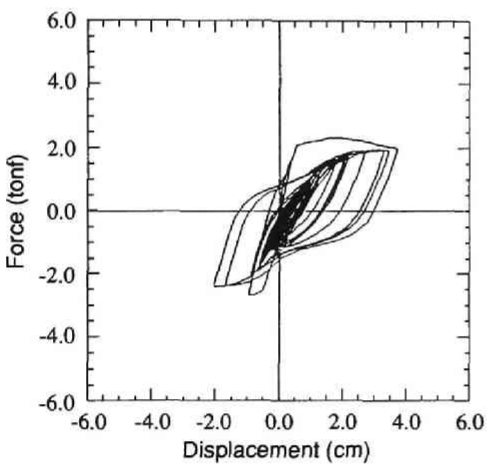

(iii) Experimental result for original specimen.

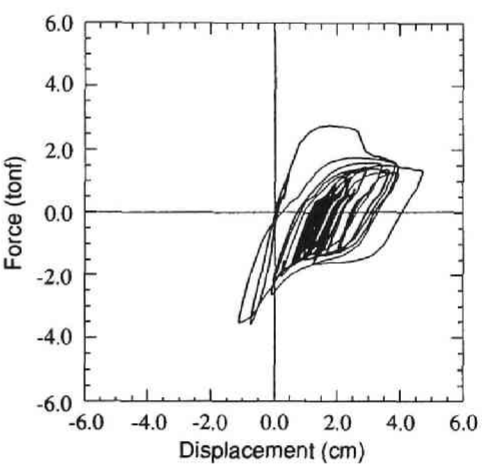

(iv) Experimental result for repaired specimen.

Figure 4.8 (g) Comparison of hysteretic loops between analysis and experiment for original and repaired specimens.
(No. 7 specimen of Chapter 3, El Centro record A_{max}=250 gal, Repaired with epoxy resin grouting method)

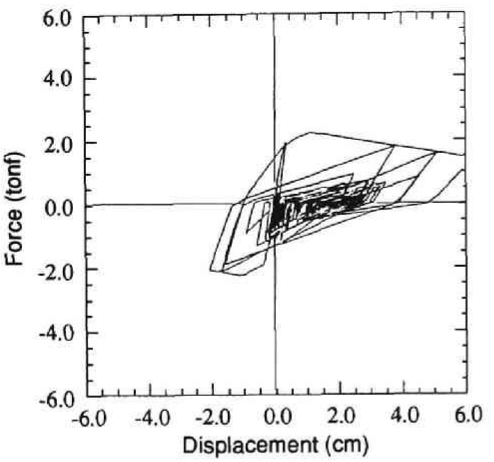

(i) Analytical result for original specimen.

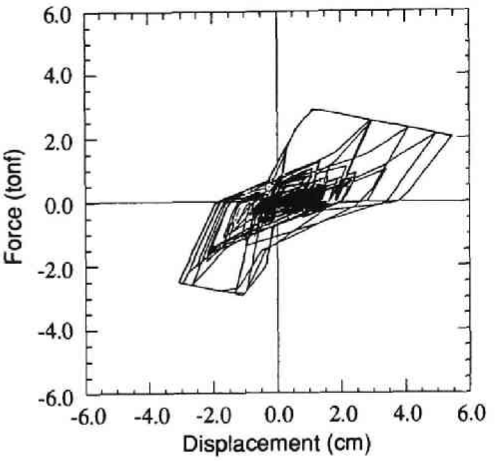

(ii) Analytical result for repaired specimen.

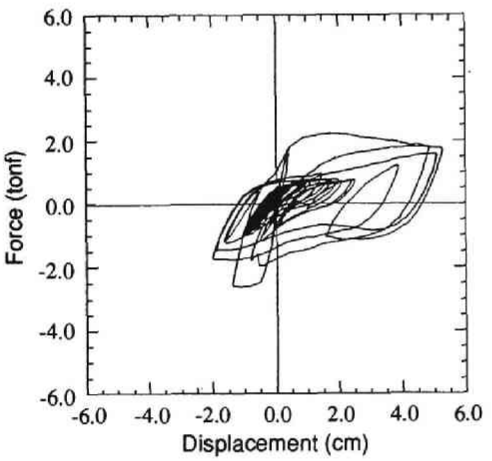

(iii) Experimental result for original specimen.

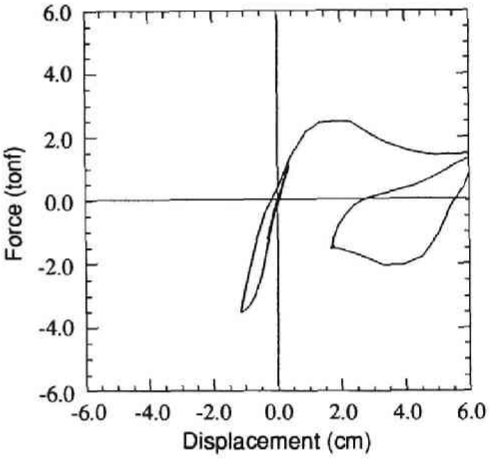

(iv) Experimental result for repaired specimen.

Figure 4.8 (h) Comparison of hysteretic loops between analysis and experiment for original and repaired specimens.
(No. 8 specimen of Chapter 3, El Centro record A_{max}=300 gal, Repaired with epoxy resin grouting method)

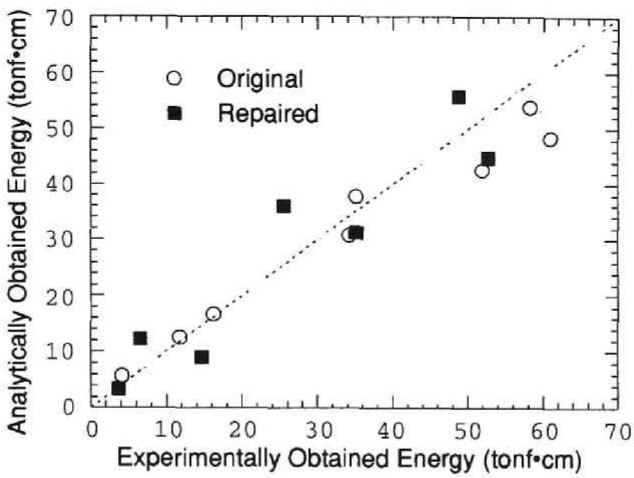

Figure 4.9 Comparison between analytical and experimental absorbed hysteretic energy during experiments.

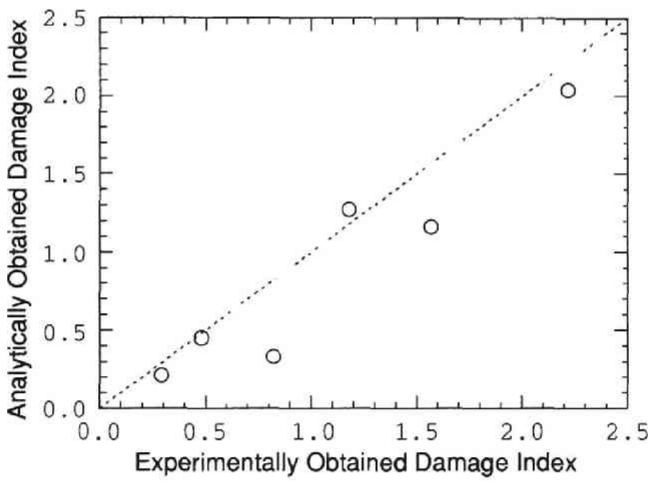

Figure 4.10 Comparison of damage index obtained by analysis and experiments.

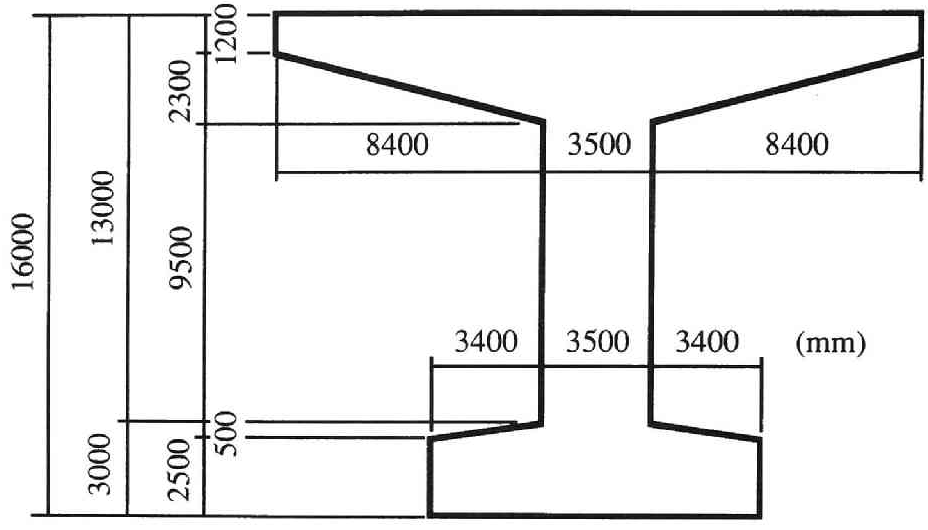

Figure 4.11 T-shape bridge pier model used for the simulations, based on Ref. 12).

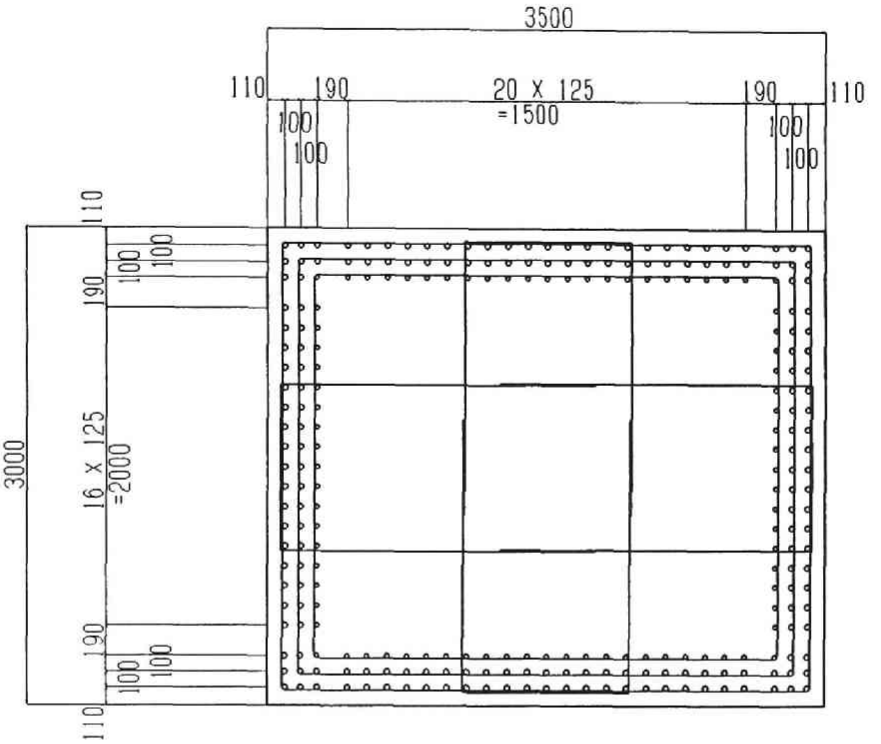

(a) Lower than the point where the reinforcement terminated.

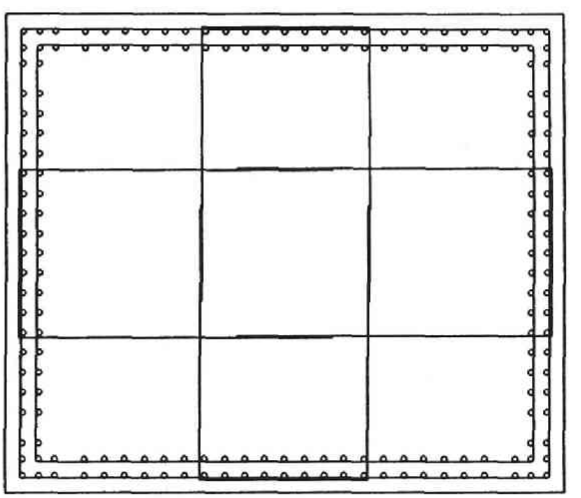

(b) Higher than the point where the reinforcement terminated.

Figure 4.12 Cross sectional views of the RC pier.

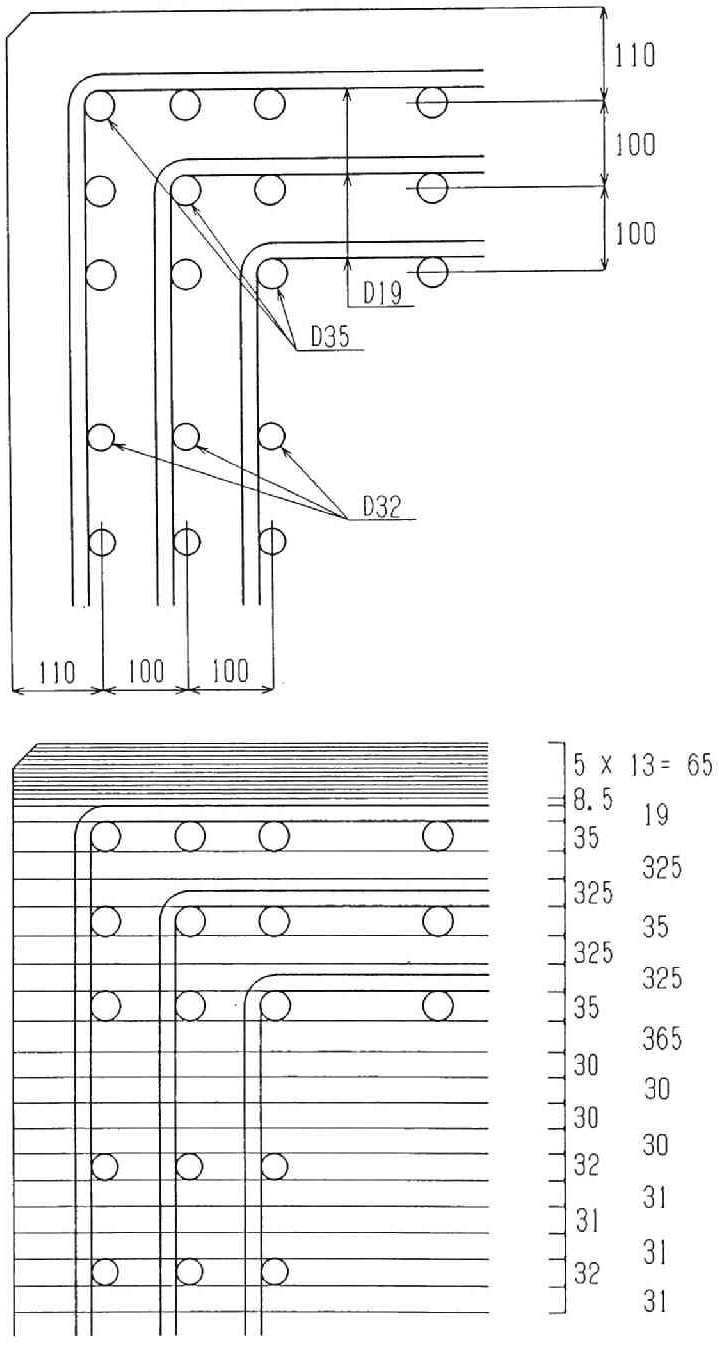

Figure 4.13 (a) Discrete fiber elements for a cross section of the pier below the termination point of the reinforcing bars.

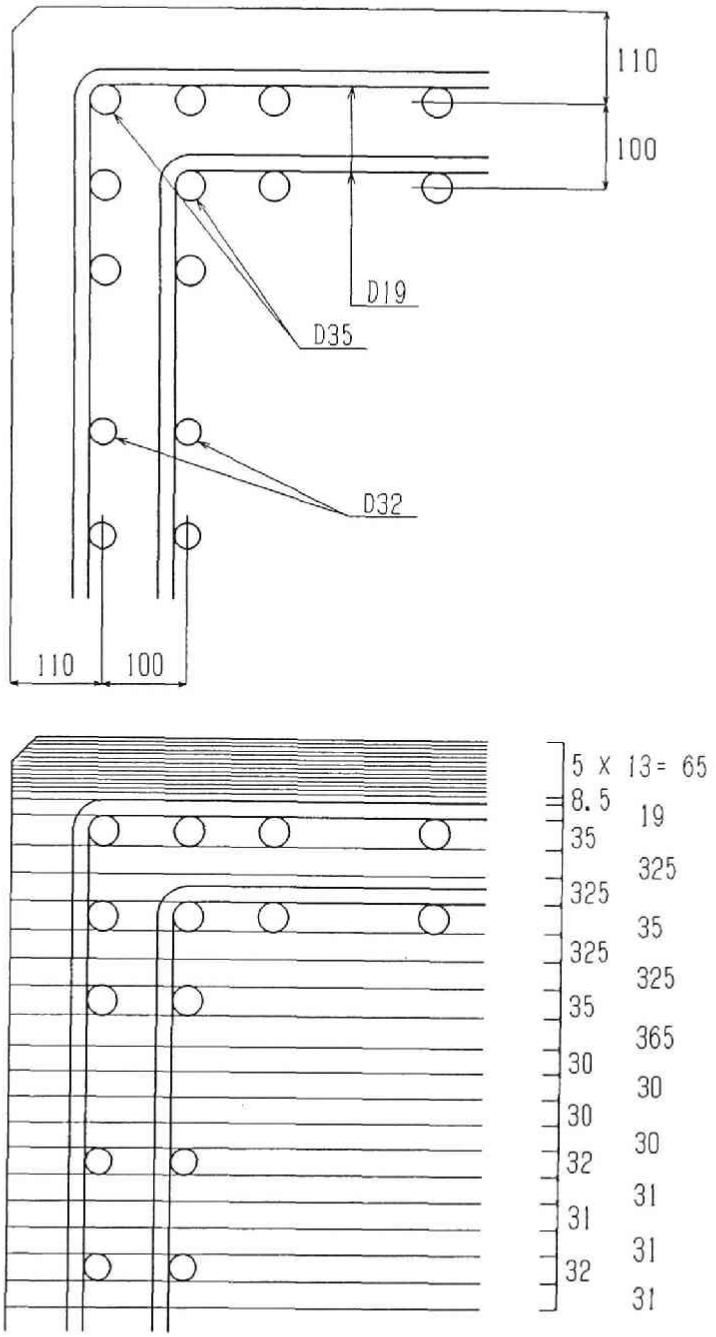

Figure 4.14 (b) Discrete fiber elements for a cross section of the pier above the termination point of the reinforcing bars.

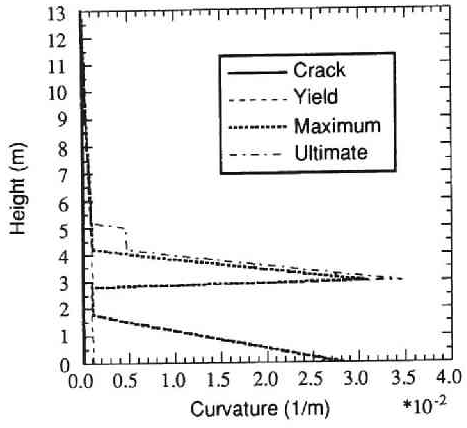

(a) Original

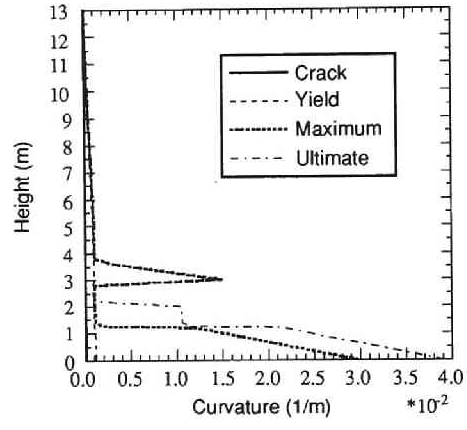

(b) Strengthened with 1 mm steel jackets - case (A)

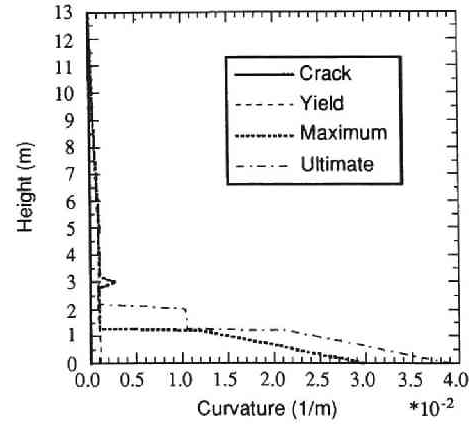

(c) Strengthened with 2 mm steel jackets - case (B)

Figure 4.14 Moment-curvature relation at each section of the bridge piers.

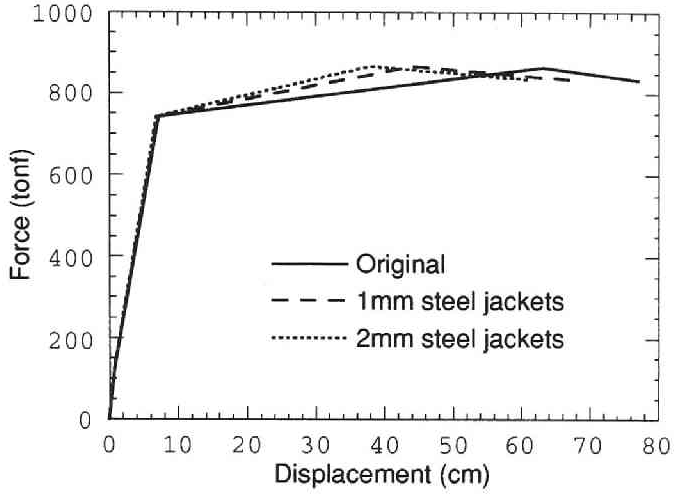

Figure 4.15 Estimated force-displacement relation of original and partially strengthened bridge piers of cases (A) and (B).

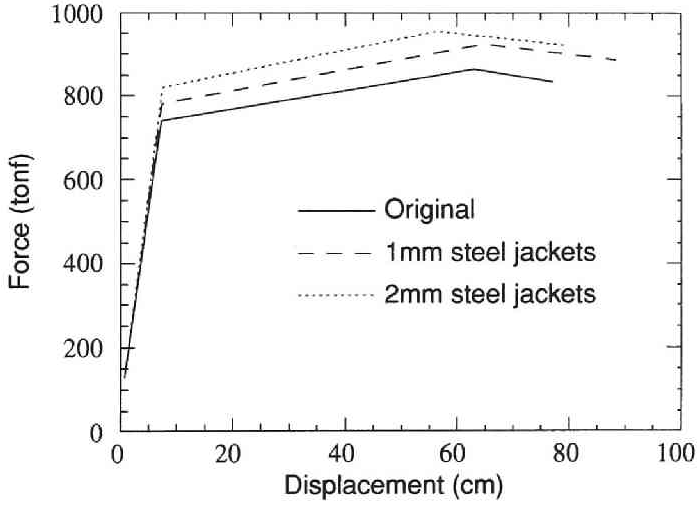

Figure 4.16 Estimated force-displacement relation of original and fully strengthened bridge piers of cases (C) and (D).

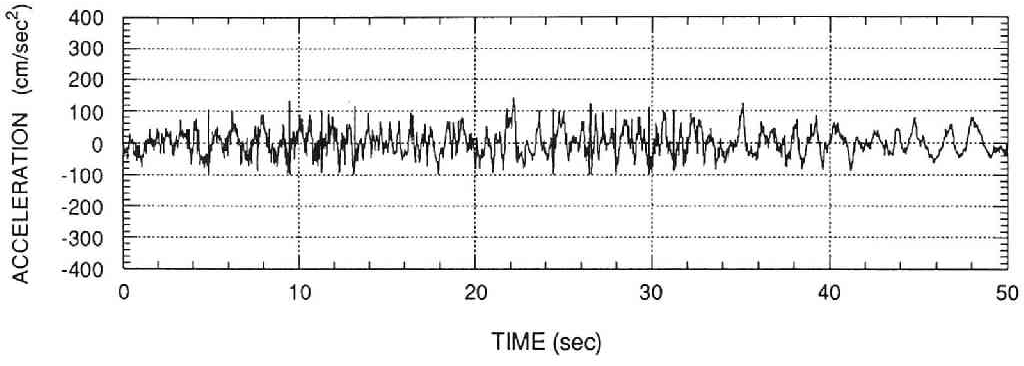

Figure 4.17 Type 3 earthquake record based on Ref. 13.

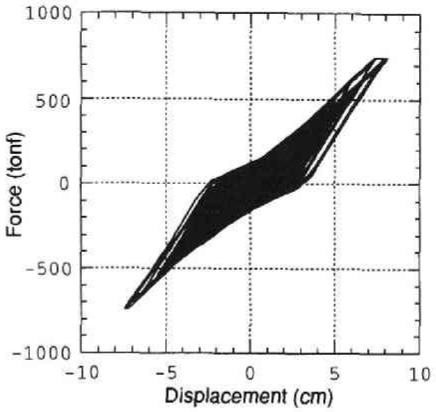

(a) Original

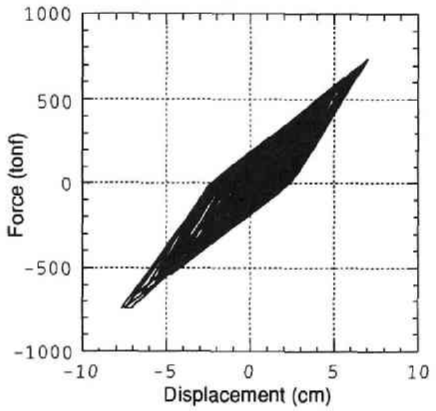

(b) Strengthened with 1 mm steel jackets

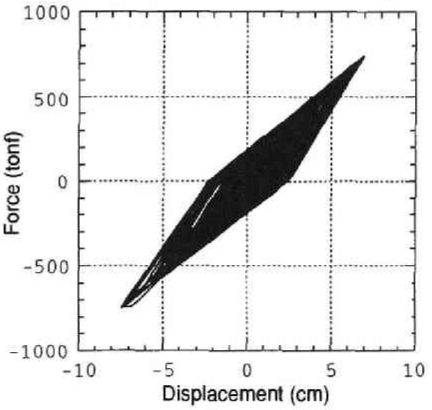

(c) Strengthened with 2 mm steel jackets

Figure 4.18 Simulated hysteretic responses of original and strengthened bridge piers.

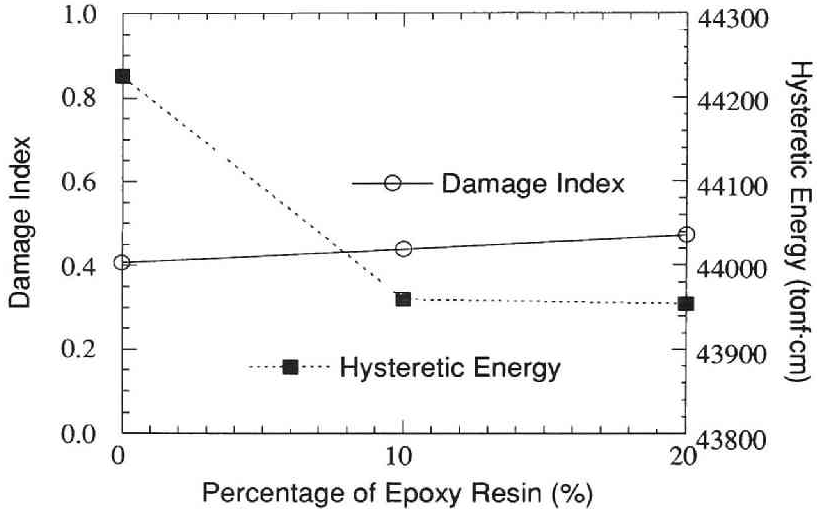

Figure 4.19 Damage index and absorbed hysteretic energy according to amount of epoxy resin.

5. Nonlinear Earthquake Response of a RC Bridge Pier Retrofitted with HDR Seismic Isolator

5.1 General Remarks

In this chapter, study of the earthquake response of a RC bridge pier retrofitted with a seismic isolator was conducted using a more sophisticated hybrid experimental system than the one shown in Chapter 3. The results were then compared with the analytical response of the original non-isolated pier. Among many types of seismic isolators, a high-damping rubber (HDR) bearing (**Photo 5.1**) was used in this study.

5.2 Nonlinear Substructured Hybrid Testing Procedure

The cross section of the HDR bearing used was 250 mm square, which is shown in **Figure 5.1**. It consisted of four layers of 12 mm rubber with 1 mm steel plates inserted between the rubber layers. The basic dynamic properties of this HDR isolator were tested in the previous studies [1-4].

The test set-up is shown in **Figure 5.2** and **Photo 5.2**. Three actuators were used in this system. The HDR bearing was subjected to 40 tonf of axial force generated by two vertical actuators (maximum total capacity = 80 tonf). In addition, the two vertical actuators were controlled so as to keep the loading beam in horizontal position throughout the large range of applied horizontal displacements. Then, calculated earthquake displacement response was applied laterally (**Photos 5.3** and **5.4**) by one horizontal actuator controlled with a 32-bit personal computer shown in **Photo 5.5**. This system has capability to conduct 3-d.o.f. general in-plane loading in which a specimen is subjected to combined axial, shear, and bending loads [4].

The equation of motion of general m.d.o.f. system to solve is as follows.

$$[\mathbf{M}]\{\ddot{\mathbf{x}}(t)\} + [\mathbf{C}]\{\dot{\mathbf{x}}(t)\} + \{\mathbf{F}(t)\} = -[\mathbf{M}]\{\mathbf{1}\}\{\ddot{\mathbf{z}}(t)\} \tag{5.1}$$

in which, $[\mathbf{M}]$ is the mass matrix, $[\mathbf{C}]$ is the damping matrix, $\{\mathbf{F}(t)\}$ is the

restoring force vector, {**1**} is the column of ones and zeros, $\ddot{z}(t)$ is the ground acceleration at time t and $\{\mathbf{x}(t)\}$ is the relative displacement vector at time t. The substructured hybrid experiment gets the restoring force $\{\mathbf{F}(t)\}$ from both the loaded specimen and the numerical calculation. The total restoring force vector is composed as follows.

$$\{\mathbf{F}(t)\} = \{\mathbf{F}(t)\}^{\text{math}} + \{\mathbf{F}(t)\}^{\text{experiment}} \tag{5.2}$$

The deformation at the next time step can be then obtained from the central difference method as shown in the next equation.

$$\{\mathbf{x}(t+\Delta t)\} = \frac{-[\mathbf{M}]\{\mathbf{1}\}\{\ddot{\mathbf{z}}(t)\} - \{\mathbf{F}(t)\} + \left(\frac{2}{\Delta t^2}[\mathbf{M}]\right)\{\mathbf{x}(t)\} - \left(\frac{1}{\Delta t^2}[\mathbf{M}] - \frac{1}{2\Delta t}[\mathbf{C}]\right)\{\mathbf{x}(t-\Delta t)\}}{\frac{1}{\Delta t^2}[\mathbf{M}] + \frac{1}{2\Delta t}[\mathbf{C}]} \tag{5.3}$$

A T-shape bridge pier of 18 m high shown in **Figure 5.3** was modeled as 1-d.o.f. system which has an inelastic spring and a mass. This pier was designed based on the specification of highway bridge piers [5] and the mass was adjusted in order to realize a structural system with the natural period of interest. Using the assumed force-deformation relation of **Figure 5.4**, the 3-parameter model was used to represent hysteretic behavior of the inelastic spring.

Applying the substructure hybrid testing concepts, the bridge pier was assumed as an analytical substructure while a seismic isolator was assumed as an experimental substructure. **Figure 5.5 (b)** shows the experimental sub-structure of HDR isolator and the bridge pier with an inelastic spring to which the 3-parameter rules were applied. The masses of the model and the number of isolators were determined so that the structure have the first natural period of 2 seconds.

Figure 5.5 (a) describes the non-isolated bridge pier model whose response is calculated by purely analytical methods and compared with the isolated structure. The pier and girder were assumed to move simultaneously for the non-isolated case.

The input motions were prepared using Type 1, Type 2 and Type 3

earthquake records prescribed in the Japanese seismic code for highway bridges [6] (**Figure 5.6**). Their maximum accelerations were set to 60 gal, 90 gal and 120 gal, which corresponds the maximum displacement of HDR bearing to about 100%, 150% and 200% of its total height of the rubber (48 mm). Nine cases of experiments were conducted by changing the input motions as shown in **Table 5.1**. Designation of each case consists of the earthquake type number and its maximum acceleration.

5.3 Response of Isolated and Non-Isolated Bridge Pier

5.3.1 Acceleration Time Histories

Figures 5.7 (a)-(i) show the obtained acceleration response for isolated and non-isolated bridge piers. Each figure contains absolute acceleration time histories of (1) non-isolated pier-girder, (2) isolated bridge pier top, and (3) isolator itself. The results of (1) was obtained purely analytically while (2) and (3) were obtained from the hybrid experiments.

The natural period of the non-isolated structure is 0.46 second which dominates the acceleration response shown in the most upper figures. On the other hand, the first natural period of the isolated structure is 2.0 second which dominates the response of the isolator, and the second natural period is 0.14 second which is dominant in the response of the isolated bridge pier.

The acceleration response of the isolated pier top (below the isolator) was higher than the non-isolated pier. On the contrary, the girder response became smaller resulting from its elongated natural period. Numerical comparison between non-isolated and isolated structures are discussed later.

5.3.2 Hysteretic Load-Deformation Response

Figures 5.8 (a)-(i) show the hysteretic response for isolated and non-isolated structures. Similar to the previous figures, each figure contains hysteretic response for (1) non-isolated pier-girder, (2) isolated bridge pier top, and (3) isolator itself.

The non-isolated pier-girder response showed nonlinear hysteretic behavior which absorbed large hysteretic energy. Although the loops were

stable in the numerical simulations, a real structure has a possibility to behave unstable for many cyclic loadings because no failure criteria had been considered in this analysis.

The isolated pier top shows almost linear response except for the Case 1-120; the input motion of it was Type 1 earthquake whose maximum acceleration was set to 120 gal (**Figure 5.8-c-2**). Unless the input was strong and of high frequency accelerations, a linear hysteretic model for the isolated bridge pier may accurately estimate the response of the pier. Even for Case 1-120, a large inelastic response occurred only once.

The isolator showed bilinear shape hysteretic loops. However, severe material hardening was observed for the strong motions such as Cases 1-120 (**Figure 5.8-c**), 2-120 (**Figure 5.8-f**) and 3-120 (**Figure 5.8-i**). Lateral deformation larger than 150% of its total rubber height triggered the hardening phenomenon for this HDR specimen.

5.3.3 Comparison of Isolated and Non-Isolated Structures

Figure 5.9 shows the comparison of the maximum acceleration response for non-isolated and isolated structures. The isolated girder showed 50-70% acceleration response of the non-isolated structure except for Cases 1-90 and 1-120 which responded 80-90% of the non-isolated one. Material hardening initiated early in the response caused the less reduction of acceleration response.

The acceleration response of the isolated pier top was higher than the non-isolated pier as already mentioned. This was caused by the linear response of the isolated pier while the non-isolated pier showed nonlinear hysteretic behavior. To verify this point, the maximum acceleration of a linear non-isolated pier was also plotted in this **Figure 5.9**. The maximum acceleration of the isolated pier always became smaller about 70-95% of the linear non-isolated pier.

Figure 5.10 shows the comparison of the maximum base shear coefficients between the non-isolated and the isolated piers. The isolated pier showed 75-85% base shear force of the non-isolated pier for Case 1-90 and Case 1-120, and 50-60% for the other cases. This represents the effectiveness of the HDR isolators for retrofitting old structures.

The maximum displacement response of the girder is shown in **Figure 5.11**. The displacement response of the isolated girder became more than 6 times larger than the non-isolated original structure. Cautious countermeasures are needed for preventing collapse and fall of the girders.

Figure 5.12 compares ductility factors of the pier (below isolators) between non-isolated and isolated structures. The ductility factor of the isolated bridge pier became 40-50% of the non-isolated pier except for Case 1-120. Case 1-120 showed only 75% of the non-isolated one, however, only one large deformation was observed from **Figure 5.8 (c)-2**. The ductility factors for the pier of the isolated structures were less than 0.2 (except for Case 1-120) which results in they might suffer only slight damage due to large deformation. On the contrary, the ductility factors for the non-isolated pier showed large values as 0.2-0.5. These simulations resulted in safe responses presented from this point of view.

Figure 5.13 shows comparison of absorbed hysteretic energy during earthquake response between non-isolated and isolated structures. Most of the energy input to the isolated structures was absorbed by the HDR isolator, as can be recognized from the linear response of the pier. The absorbed energy of the isolated structure was only 6-25% of the non-isolated original structure. The advantage of the isolated structures were clearly presented in this point of view.

Lastly, **Figure 5.14** shows the damage index [7] of the non-isolated and isolated piers. The damage index consists of the deformation term and the absorbed hysteretic energy term as already mentioned in the previous chapters. Both the displacement response of the pier (**Figure 5.12**) and the absorbed energy (**Figure 5.13**) were smaller than the non-isolated pier, which results in the damage index of the isolated pier to be at most 0.05. The damage indices for the non-isolated bridge piers showed 2-15 times larger values than the isolated piers. The differences mainly owed to the absorbed energy term.

5.4 Adding Seismic Isolator to Slightly Damaged Pier

This section verifies effectiveness of seismic isolators for retrofitting already slightly damaged RC piers. When the bridge is retrofitted by adding seismic isolators, the severely damaged parts of the bridge pier might be rehabilitated. However, the slightly damaged parts might be left unrepaired, or

the severely damaged material may not behave quite similarly to the brand new material even after retrofitting. It is important to check the behavior of isolators under imperfect condition of bridge piers.

After the simulations using weak input motions, same as Cases 1-60, 2-60 and 3-60 of the previous section, isolators were assumed to put on the damaged piers for retrofitting. Degraded stiffness and strength after the first loading were used for the second loading simulation. Dissipated energy and the past maximum deformation during the first loading were also saved and used for the second loading. The first loading using weak acceleration is called "pre-loading" in this study.

The model became slightly damaged after this pre-loading simulation as to ductility factor of 0.2 (**Figure 5.12**) and the damage index of 0.03-0.05 (**Figure 5.14**).

Then, the experimental results for the second loading; i.e., the response of the isolated damaged structure, was compared with the first loading case of the isolated new structure which had been shown in the previous section. The results were also compared with the analytical simulations of the second loadings without retrofit.

The second loading using a strong acceleration is called "main loading" in this section. The loading schemes for simulations and experiments are described in **Table 5.2**. The designation of each loading scheme consists of the earthquake type number and loading series name. The "A-series" loadings represent the behavior of the isolated structure whose pier has suffered slight damage. The "B-series" loadings represent the behavior of initially loaded isolated structure. The "C-series" loadings represent the response of already damaged structure without any retrofit. And the "D-series" loadings represent the response of a new structure subjected to 120 gal acceleration. The simulations of the isolated structures were carried out using hybrid experiments while the non-isolated cases were calculated purely numerical methods.

Figure 5.15 shows the obtained hysteretic response for the pre-loadings and the main loadings with and without isolators. No effect of pre-loadings can be observed on the hysteretic loops of the added isolators during the main loadings. Comparing the isolator response between Cases 1-A (**Figure 5.15-a-3**) and 1-B (**Figure 5.15-b-2**), 2-A (**Figure 5.15-e-3**) and 2-B (**Figure 5.15-f-2**), 3-A (**Figure 5.15-i-3**) and 3-B (**Figure 5.15-j-2**), no significant difference can be observed.

The damaged piers also show the similar loops to the non-damaged ones, however, the initial stiffness had been changed. Effect of different initial stiffness was obvious especially for the isolated piers because of their almost linear responses: for example, see **Figure 5.15-e-2** of Case 2-A and **Figure 5.15-f-1** of Case 2-B, or **Figure 5.15-i-2** of Case 3-A and **Figure 5.15-j-1** of Case 3-B. On the contrary, the response of the pre-loaded pier showed no difference from the initially loaded pier: see **Figure 5.15-c-2** of Case 1-C and **Figure 5.15-d** of Case 1-D, **Figure 5.15-g-2** of Case 2-C and **Figure 5.15-h** of Case 2-D, or **Figure 5.15-k-2** of Case 3-C and **Figure 5.15-l** of Case 3-D.

Figures 5.16-5.21 show the response characteristics of each loading scheme.

First, **Figure 5.16** shows the maximum acceleration responses of the piers and girders. The maximum acceleration did not changed for the non-isolated cases: Cases 1-C and 1-D, 2-C and 2-D, 2-C and 3-D. The pre-loaded isolated piers (Cases 1-A, 2-A and 3-A) showed lower acceleration responses because of their softer stiffnesses compared to the initially loaded isolated piers (Cases 1-B, 2-B and 3-B), however, they are still higher than the non-isolated piers. The pre-loaded girders which had been retrofitted with isolators also showed 1-10% lower acceleration responses compared to the initially loaded isolated girders. The isolators reduced the maximum girder acceleration responses in 20-50% compared with the non-isolated structures.

Figure 5.17 shows the base shear coefficient for each loading scheme. The pre-loaded structures which had been retrofitted with isolators (Cases 1-A, 2-A and 3-A) showed the same or a little less base shear coefficients compared to the initially loaded isolated structures (Cases 1-B, 2-B and 3-B) like the maximum acceleration response.

Figure 5.18 shows the maximum displacement response of the girders for each loading scheme. the pre-loaded girders showed larger displacement response for the Type 1 and the Type 3 earthquakes, and smaller response for the Type 2 earthquake, however, the differences were within only 5%. The responses of the pre-loaded girders without isolators (Case 1-C, 2-C and 3-C) were as same as the initially loaded girders without isolators of Cases 1-D, 2-D and 3-D.

Figure 5.19 shows the ductility factors for the piers. The pre-loaded piers

showed larger ductility factors for Cases 1-C and 3-A, smaller value for Case 1-A, and the same values for the other cases. For Cases 1-A and 1-B, the ductility factors were determined by the only one impulsive response shown in **Figures 5.15 (a)-2** and **5.15 (b)-1**. The difference between the maximum displacement responses of these two piers were only 0.1 mm. Therefore, the ductility factors of the pre-loaded structures can be stated as almost the same or a little larger compared to the initially loaded structures. Elongation of the natural period due to pre-loadings affected their displacement responses of the piers.

Figure 5.20 shows the absorbed hysteretic energy during earthquakes. For the isolated structures, the total absorbed energy became almost the same comparing between pre-loaded and initially loaded structures: i.e., total amount of energy that was absorbed during pre-loading and the main loading of 1-A, 2-A and 3-A were as same as that of the main loading of 1-B, 2-B and 3-B. The energy absorbed by the pre-loaded piers during the main loading became smaller than that of the initially loaded piers. Furthermore, the isolator absorbed the same amount of the hysteretic energy between Cases 1-A and 1-B, 2-A and 2-B, 3-A and 3-B. For the non-isolated structures, the energy absorbed during the main loadings were the same between 1-C and 1-D, 2-C and 2-D, 3-C and 3-D. Therefore, the energy absorbed by the pre-loaded structures in Cases 1-C, 2-C and 3-C always became larger than the initially loaded structures of Cases 1-D, 2-D and 3-D.

Figure 5.21 shows the damage indices for the pre-loadings and the main loadings. The pre-loaded structures always showed larger damage indices mainly because of their larger amount of absorbed energy. Though the added isolators after pre-loading behaved similarly to the initially loaded structures, the slightly damaged piers did not respond in the similar way as the original piers.

5.5 Conclusions

Effectiveness of a seismic isolator in retrofitting a RC bridge pier was studied using hybrid experimental system and numerical simulations. The main conclusions were as follows.

(1) The HDR isolator behaved like a bilinear response. And the isolated pier showed almost linear response while the non-isolated pier showed inelastic cyclic behavior. The isolated bridge pier can be accurately

modeled using linear hysteretic model.

(2) The isolated girder showed 50-70% acceleration response of the non-isolated structure for Type 2 and Type 3 earthquake, and 80-90% for Type 1 earthquake.

(3) The maximum acceleration response of the isolated pier top was higher than the non-isolated original pier because of its almost linear response of the isolated pier, however, it is smaller than the simulation results of the linear non-isolated pier.

(4) The maximum base shear decreased for the isolated structures to about 50-85% of the non-isolated structures.

(5) The maximum displacement of the isolated girders became more than 6 times larger than the non-isolated girders. On the contrary, the ductility factors for the isolated pier decreased to 40-50%.

(6) The absorbed hysteretic energy of the isolated structure was 6-25% of the non-isolated originals.

(7) The isolated structures showed small damage indices at most 0.43, while the damage index of the non-isolated original structure exceeds 1.0 sometimes.

(8) The first loadings without isolators using weak input motions did not affect on the responses of the isolators under second loadings using strong input motions. However, elongated natural period of the pre-loaded piers affected the response of the piers themselves.

References of Chapter 5

1) Yamada, Y., Iemura, H., Tanzo, W., Uno, Y. and Nakamura, S., "Hybrid loading test of the high damping rubber bearings subjected to sinusoidal and random earthquake ground motion", *Journal of Structural Engineering*, Vol. 37A, pp. 851-862, 1991 (in Japanese).
2) Iemura, H., Yamada, Y., Tanzo, W., Uno, Y. and Nakamura, S., "On-line earthquake response tests of high-damping rubber bearings for seismic isolation", *Proc. of the 1st US-Japan Workshop on Earthquake Protective Systems for Bridges*, Buffalo, New York, USA, 1991.
3) Tanzo, W., Yamada, Y., Uno, Y. and Nakamura, S., "Substructured hybrid loading tests of high-damping rubber seismic isolators for inelastic earthquake response of bridge structures", *Proc. of the 10th World Conference on Earthquake Engineering*, Madrid, Spain, Vol. 4, pp. 2233-2236, 1992.
4) Tanzo, W., Yamada, Y. and Iemura, H., *Substructured Computer-Actuator Hybrid Loading Tests for Inelastic Earthquake Response of Structures*, Research Report, School of Civil Engineering, Kyoto University, No. 92-ST-01, 1992.
5) Hanshin Highway Public Corporation, *General Figures for Reinforced concrete Structures*, 1991.
6) Japan Road Association, *Seismic Design Code, Specifications for Highway Bridges in Japan*, Part V, 1990 (in Japanese).
7) Park, Y.J., Ang, A.H.-S. and Wen, Y.K., "Seismic Damage Analysis and Damage-Limiting Design of RC Buildings", *Research Report, University of Illinois*, No. 516, October 1984.

Table 5.1 Designation of loading cases.

Max. Acc. / Earthquake	60 gal	90 gal	120 gal
Type 1	1–60	1–90	1–120
Type 2	2–60	2–90	2–120
Type 3	3–60	3–90	3–120

Table 5.2 Loading schemes to evaluate effect of pre-loadings.

input / name	pre-loading		main loading	
	input motion	isolation	input motion	isolation
1-A	Type 1 max. 60 gal	No	Type 1 max. 120 gal	**Yes**
1-B	—	—	Type 1 max. 120 gal	**Yes**
1-C	Type 1 max. 60 gal	No	Type 1 max. 120 gal	No
1-D	—	—	Type 1 max. 120 gal	No
2-A	Type 2 max. 60 gal	No	Type 2 max. 120 gal	**Yes**
2-B	—	—	Type 2 max. 120 gal	**Yes**
2-C	Type 2 max. 60 gal	No	Type 2 max. 120 gal	No
2-D	—	—	Type 2 max. 120 gal	No
3-A	Type 3 max. 60 gal	No	Type 3 max. 120 gal	**Yes**
3-B	—	—	Type 3 max. 120 gal	**Yes**
3-C	Type 3 max. 60 gal	No	Type 3 max. 120 gal	No
3-D	—	—	Type 3 max. 120 gal	No

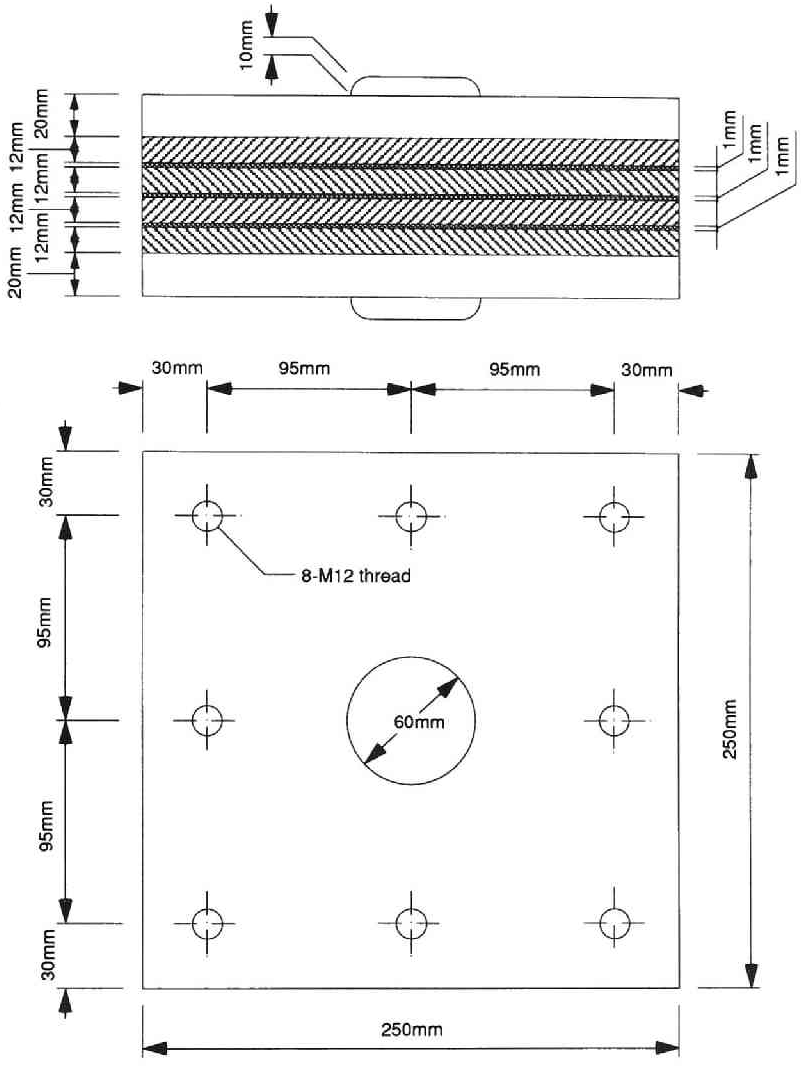

Figure 5.1 Dimension of HDR seismic isolator specimen.

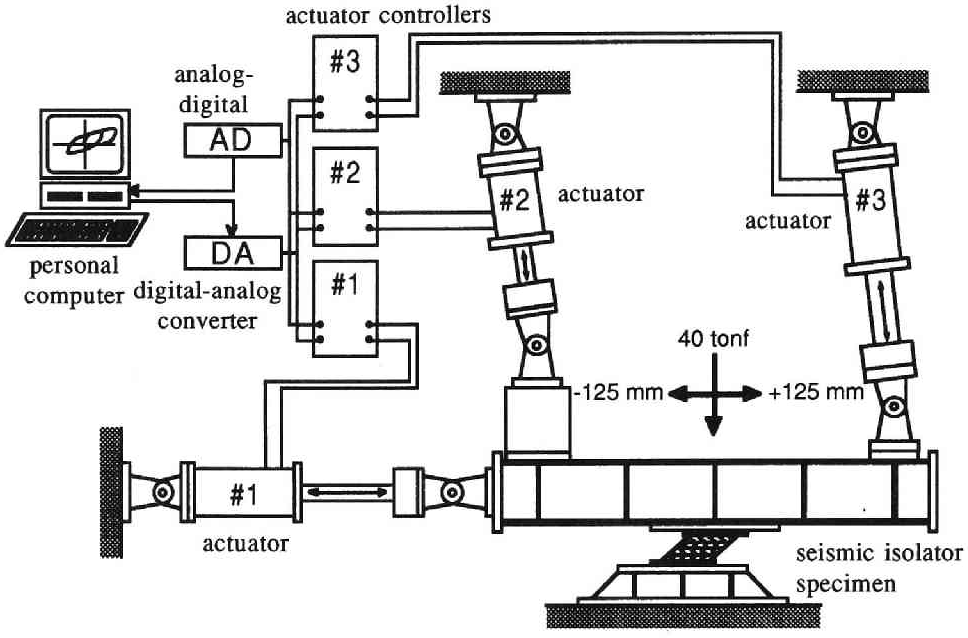

Figure 5.2 Hybrid loading system of earthquake response for seismic isolators.

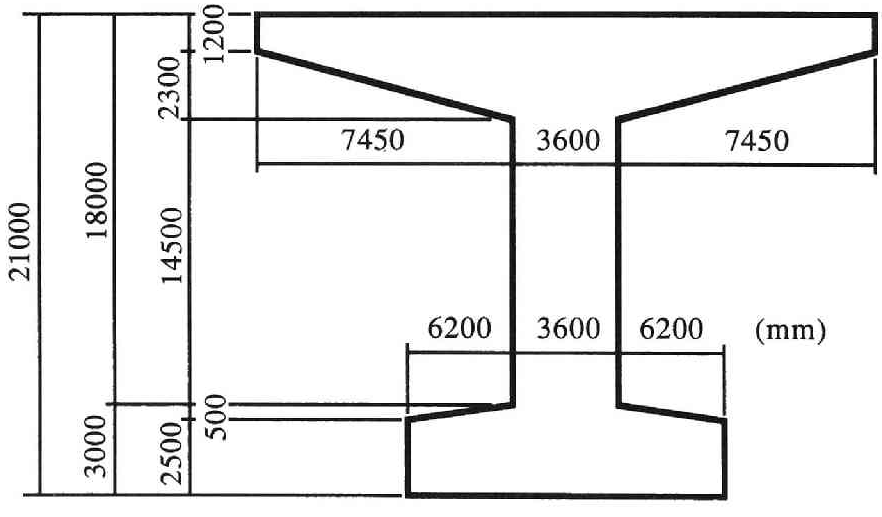

Figure 5.3 T-shape bridge pier model used for retrofit case study.

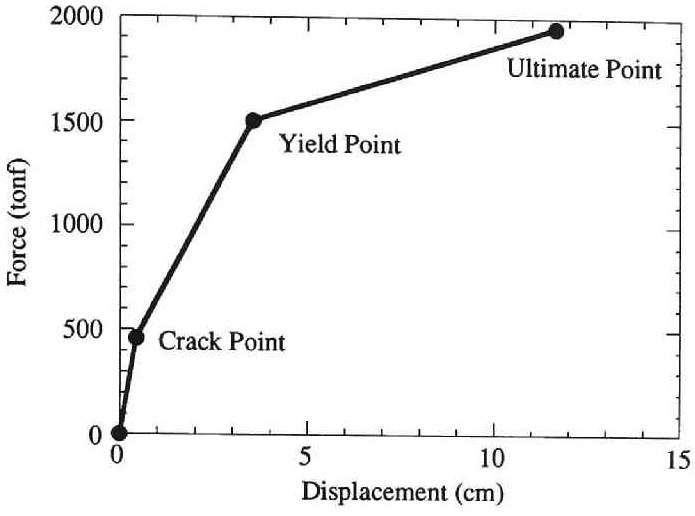

Figure 5.4 Assumed force-deformation relationship for RC pier.

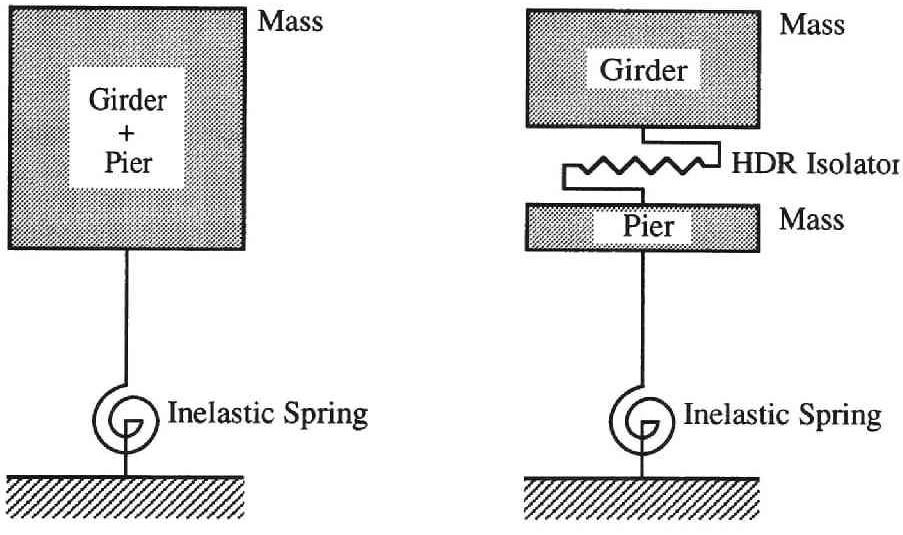

(a) 1-d.o.f. non-isolated model.

(b) 2-d.o.f. isolated model.

Figure 5.5 Bridge pier and girder models used for simulations.

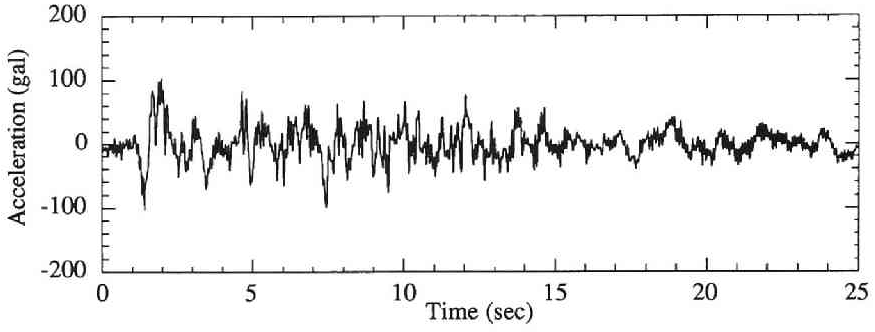

(a) Type 1 eathquake

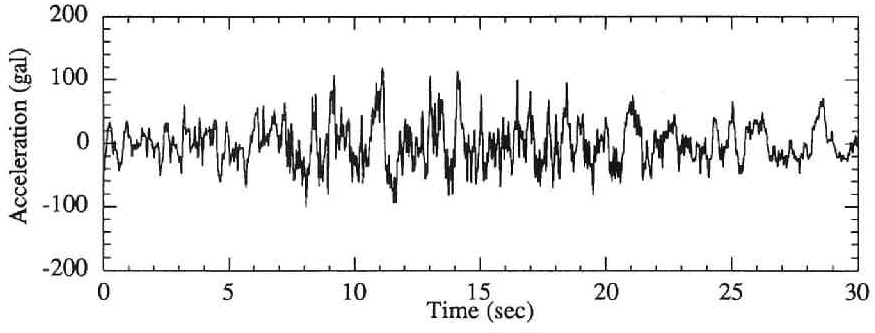

(b) Type 2 eathquake

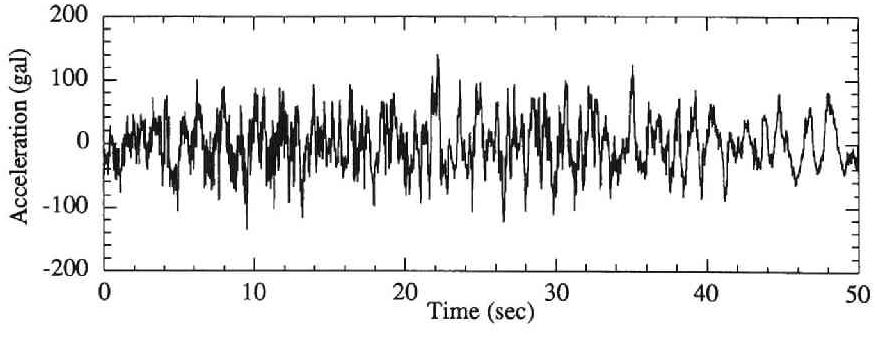

(c) Type 3 eathquake

Figure 5.6 Input earthquake records recommended in the Japanese seismic code for highway bridges.

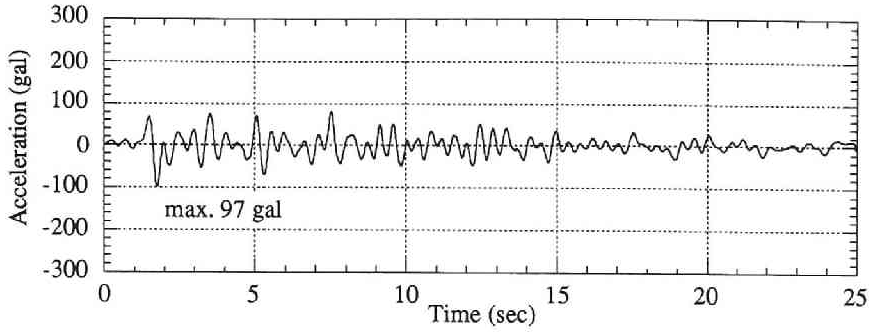

(1) Non-isolated pier-girder acceleration.

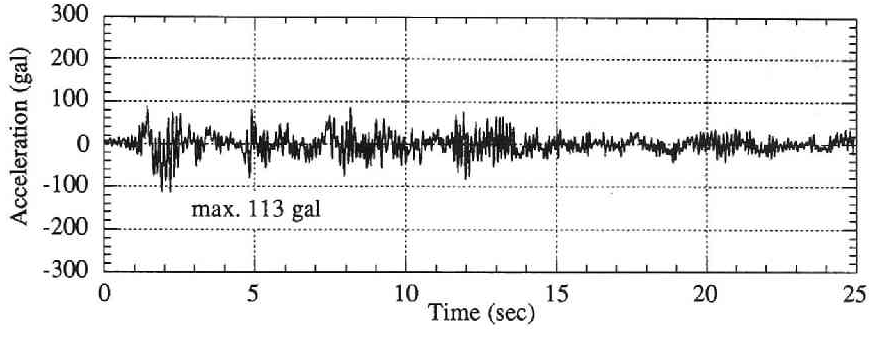

(2) Pier top (below HDR) acceleration of isolated structure.

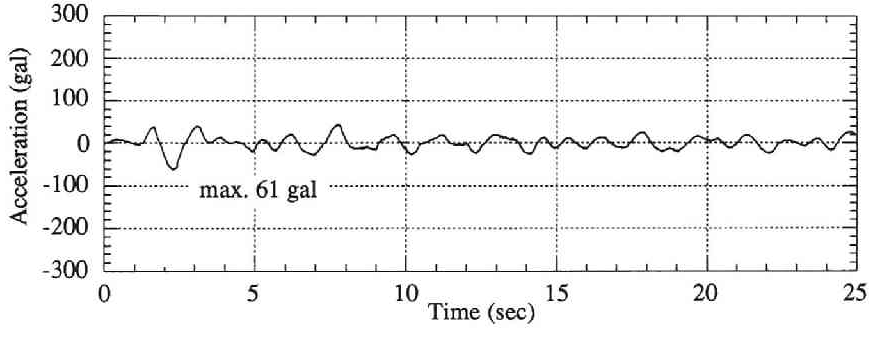

(3) Girder (above HDR) acceleration of isolated structure.

Figure 5.7 (a) Acceleration time histories for Case 1–60.
(Type 1 earthquake, max. 60 gal)

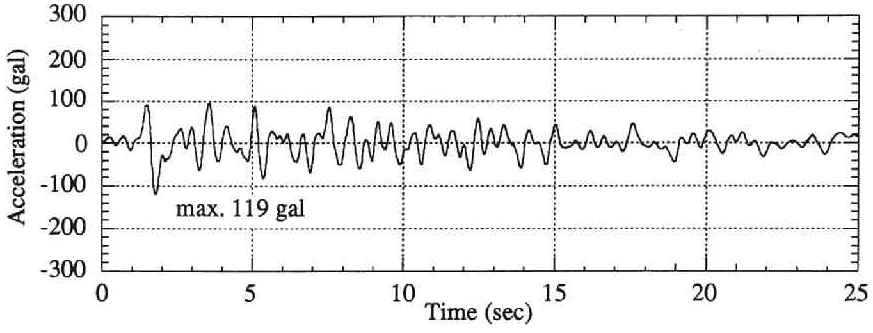

(1) Non-isolated pier-girder acceleration.

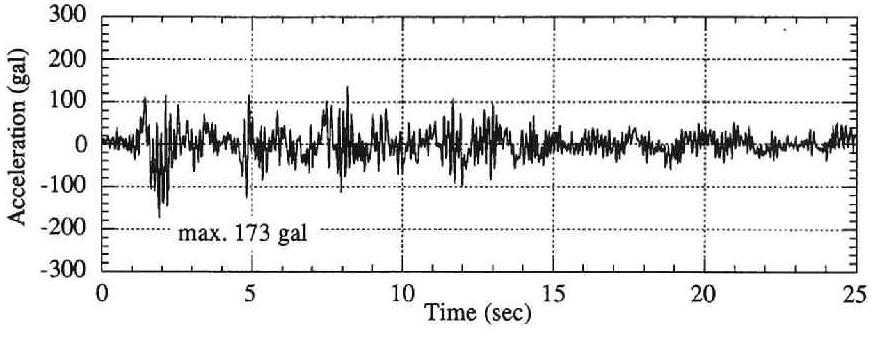

(2) Pier top (below HDR) acceleration of isolated structure.

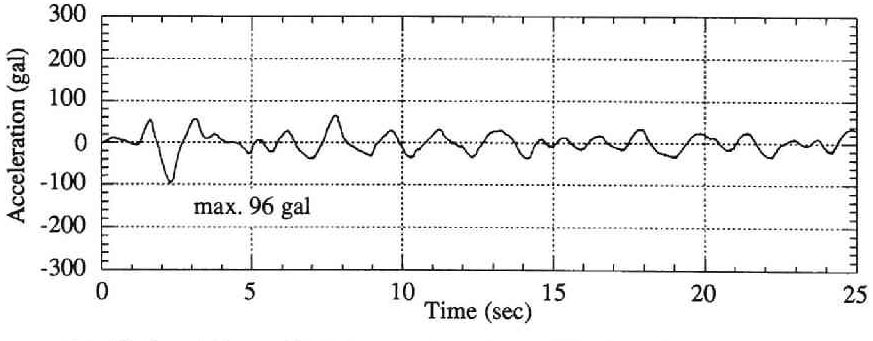

(3) Girder (above HDR) acceleration of isolated structure.

Figure 5.7 (b) Acceleration time histories for Case 1–90.
(Type 1 earthquake, max. 90 gal)

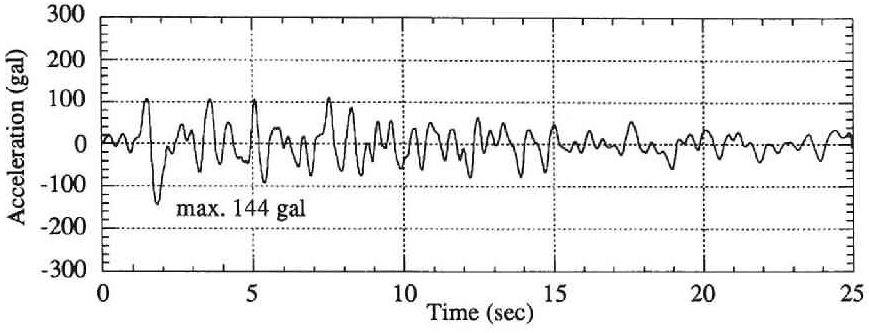

(1) Non-isolated pier-girder acceleration.

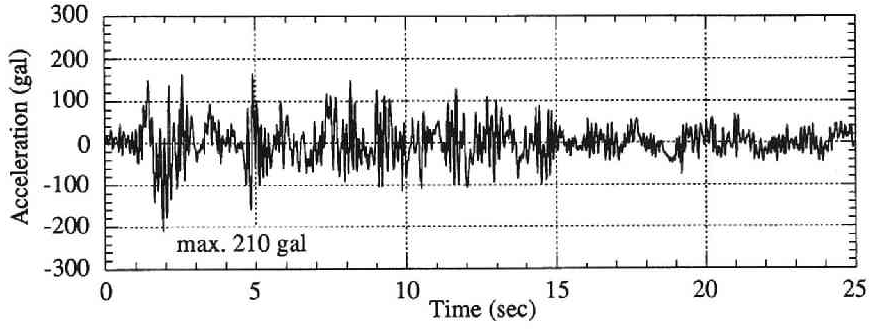

(2) Pier top (below HDR) acceleration of isolated structure.

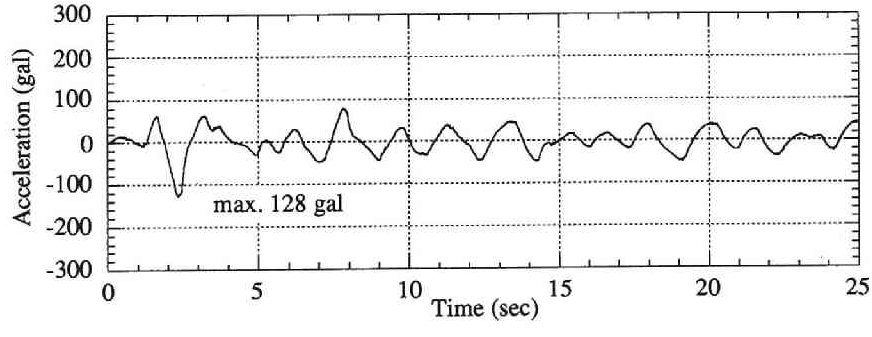

(3) Girder (above HDR) acceleration of isolated structure.

Figure 5.7 (c) Acceleration time histories for Case 1–120.
(Type 1 earthquake, max. 120 gal)

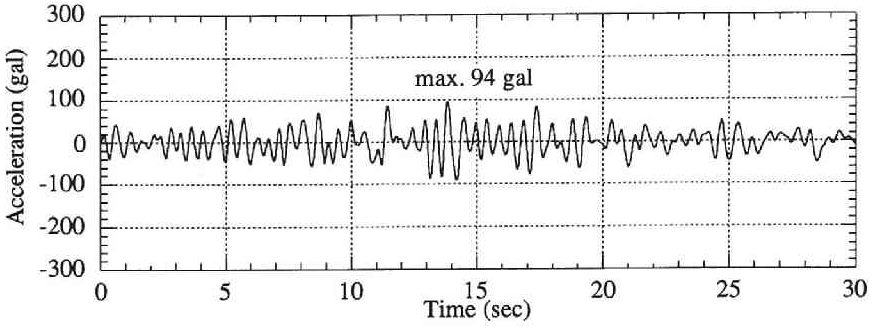

(1) Non-isolated pier-girder acceleration.

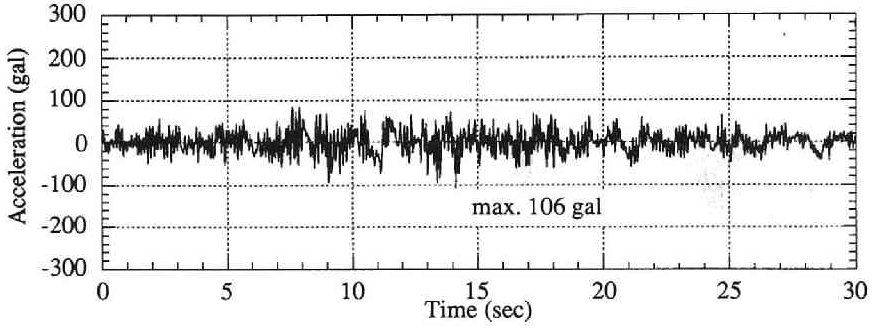

(2) Pier top (below HDR) acceleration of isolated structure.

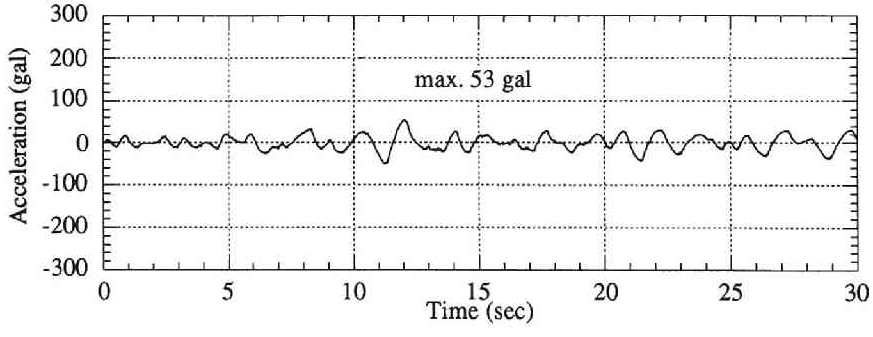

(3) Girder (above HDR) acceleration of isolated structure.

Figure 5.7 (d) Acceleration time histories for Case 2–60.
(Type 2 earthquake, max. 60 gal)

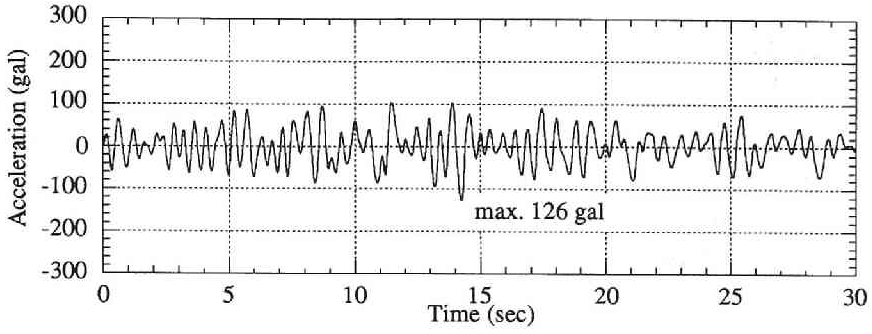

(1) Non-isolated pier-girder acceleration.

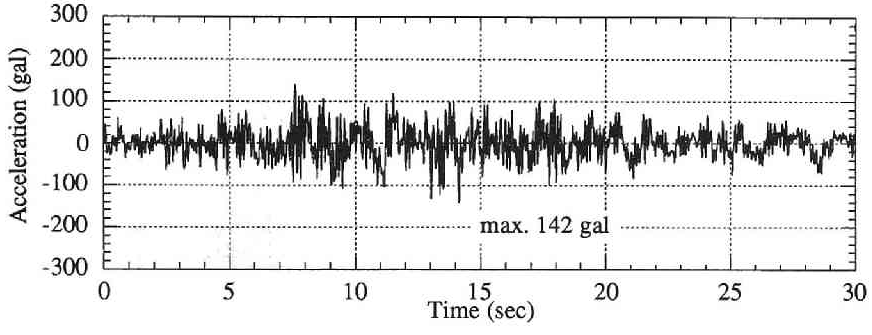

(2) Pier top (below HDR) acceleration of isolated structure.

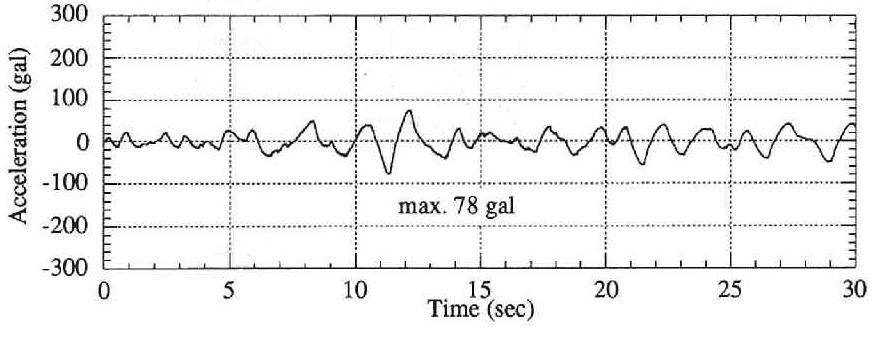

(3) Girder (above HDR) acceleration of isolated structure.

Figure 5.7 (e) Acceleration time histories for Case 2–90.
(Type 2 earthquake, max. 90 gal)

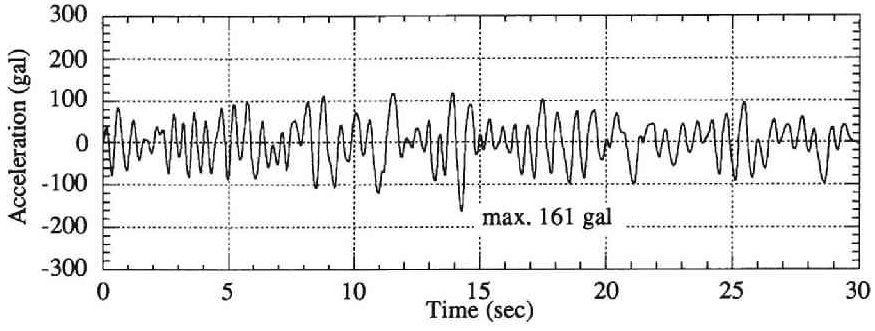

(1) Non-isolated pier-girder acceleration.

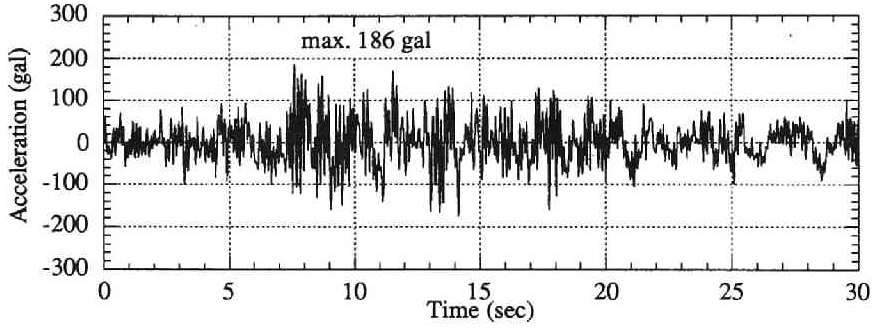

(2) Pier top (below HDR) acceleration of isolated structure.

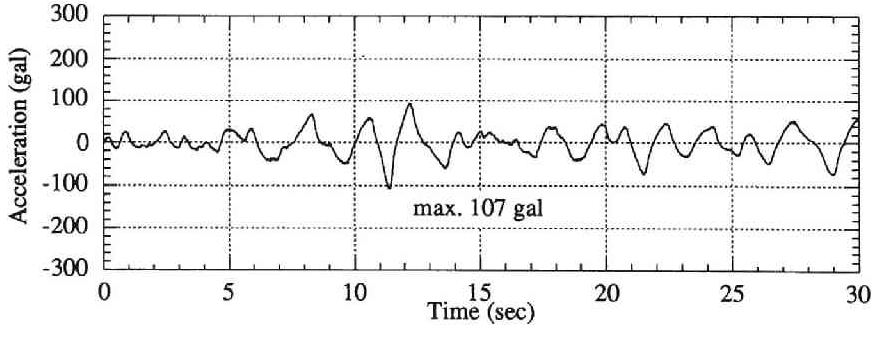

(3) Girder (above HDR) acceleration of isolated structure.

Figure 5.7 (f) Acceleration time histories for Case 2–120.
(Type 2 earthquake, max. 120 gal)

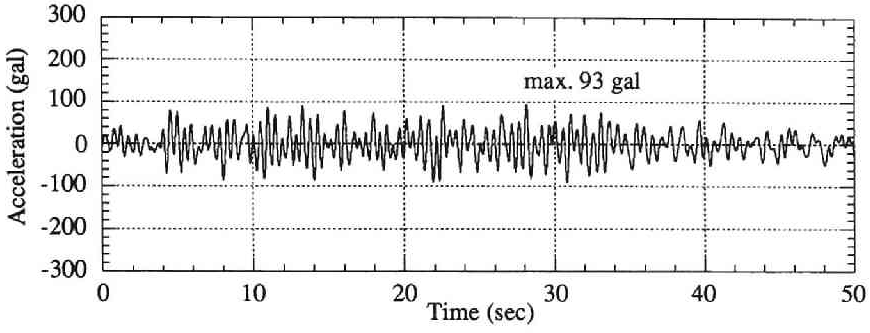

(1) Non-isolated pier-girder acceleration.

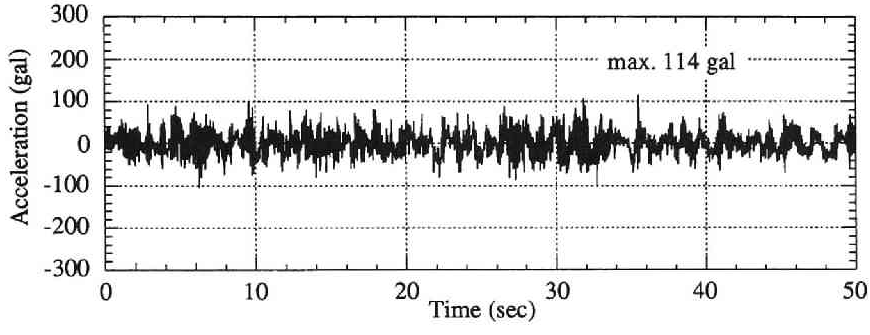

(2) Pier top (below HDR) acceleration of isolated structure.

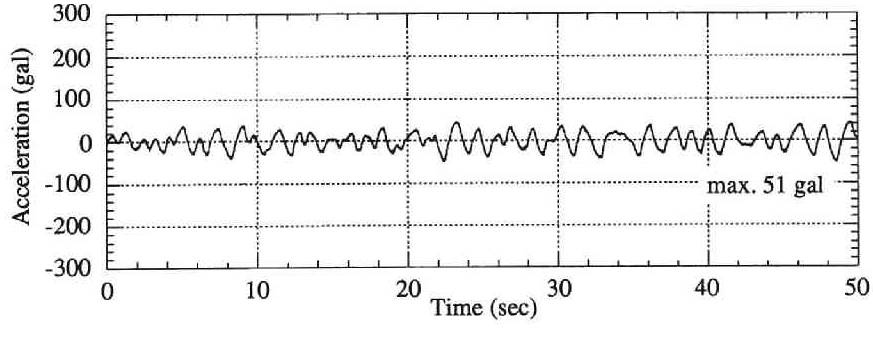

(3) Girder (above HDR) acceleration of isolated structure.

Figure 5.7 (g) Acceleration time histories for Case 3–60.
(Type 3 earthquake, max. 60 gal)

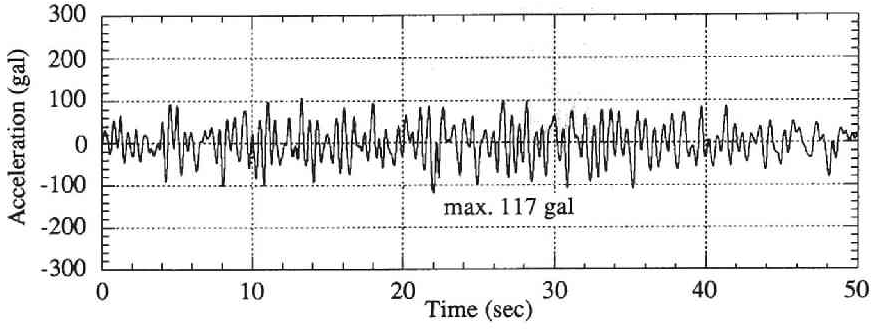

(1) Non-isolated pier-girder acceleration.

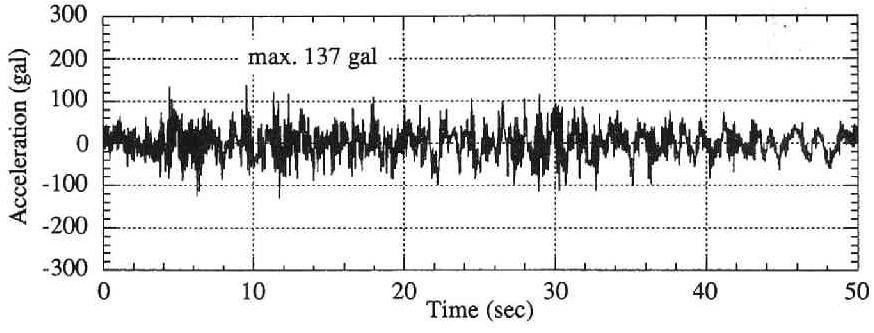

(2) Pier top (below HDR) acceleration of isolated structure.

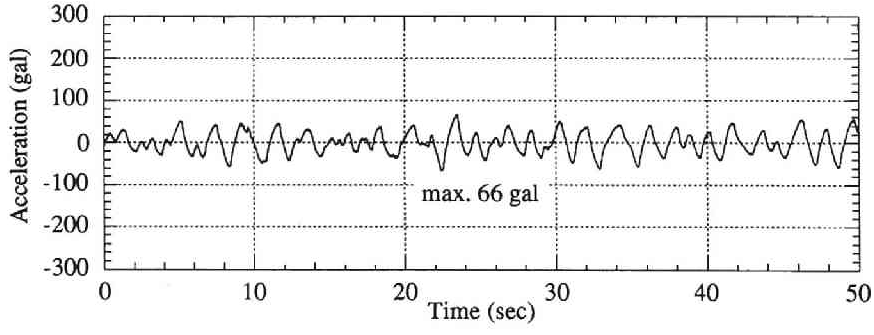

(3) Girder (above HDR) acceleration of isolated structure.

Figure 5.7 (h) Acceleration time histories for Case 3–90.
(Type 3 earthquake, max. 90 gal)

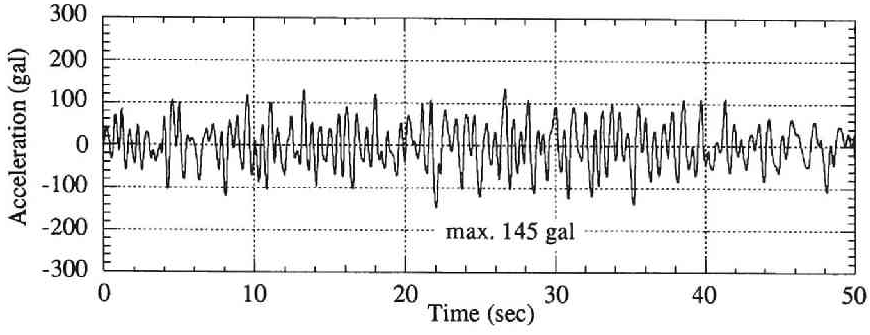

(1) Non-isolated pier-girder acceleration.

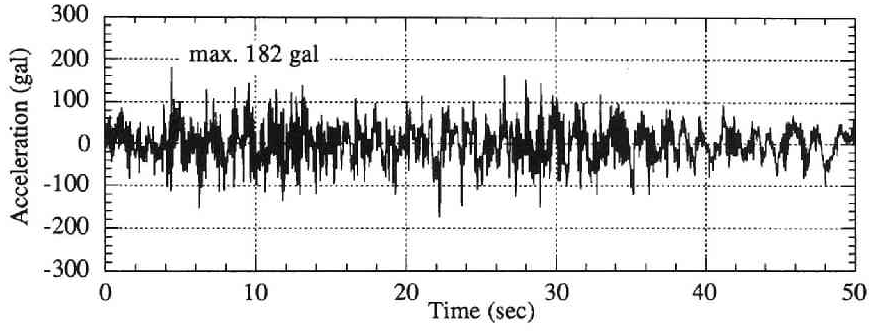

(2) Pier top (below HDR) acceleration of isolated structure.

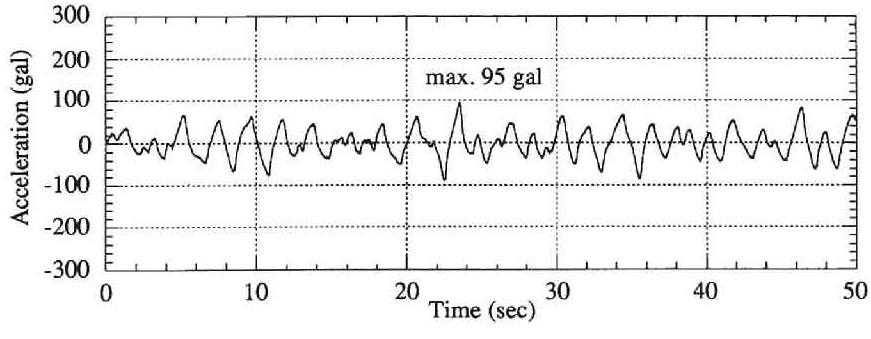

(3) Girder (above HDR) acceleration of isolated structure.

Figure 5.7 (i) Acceleration time histories for Case 3–120.
(Type 3 earthquake, max. 120 gal)

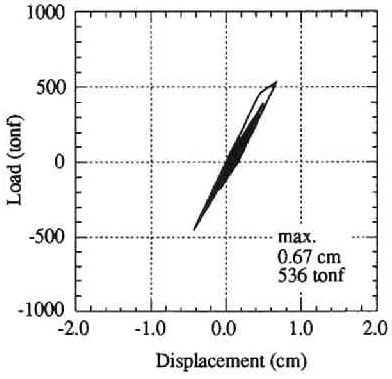

(1) Non-isolated pier-girder hysteretic response.

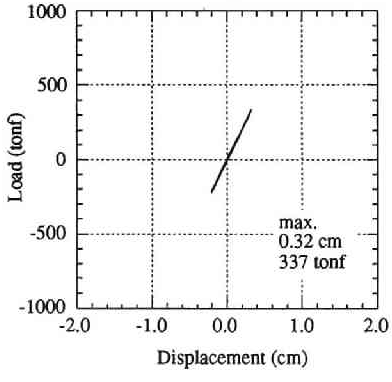

(2) Pier top (below HDR) hysteretic response of isolated structure.

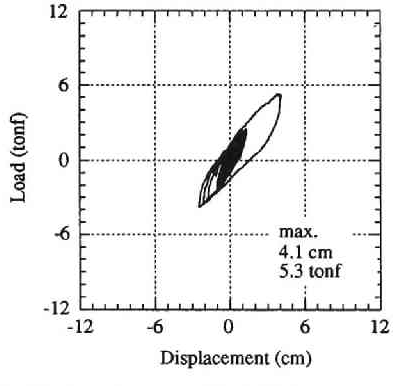

(3) Girder (above HDR) hysteretic response of isolated structure.

Figure 5.8 (a) Hysteretic response for Case 1-60.

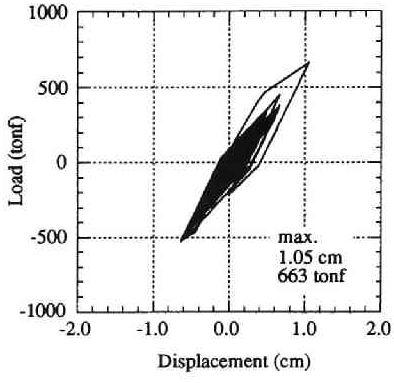

(1) Non-isolated pier-girder hysteretic response.

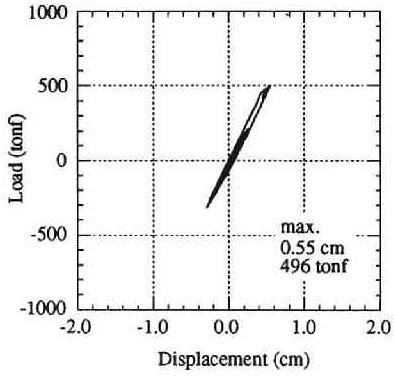

(2) Pier top (below HDR) hysteretic response of isolated structure.

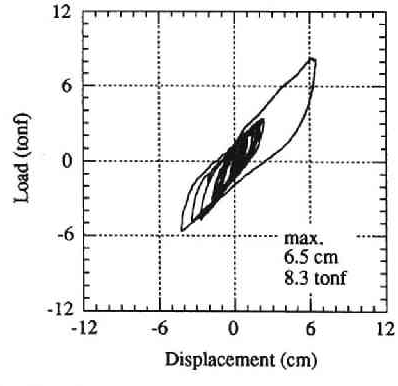

(2) Girder (above HDR) hysteretic response of isolated structure.

Figure 5.8 (b) Hysteretic response for Case 1-90.

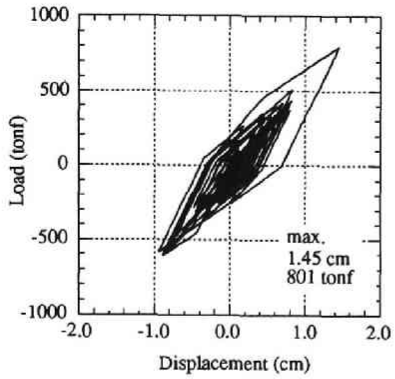

(1) Non-isolated pier-girder hysteretic response.

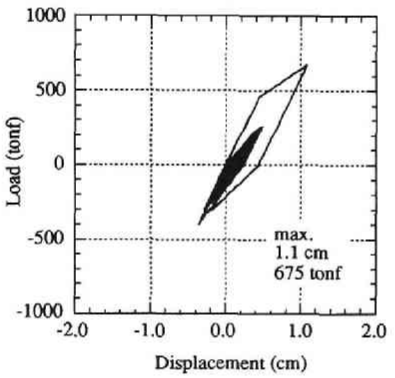

(2) Pier top (below HDR) hysteretic response of isolated structure.

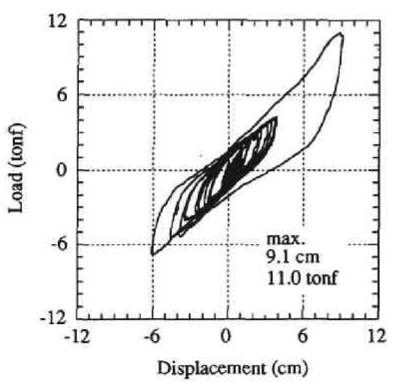

(3) Girder (above HDR) hysteretic response of isolated structure.

Figure 5.8 (c) Hysteretic response for Case 1-120.

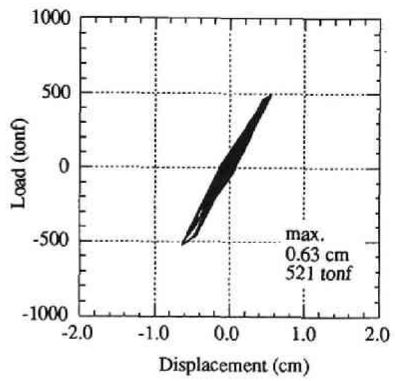

(1) Non-isolated pier-girder hysteretic response.

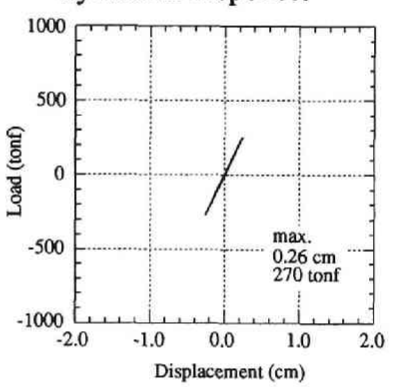

(2) Pier top (below HDR) hysteretic response of isolated structure.

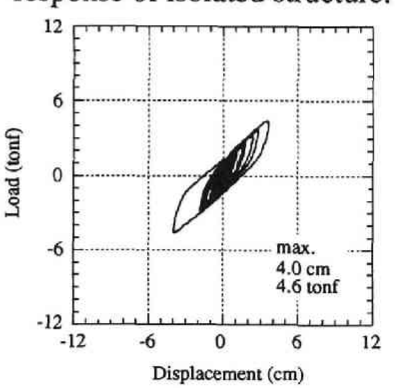

(2) Girder (above HDR) hysteretic response of isolated structure.

Figure 5.8 (d) Hysteretic response for Case 2-60.

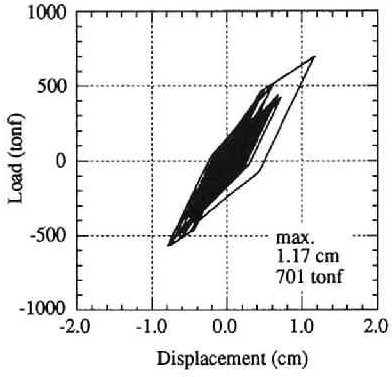

(1) Non-isolated pier-girder hysteretic response.

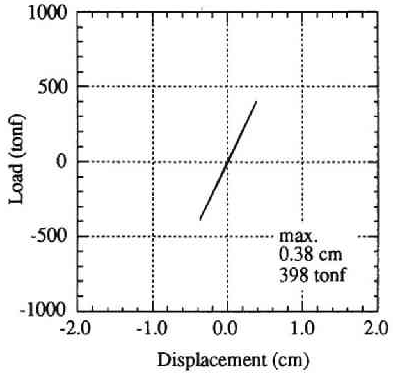

(2) Pier top (below HDR) hysteretic response of isolated structure.

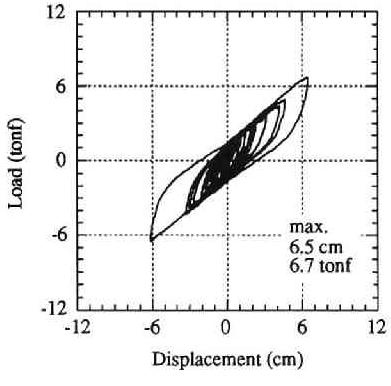

(3) Girder (above HDR) hysteretic response of isolated structure.

Figure 5.8 (e) Hysteretic response for Case 2-90.

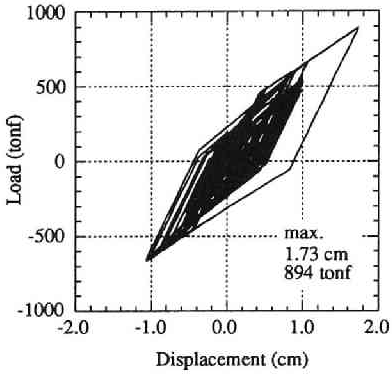

(1) Non-isolated pier-girder hysteretic response.

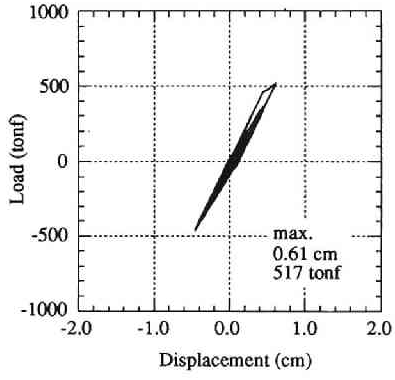

(2) Pier top (below HDR) hysteretic response of isolated structure.

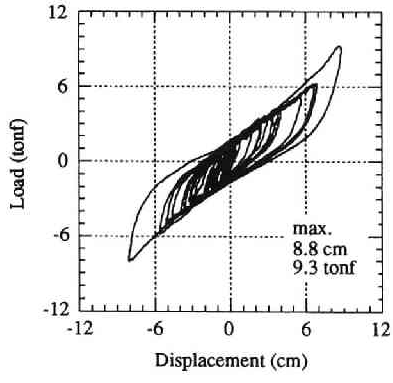

(2) Girder (above HDR) hysteretic response of isolated structure.

Figure 5.8 (f) Hysteretic response for Case 2-120.

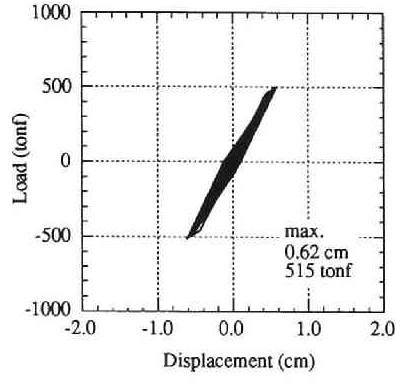

(1) Non-isolated pier-girder hysteretic response.

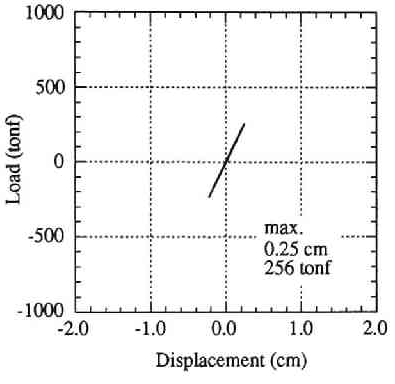

(2) Pier top (below HDR) hysteretic response of isolated structure.

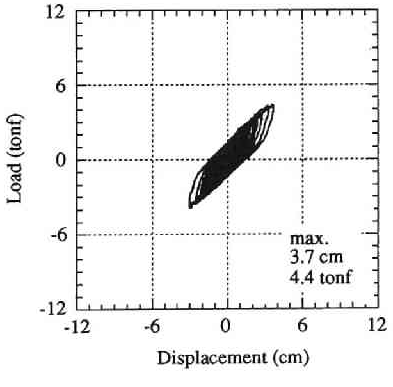

(3) Girder (above HDR) hysteretic response of isolated structure.

Figure 5.8 (g) Hysteretic response for Case 3-60.

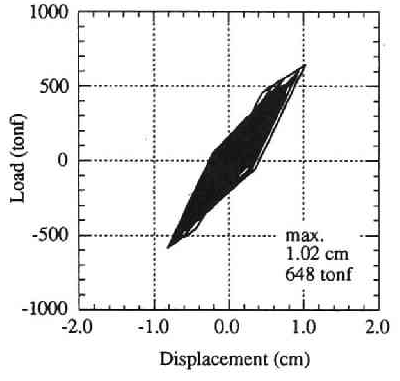

(1) Non-isolated pier-girder hysteretic response.

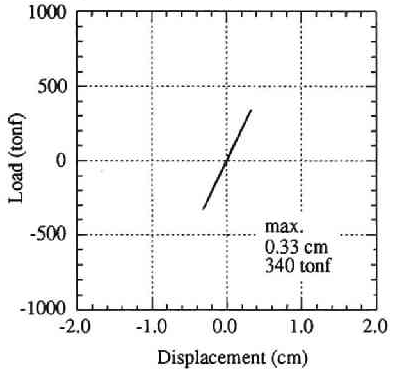

(2) Pier top (below HDR) hysteretic response of isolated structure.

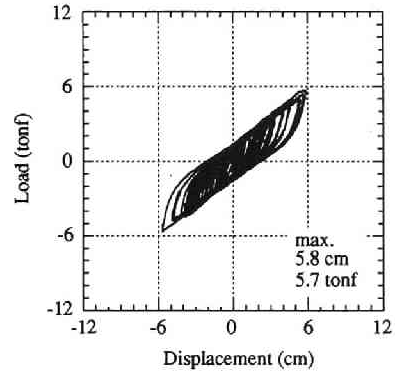

(2) Girder (above HDR) hysteretic response of isolated structure.

Figure 5.8 (h) Hysteretic response for Case 3-90.

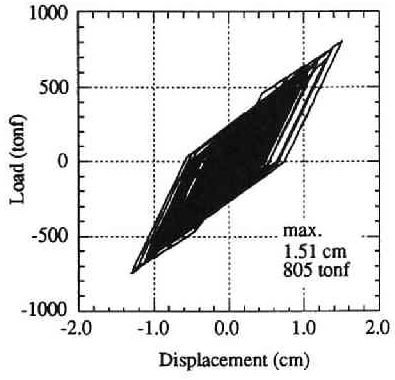

(1) Non-isolated pier-girder hysteretic response.

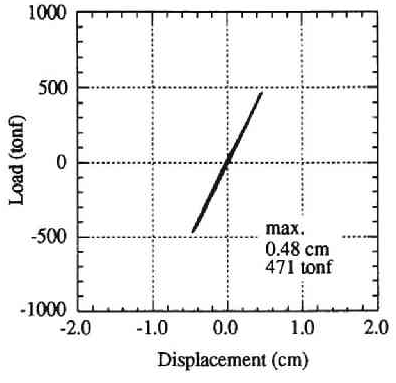

(2) Pier top (below HDR) hysteretic response of isolated structure.

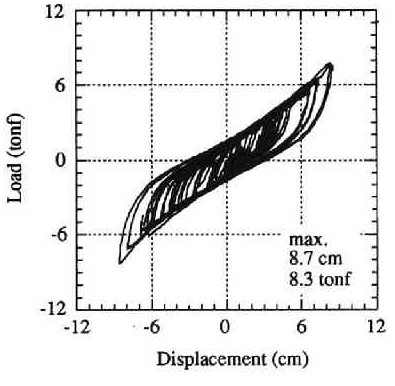

(3) Girder (above HDR) hysteretic response of isolated structure.

Figure 5.8 (i) Hysteretic response for Case 3-120.

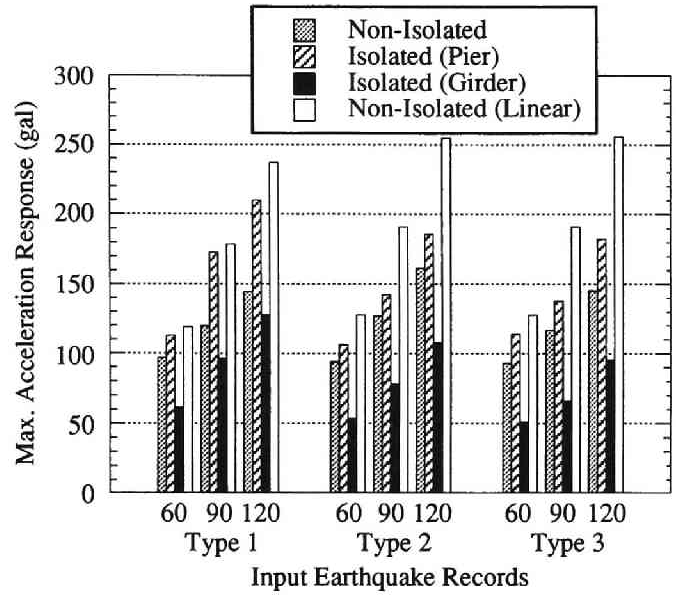

Figure 5.9 Comparison of maximum acceleration response for non-isolated and isolated structures.

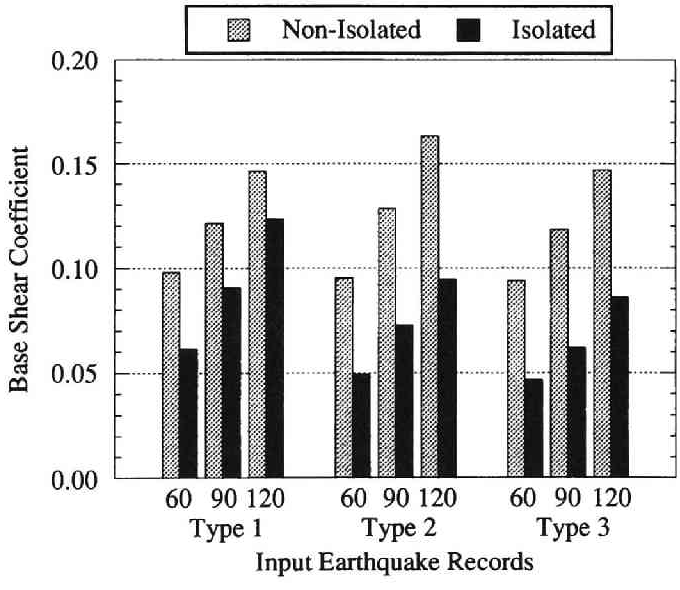

Figure 5.10 Comparison of base shear coefficients for non-isolated and isolated structures.

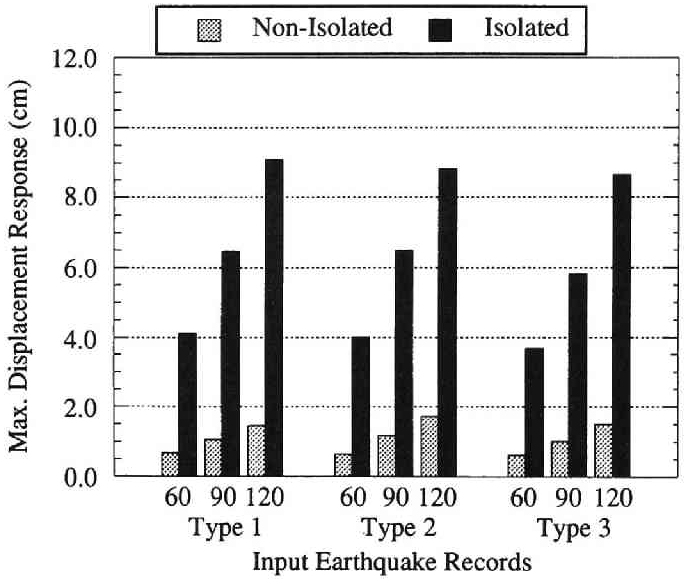

Figure 5.11 Comparison of maximum displacement response for non-isolated and isolated girders.

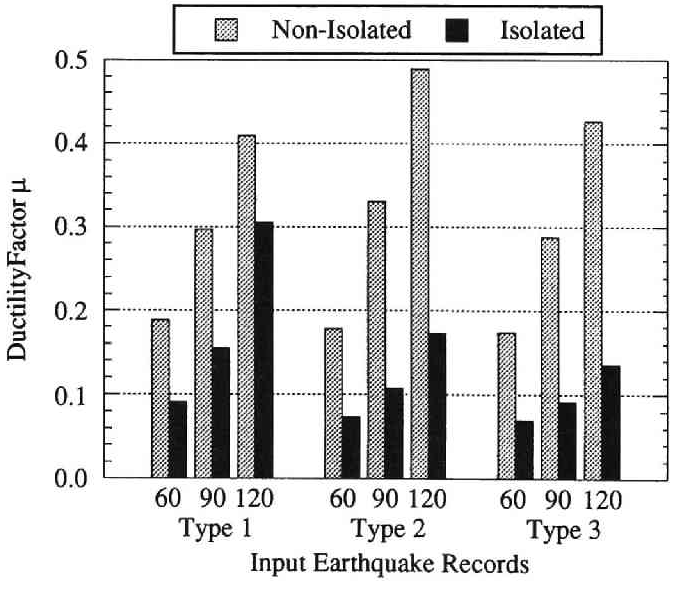

Figure 5.12 Comparison of ductility factor for non-isolated and isolated RC piers.

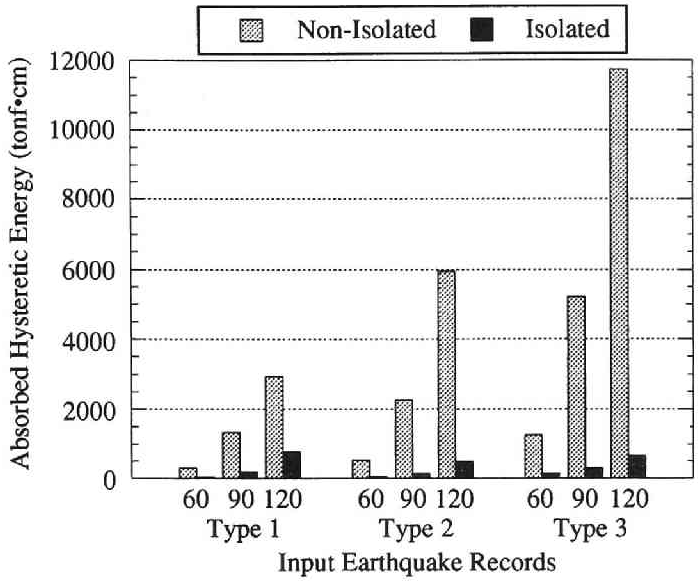

Figure 5.13 Comparison of absorbed hysteretic energy during earthquake response for non-isolated and isolated structures.

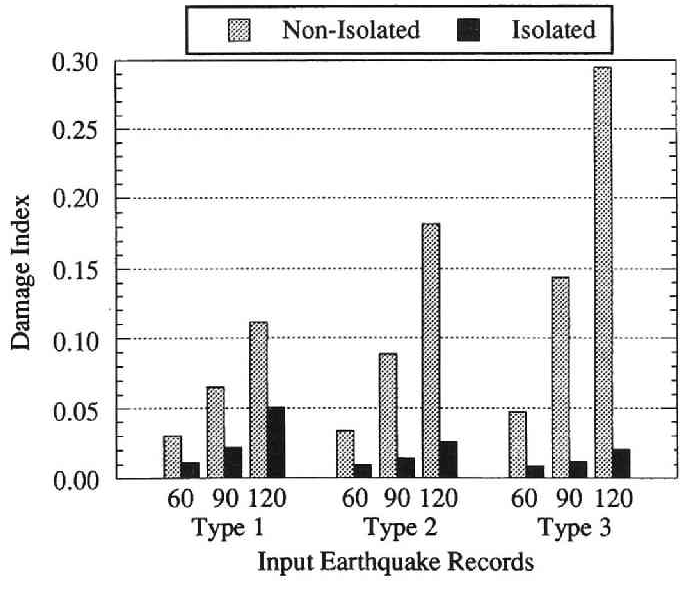

Figure 5.14 Comparison of damage index for non-isolated and isolated RC piers.

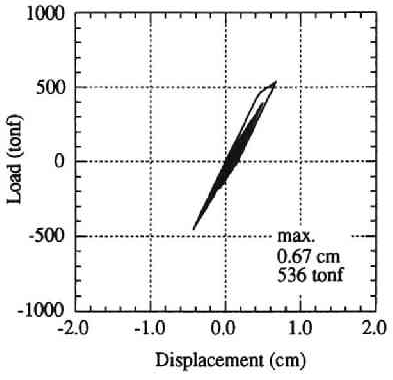

(1) Pier-girder hysteretic response during pre-loading.

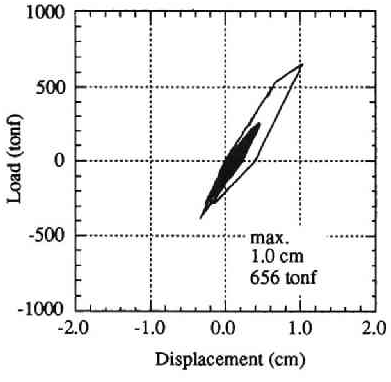

(2) Pier top (below HDR) hysteretic response during main loading.

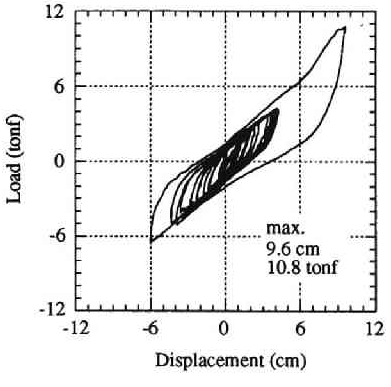

(3) Girder (above HDR) hysteretic response during main loading.

Figure 5.15 (a) Hysteretic response for Case 1-A.

Case 1-A

1 Type 1 max. 60 gal without isolator

2 Type 1 max. 120 gal with isolator

Case 1-B

1 Type 1 max. 120 gal with isolator

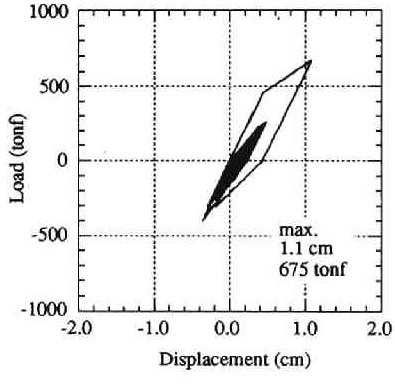

(1) Pier top (below HDR) hysteretic response during main loading.

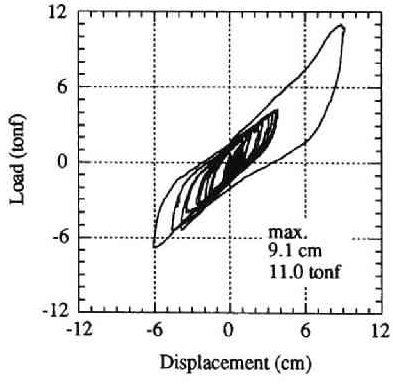

(2) Girder (above HDR) hysteretic response during main loading.

Figure 5.15 (b) Hysteretic response for Case 1-B.

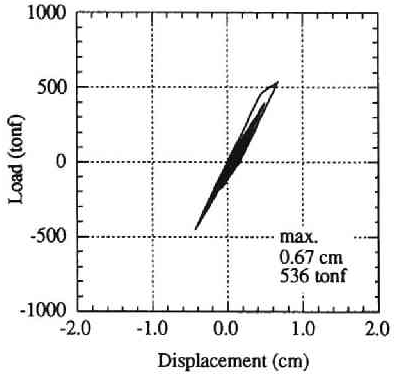

(1) Pier-girder hysteretic response during pre-loading.

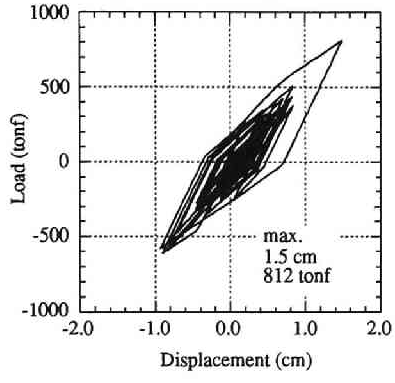

(2) Pier-girder hysteretic response during main loading.

Figure 5.15 (c) Hysteretic response for Case 1-C.

Case 1-C

1 Type 1 max. 60 gal without isolator

2 Type 1 max. 120 gal without isolator

Case 1-D

1 Type 1 max. 120 gal without isolator

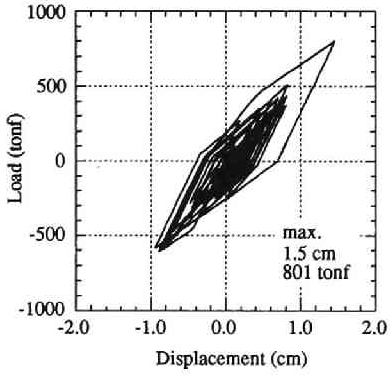

Pier-girder hysteretic response during main loading.

Figure 5.15 (d) Hysteretic response for Case 1-D.

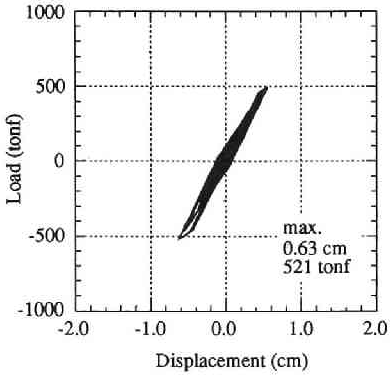

(1) Pier-girder hysteretic response during pre-loading.

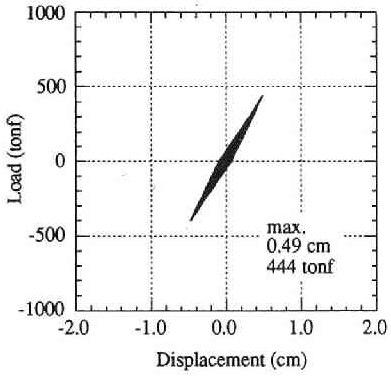

(2) Pier top (below HDR) hysteretic response during main loading.

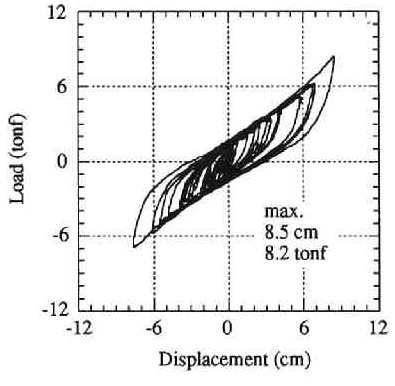

(3) Girder (above HDR) hysteretic response during main loading.

Figure 5.15 (e) Hysteretic response for Case 2-A.

Case 2-A

1 Type 2 max. 60 gal without isolator

2 Type 2 max. 120 gal with isolator

Case 2-B

1 Type 2 max. 120 gal with isolator

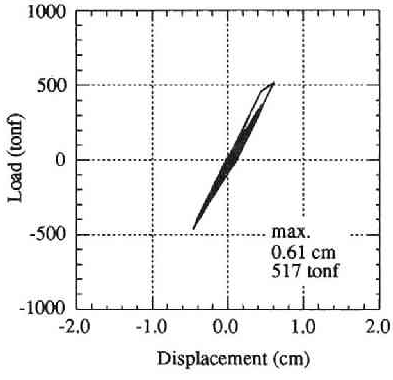

(1) Pier top (below HDR) hysteretic response during main loading.

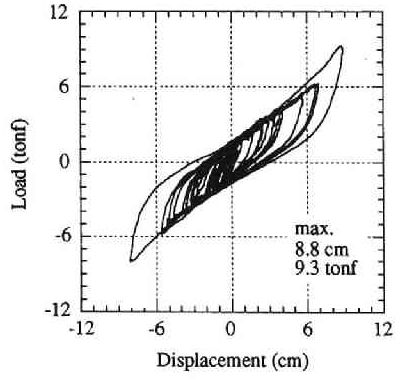

(2) Girder (above HDR) hysteretic response during main loading.

Figure 5.15 (f) Hysteretic response for Case 2-B.

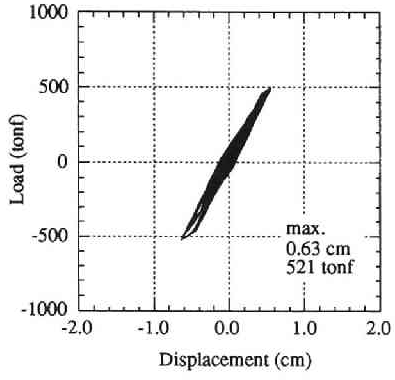

(1) Pier-girder hysteretic response during pre-loading.

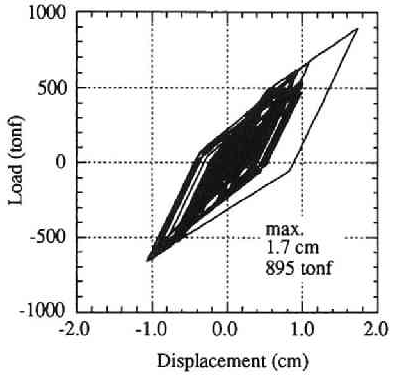

(2) Pier-girder hysteretic response during main loading.

Figure 5.15 (g) Hysteretic response for Case 2-C.

Case 2-C

1 Type 2 max. 60 gal without isolator

2 Type 2 max. 120 gal without isolator

Case 2-D

1 Type 2 max. 120 gal without isolator

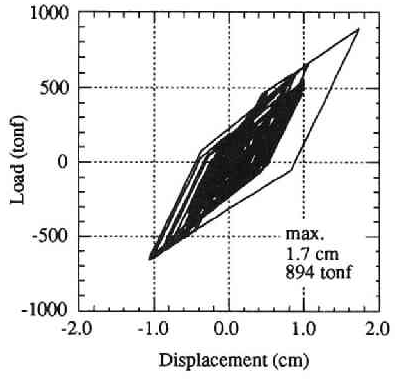

Pier-girder hysteretic response during main loading.

Figure 5.15 (h) Hysteretic response for Case 2-D.

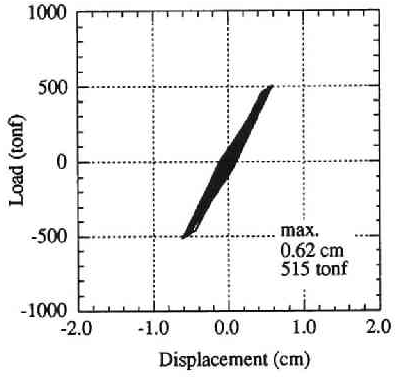

(1) Pier-girder hysteretic response during pre-loading.

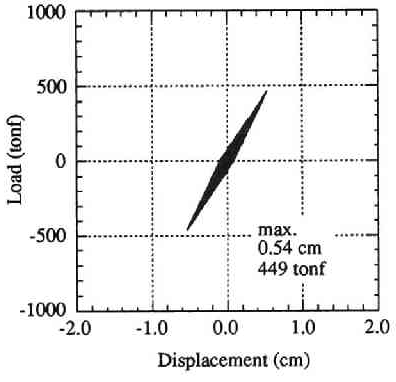

(2) Pier top (below HDR) hysteretic response during main loading.

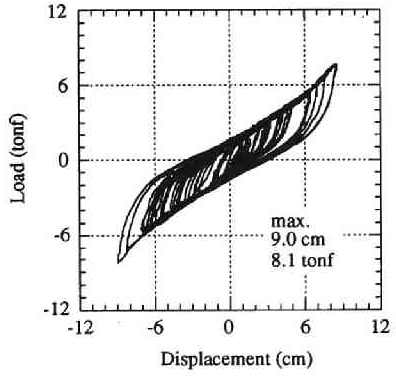

(3) Girder (above HDR) hysteretic response during main loading.

Figure 5.15 (i) Hysteretic response for Case 3-A.

Case 3-A

1. Type 3 max. 60 gal without isolator
2. Type 3 max. 120 gal with isolator

Case 3-B

1. Type 3 max. 120 gal with isolator

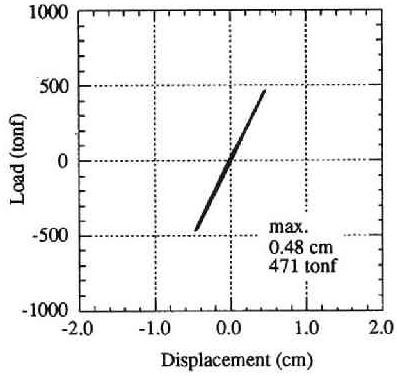

(1) Pier top (below HDR) hysteretic response during main loading.

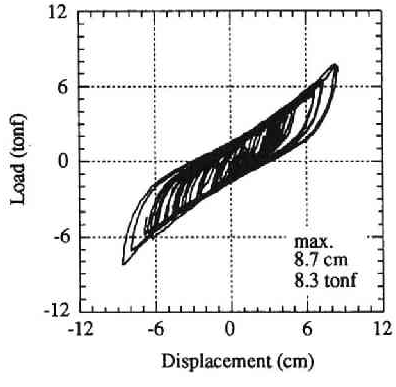

(2) Girder (above HDR) hysteretic response during main loading.

Figure 5.15 (j) Hysteretic response for Case 3-B.

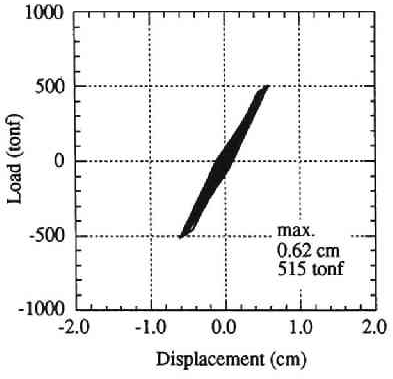

(1) Pier-girder hysteretic response during pre-loading.

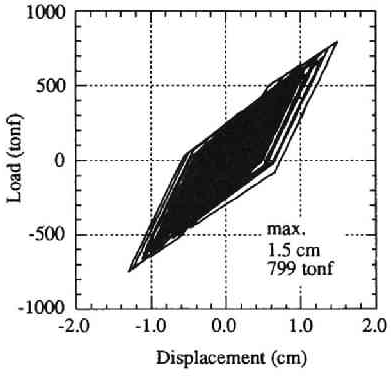

(2) Pier-girder hysteretic response during main loading.

Figure 5.15 (k) Hysteretic response for Case 3-C.

Case 3-C

1 Type 3 max. 60 gal without isolator

2 Type 3 max. 120 gal without isolator

Case 3-D

1 Type 3 max. 120 gal without isolator

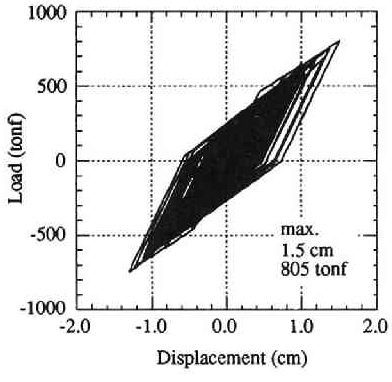

Pier-girder hysteretic response during main loading.

Figure 5.15 (l) Hysteretic response for Case 3-D.

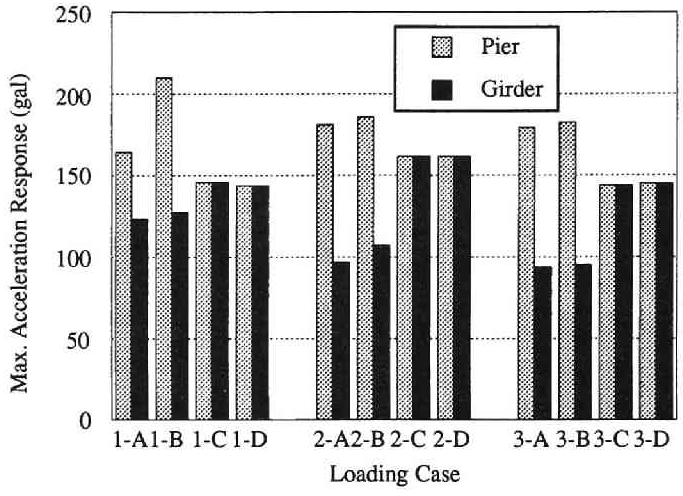

Figure 5.16 Comparison of maximum acceleration response for original and damaged structures.

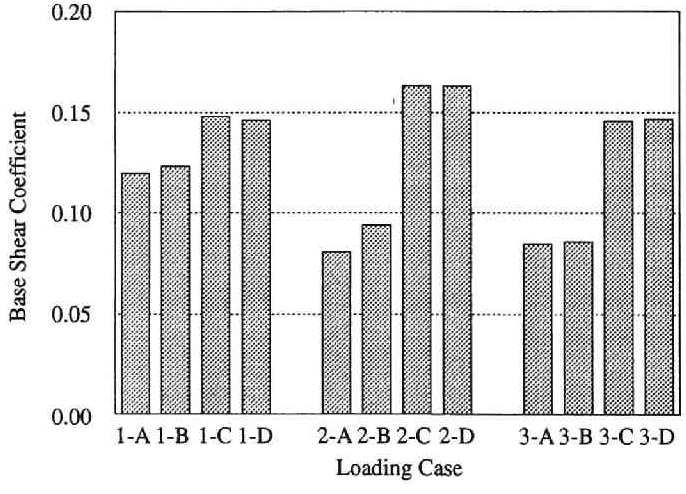

Figure 5.17 Comparison of base shear coefficients for original and damaged structures.

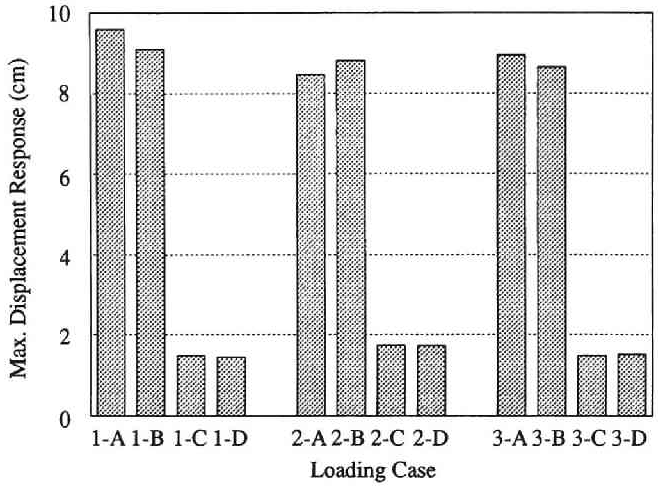

Figure 5.18 Comparison of maximum displacement response for original and damaged girders.

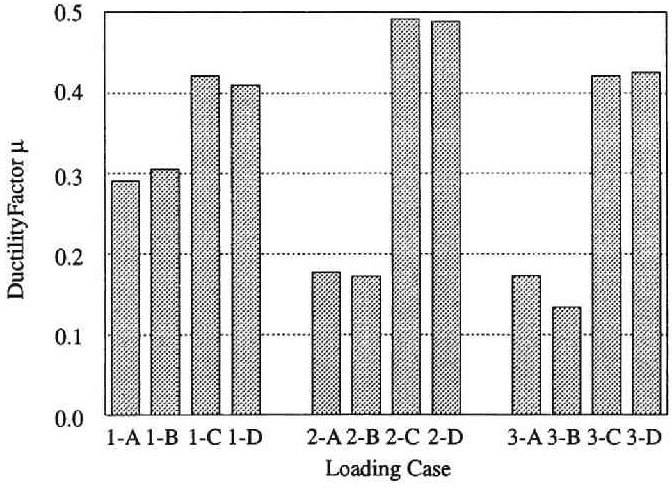

Figure 5.19 Comparison of ductility factor for original and damaged RC piers.

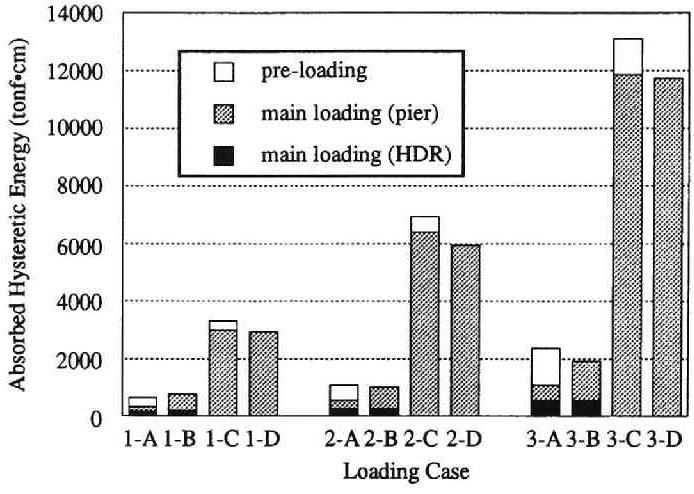

Figure 5.20 Comparison of absorbed hysteretic energy during earthquake response for original and damaged structures.

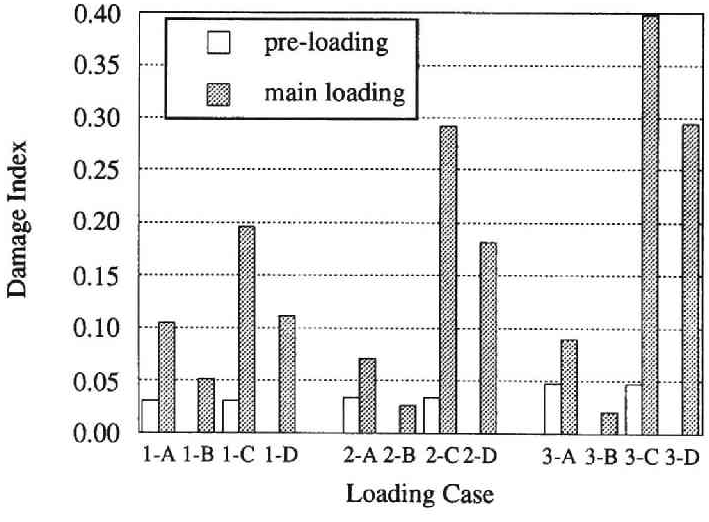

Figure 5.21 Comparison of damage index for original and damaged RC piers.

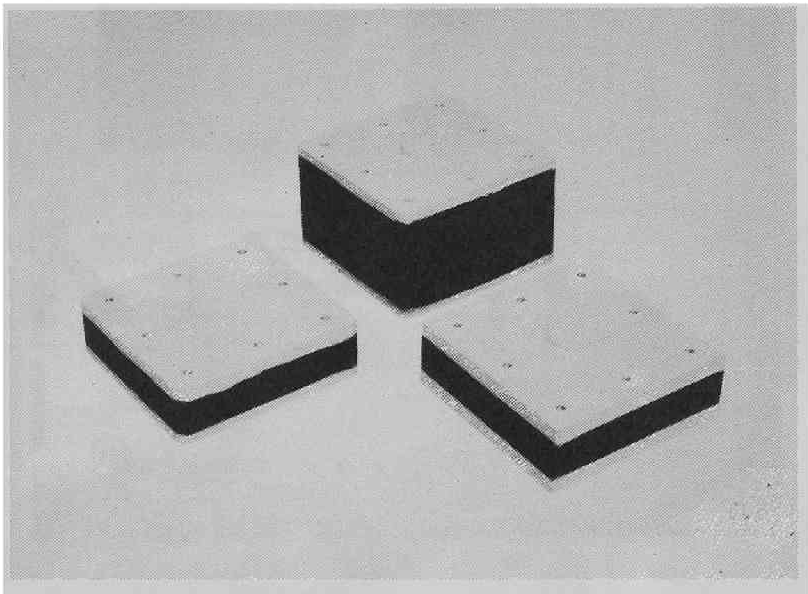

Photo 5.1 Various types of HDR isolators.

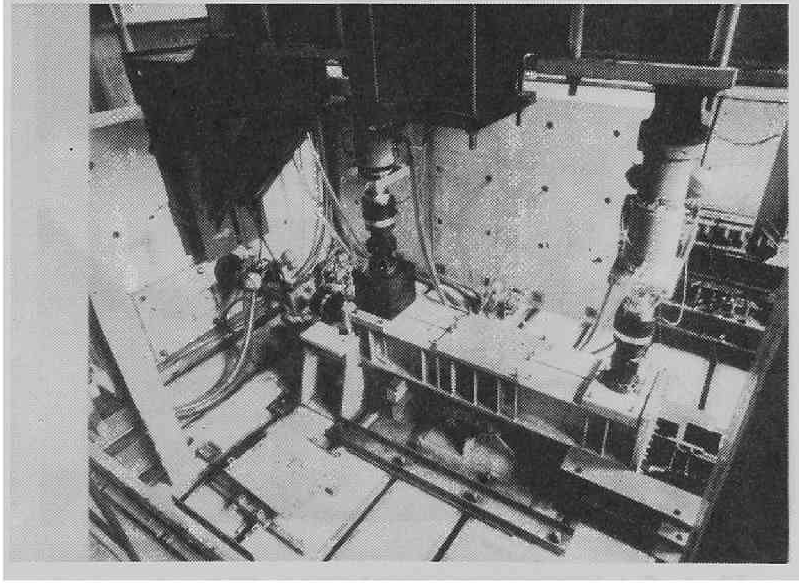

Photo 5.2 Test set-up of the hybrid loading system for HDR isolator.

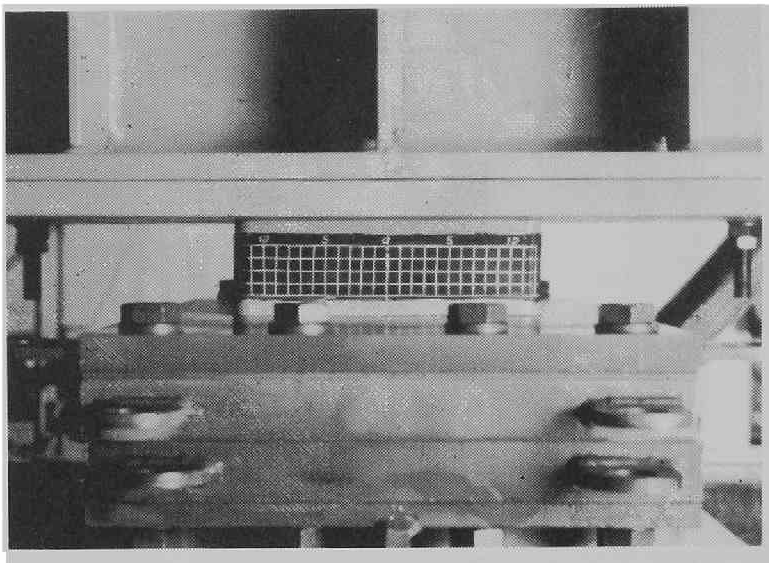

Photo 5.3 Test set-up of HDR isolator specimen.

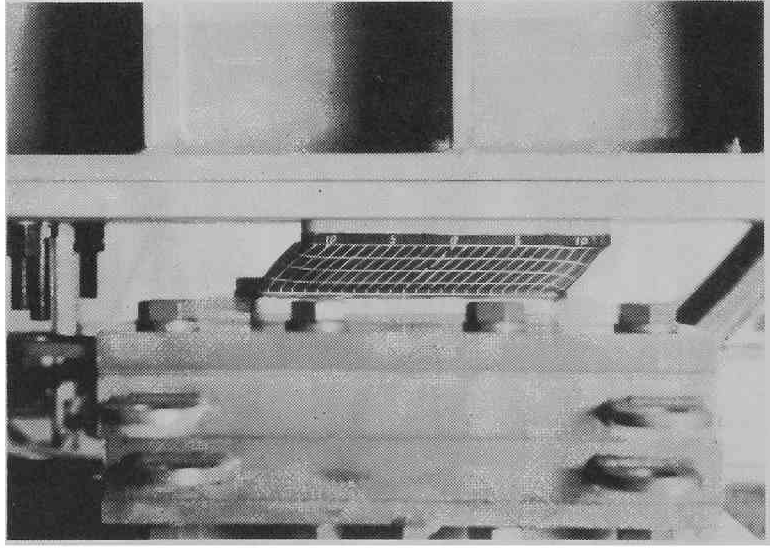

Photo 5.4 HDR isolator specimen under loading test.

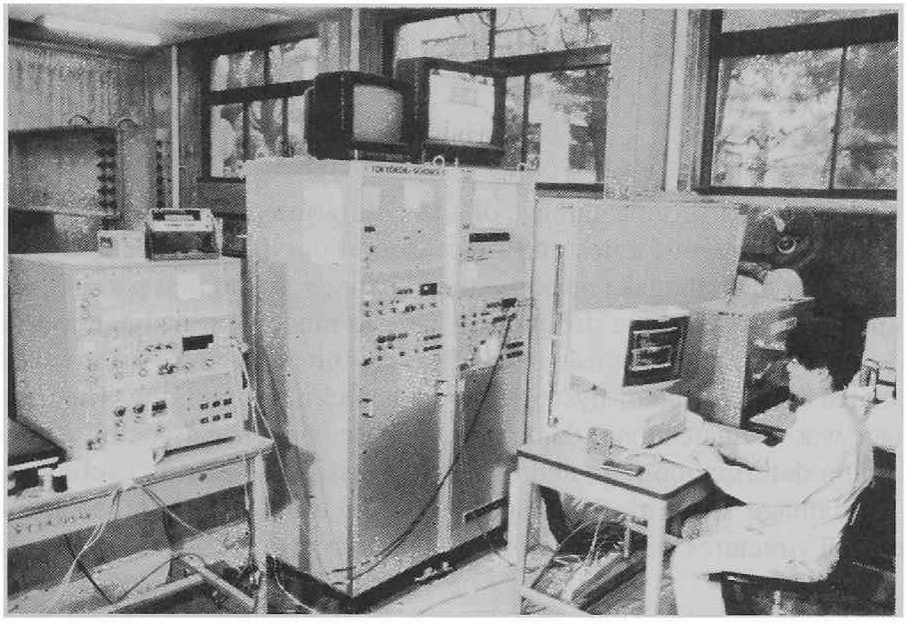

Photo 5.5 Personal computer and controllers of actuators.

6. Concluding Remarks

6.1 Summary

Estimation of seismic damage of an existing structure varies depending on the assumed hysteretic rules and input excitations because of indices being calculated from earthquake response time histories. In the first part of this study (Chapter 2), effects of the different hysteretic models on damage assessment was studied. First, response of RC bridge piers during earthquakes was calculated using different hysteretic models and input motions. Then, seismic damage was evaluated by 1) damage index based on a linear combination of the maximum deformation ratio and the energy dissipation during cyclic loadings, and 2) damage spectra of damage index, ductility and absorbed hysteretic energy for structures with various natural periods.

The other important problem about existing structures is retrofit for future earthquakes. Using experimental simulation of the inelastic restoring force properties by HYLSER (Hybrid Loading System of Earthquake Response), effects of different repair techniques on the stiffness-deteriorating process and energy-absorbing capacity of the repaired test specimens were studied. Three repair methods were used, and the behavior of the repaired specimens was compared with earlier tested specimens. A description of hybrid experiment method used to analyze retrofitted RC members under varying bending loads and constant axial force, and the experimentally simulated behavior of these members during earthquakes were discussed in Chapter 3.

In the next part (Chapter 4), effectiveness of seismic retrofit for a damaged reinforced concrete structure repaired with grouted epoxy resin or steel jackets was quantified analytically. Retrofitted reinforced concrete structures were modeled using fiber modeling technique extended to include the stress-strain relation of repair material such as grouted epoxy resin or covered steel plates. Earthquake response analysis was then conducted using inelastic hysteretic rules. Effectiveness of seismic retrofit was evaluated through comparison of ductility, hysteretic energy and damage index with the original members. The proposed method was verified by the test results of retrofitted RC beam members. As an application of this method, earthquake response of a strengthened RC bridge pier was simulated. The bridge pier with reinforcements terminated at mid-height was modeled including retrofitting by

steel jackets.

Effectiveness of a seismic isolator in retrofitting an RC bridge pier was studied using hybrid experimental system and numerical simulations in Chapter 5. A high damping rubber (HDR) bearing was used as a seismic isolator in this study. A T-shape bridge pier was modeled as 1-d.o.f. system which has an inelastic spring and a mass. Applying the substructure hybrid testing concepts, the bridge pier was assumed as an analytical substructure while a seismic isolator was assumed as an experimental substructure. In total, nine cases of experiments were conducted by changing the input motions. The results were then compared with the analytical response of the original non-isolated pier. Furthermore, the effectiveness of the isolator to the slightly damaged pier for retrofit work is also discussed.

6.2 Conclusions

From numerical simulations, the non-degrading maximum value directed model has been found to be accurate enough for seismic damage analysis while the bilinear model underestimated damage because of its linear response to the low intensity cyclic loadings. The maximum value directed model was also needed to predict damage index from the maximum velocity or the spectral intensity of the input motions.

From the hybrid experiments of the repaired RC members, the stiffness deterioration of the repaired specimens resembled that of the unrepaired originals when suitable repair methods were used. Energy-absorbing capability also was regained for adequately repaired specimens.

Analytical methods for inelastic earthquake response analysis was proposed using the skeleton curves obtained from the fiber model extended to include repair materials. Analytically obtained hysteretic loops, absorbed hysteretic energy and damage indices were in good agreement with the experimental results. The hysteretic loops of both original and retrofitted RC members can be modeled by the proposed method with high accuracy. Furthermore, aseismic behavior of the strengthened bridge pier was simulated, and effectiveness of thinner steel jackets was verified.

Effectiveness of a seismic isolator for use in retrofit work was verified by experimental and numerical analyses. The isolated pier showed almost linear response while the non-isolated pier showed inelastic cyclic behavior. The

isolated bridge pier element can be accurately modeled using linear hysteretic model. The isolated girder showed smaller acceleration response of the non-isolated structure. However, the maximum acceleration response of the isolated pier top was higher than the non-isolated original pier because of its almost linear response of the isolated pier. The maximum base shear force, the absorbed hysteretic energy, the ductility factor and the damage index decreased for the isolated structures to less than half of the non-isolated structures. On the contrary, the maximum displacement of the isolated girders became more than 6 times larger than the non-isolated girders. Besides, the first loading without isolators using weak input motions did not affect on the response under second loading with isolators using strong input motions.

For future studies, analytical method to simulate seismic behavior of retrofitted RC structures might be refined in the following points. After retrofitting work, damaged concrete and reinforcing steel were assumed to be new again. This will underestimate seismic damage if some components of the structure are in fact ineffective even after retrofitting. The proposed present method is, however, still effective if the remaining original components of the structure has no past significant damage when it is retrofitted.